Numerical Simulation of Pollutant Emission and Flame Extinction in Lean Premixed Systems

A Thesis
Presented to
The Academic Faculty

by

Gilles Eggenspieler

In Partial Fulfillment
of the Requirements for the Degree
Doctor of Philosophy

School of Aerospace Engineering
Georgia Institute of Technology
August 2005

Numerical Simulation of Pollutant Emission and Flame Extinction in Lean Premixed Systems

Approved by:

Prof. Suresh Menon,
School of Aerospace Engineering
Georgia Institute of Technology
Committee Chair

Prof. Tim Lieuwen,
School of Aerospace Engineering
Georgia Institute of Technology

Dr. Yedidia Neumeier,
School of Aerospace Engineering
Georgia Institute of Technology

Prof. Jerry Seitzman,
School of Aerospace Engineering
Georgia Institute of Technology

Prof. Fotis Sotiropoulos,
School of Civil Engineering
Georgia Institute of Technology

Date Approved : July 6, 2005

To my parents,

ACKNOWLEDGEMENTS

First, I would like to thanks Prof. Suresh Menon for giving me the opportunity to discover the fascinating world of combustion and Computational Fluid Dynamics as well as for giving me the opportunity to study interesting and challenging problems. Also, I express my gratitude toward Prof. Suresh Menon for his patience and tolerance.

I want to extend my thanks to my Committee members: Prof. Tim Lieuwen, Dr. Yedidia Neumeier, Prof. Jerry Seitzman and Prof. Fotis Sotiropoulos for evaluating this work and for giving excellent suggestions.

This work is not the work of one person and I would like to thank all current and former members of the Computational Combustion Lab; without their help, this work would not have been possible. I also greatly appreciated the help of Dr. Chris Stone and Dr. Vaidya Sankaran, who were always available to answer my questions.

I would like to thank General Electric for funding this research as well as the Department of Defense super-computer centers for providing the computational capabilities.

Also, I want to thank my parents and my friends for their support during these five years. I would never have been able to complete this degree without them.

I also would like to thank Starbucks Coffee for helping me staying awake for long hours in front of the computer and the New York Times for providing great news coverage available all day when a break from coding was necessary!

TABLE OF CONTENTS

LIST OF TABLES

LIST OF FIGURES

NOMENCLATURE

Roman Symbols

c	speed of Sound
c_p	specific heat at constant pressure per unit mass
c_v	specific heat at constant volume per unit mass
C_ν	model coefficient for turbulent viscosity
C_ϵ	model coefficient for subgrid dissipation
D	mass diffusivity
E	total energy per unit mass
e_i	internal energy per unit mass
H	total enthalpy per unit mass
H^{sgs}	subgrid enthalpy flux
i, j, k	computational grid indices
k^{sgs}	subgrid kinetic energy
l	eddy size
Le	Lewis number
N	total number of species
P	pressure
Pr	prandtl number
Pr_t	turbulent Prandtl number
q_i	heat flux vector
$q_{i,k}^{sgs}$	subgrid heat flux
Re	reynolds number
R_u	universal gas constant
T	temperature
T^{sgs}	species-Temperature correlation term

t	time
$\mathbf{u}$	velocity vector
u'	rms velocity, time-averaged resolved turbulence intensity
u_i	Cartesian velocity tensor component
u'_{sgs}	subgrid scale turbulence intensity
V	control volume
$V_{i,k}$	diffusion velocity of species k
W_k	molecular weight of species k
x, y, z	Cartesian coordinate directions
X_k	mole fraction of species k
Y_k	mass fraction of species k
$Y_{i,k}^{sgs}$	subgrid species flux

Greek Symbols

γ	ratio of specific heats
α	thermal diffusivity
ε	turbulent kinetic energy dissipation rate,
ρ	density
δ_{ij}	Kronecker delta
Δ	local grid size
κ	thermal conductivity
η	Kolmogorov length scale
λ	stirring frequency
ν	kinematic viscosity
ν_t	eddy viscosity
Φ	equivalence ratio
τ	large-eddy time scale
τ_{ij}	viscous stress tensor

τ_{ij}^{sgs}	subgrid stress tensor
$\theta_{i,k}^{sgs}$	Subgrid species diffusive flux

Subscripts

0	reference quantity
i, j, k	Cartesian tensor indices or species indices
n	time step index
t	turbulent quantity
sgs	subgrid scale
$stir$	stirring

Superscripts

$\widetilde{\Psi}$	resolved subgrid scale quantity
$\widehat{\Psi}$	test filter subgrid scale quantity
$\overline{\Psi}$	space average scale quantity
sgs	subgrid scale

Other Symbols

∂	partial derivative
∇	gradient operator
$\nabla\cdot$	divergence operation
$\sum$	summation
Π	product
$< \phi >$	ensemble averaging (of ϕ)
$\widetilde{\phi}$	Favre spatial filter or Favre time average (of ϕ)
$*$	non dimensional

Abbreviations

CFD	Computational Fluid Dynamics
DNS	Direct Numerical Simulation
DOE	Department Of Energy
HAT	Humid Air Turbine
LDKM	Localized Dynamic k-equation Model
LES	Large-Eddy Simulation
LEM	Linear-Eddy Model
MPI	Message Passing Interface
rms	Root Mean Square, Variance

SUMMARY

Premixed and partially-premixed combustion and pollutant emissions in full-scale gas turbines has been numerically investigated using a massively-parallel Large-Eddy Simulation Combustion Dynamics Model.

Through the use of a flamelet library approach, it was observed that CO (Carbon Oxide) and NO (Nitric Oxide) emission can be predicted and match experimental results. The prediction of the CO emission trend is shown to be possible if the influence of the formation of UHC (Unburnt HydroCarbons) via flame extinction is taken into account. Simulations were repeated with two different combustion approach: the G-equation model and the Linear-Eddy Mixing (LEM) Model. Results are similar for these two set of numerical simulations.

The LEM model was used to simulate flame extinction and flame lift-off in a dump combustion chamber. The LEM model is compared to the G-equation model and it was found that the LEM model is more versatile than the G-equation model with regard to accurate simulation of flame propagation in all turbulent premixed combustion regimes. With the addition of heat losses, flame extinction was observed for low equivalence ratio. Numerical simulation of flame propagation with transient inflow conditions were also carried out and demonstrated the ability of the LEM model to accurately simulate flame propagation in the case of a partially-premixed system.

In all simulations where flame extinction and flame lift-off was simulated, release of unburnt fuel in the post-flame region through flame extinction was not observed.

CHAPTER I

INTRODUCTION

Gas turbine engines are widely used for power generation (power plants), propulsion (airplanes jet engines, marine based propulsion system, etc). These state of the art engineering marvels are available for a wide range of use, size and power: from auxiliary power generators to extremely powerful propulsion systems (GE90, PW112). The concept of a gas turbine engine was first developed by Sir Frank Whittle (1907-1996) during the 40's and all current gas turbine engines are derived from his first design and theory. Since the beginning of the development of these engines, research and development efforts were aimed at increasing their power, efficiency, reliability, etc. However public environmental awareness have pushed efforts toward the development of more environmentally friendly gas systems. The current research effort focuses on carbon monoxide (CO), nitric oxides (NO_x) and Unburnt Hydro-Carbons (UHC) emissions from gas turbine engines.

In the past 10 years, signs of oil reserve depletion became obvious and a new type of fossil fuel became of interest: natural gas Roberts [2004]. As a result, the building of infrastructure to supply Liquid Natural Gas (LNG) and to use it for power production dramatically increased in the last decade. Natural gas is now mostly used for power generation. Some prototypes of cars, trucks and airplanes using LNG are developed but the lack of a large scale LNG distribution network limits its development and market growth in the transportation industry. Therefore, data regarding LNG gas turbines is mostly available for power generation devices. These power plants often use a premixed mixture of air and natural gas which is mainly methane (CH_4). This is one of the reasons that motivated this work on turbulent combustion of methane premixed full-scale combustion chamber.

1.1 Lean Premixed Combustion and Lean Blow Out (LBO).

In the Lean-Prevaporized-Premix (LPP) technology, where fuel and oxidizer are mixed before entering the combustion chamber, emission levels are strongly correlated with the adiabatic flame temperature. The larger the adiabatic flame temperature, the higher the CO concentration at equilibrium and the larger the post-flame NO_x reaction rate. For a given operating inlet pressure and temperature, the post-flame temperature is a function of the operating equivalence ratio (Φ). Therefore, a decrease in Φ will lead, in theory, to a decrease in pollutants emission.

Most power generation gas turbines operate in the lean premixed mode where the equivalence ratio is substantially lower than unity. However, further reduction of the equivalence ratio, although desirable for emission control, is currently difficult to achieve due to a variety of reasons. As the reactant equivalence ratio decreases and the combustion process approaches the lean flammability limit, the combustion process and the flame become susceptible to small perturbations inside the combustion chamber Huan et al. [2002]. These perturbations manifest themselves as pressure oscillations, which perturb the fuel feeding system causing spatial in-homogeneity in the incoming reactant mixture. These inhomogeneities can modify the heat release pattern, which in turn, can trigger new pressure fluctuations. Unsteady heat release in-phase with the pressure oscillations can lead to large-amplitude pressure oscillation, often called combustion instability (see the description of the Rayleigh criteria in Rayleigh [1945]).

Combustion instability in gas turbine engines is a major problem in general, but more so in the lean limit. Perturbation in heat release can (and does) lead to local and/or total flame extinction. Combustion instability, if it occurs, can accelerate this flame extinction process. Flame extinction in the lean limit is often called Lean Blow-Out (LBO) and this phenomenon can occur with or without accompanying combustion instability depending upon the combustor design and operating conditions. The equivalence ratio at which LBO occurs can be larger than the lean flammability limit and depends upon the mixture properties, as well as the geometry, heat loss, level of turbulence, etc.

LBO has been observed not only in premixed system but also in liquid fueled combustor

and thus, is a generally observed feature in practical combustors. Here, we focus primarily on LBO in premixed systems. Ideally, since the flame temperature decreases as LBO limit is approached, pollutant emission is also expected to decrease. However, experimental studies Kendrick et al. [2000] show that an exponential increase in CO emission level occurs in the vicinity of the LBO limit. Although the exact process behind this phenomenon is not well understood, it is likely due to local quenching of the flame reaction zone in the highly turbulent regions, which can result in the release of unburned hydrocarbons (UHC) into the post-flame region that subsequently oxidize into CO_2 and CO.

Predicting this phenomenon, as well as predicting engine performance near LBO is currently a major research effort, since with a proper understanding of the physics, new *actively* controlled combustion systems could be designed to operate safely near the LBO limit. The practical implication of such combustion systems is profound since emission are significantly reduced. This reduction will also translate into reduction in operating and maintenance cost for power generation systems.

1.2 Premixed Turbulent Combustion Regimes

As it is well known, the premixed flame structure and its propagation characteristics depend significantly on various characteristic length and velocity scales (both turbulent and chemical). The main parameter describing turbulent combustion is the Karlovitz number, defined as $Ka = (\delta_F/\eta)^2$ (where δ_F is the laminar flame thickness and η is the Kolmogorov scale).

When $Ka<1$, the flame thickness is smaller than the smallest eddy, and thus, the flame structure is not affected by turbulent structures and the turbulent flame front can be compared to a succession of laminar flame elements also known as $flamelets$. In this case, the flame is said to propagate either in the wrinkled flamelet regime or in the corrugated flamelet regime. These two different regimes are only relevant from the numerical point of view and the specific regime depends upon the computational grid resolution. When all turbulent structures are resolved, the flame is said to propagate in the wrinkled flamelet regime but if all turbulent structures are not resolved, the flame propagates in the corrugated flamelet

regime and the flame propagation speed has to be modeled.

When the Karlovitz number is smaller than 100, turbulent structures do not penetrate the reaction zone. Flames in the flamelet and Thin-Reaction-Zone (TRZ) regime exhibit this feature. In the flamelet regime ($Ka<1$), the preheat zone is much thinner than the smallest eddy, and thus, the flame structure is not affected by turbulent structures. In the TRZ regime, some of the smaller eddies can penetrate into the preheat zone (and thus, broaden the overall flame width) but eddies still do not penetrate into the reaction zone. Thus, in both these regimes, the flame surface (identified by the thin-reaction region) and its propagation can be tracked accurately using computationally efficient level-set methods such as the G-equation approach Kim and Menon [2000], Pitsch and Duchamp De Lageneste [2002].

As the turbulence level increases, such that $Ka>100$, the smaller turbulent structures can penetrate into the reaction zone and modify its structure. This regime is often called the Broken-Reaction-Zone (BRZ) regime since the typical concept of a single connected flame is no longer applicable. If the flame structure is of no interest, and if the overall burning speed can be accurately predicted, then a level set approach can still be used in the BRZ regime. However, in such highly turbulent regimes, local flame extinction (and hence, re-ignition) is expected and needs to be included. Unfortunately, it is difficult to include extinction and especially, re-ignition in level-set methods. Recently, Meneveau and Poinsot [1991] has demonstrated that the flamelet approach is valid as long as flame quenching is a local phenomenon that does not inhibit the propagation of the rest of the flame surface. However, this requires that the overall flame is still a connected surface, which may not be valid in the BRZ regime.

In a LPP combustor, combustion occurs over a wide range of conditions depending upon the operational setup. Figure 1.1 is a diagram for turbulent premixed combustion Pitsch and Duchamp De Lageneste [2002] in which the computational approaches and the typical operating regimes for both laboratory and industrial devices are shown. Typical lean combustion in full-scale gas turbine engines occurs at the extreme limit of TRZ regime (in contrast, all laboratory flames are well within the flamelet and TRZ regimes). As the

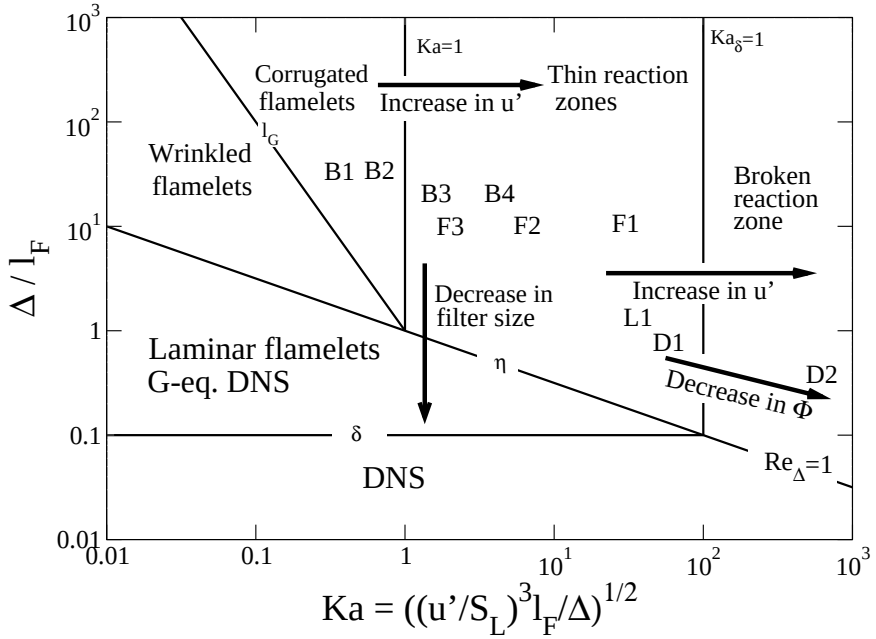

Figure 1.1: Premixed combustion regimes and locations of typical flames: B-type (Bédat and Cheng [1995]), F-type (Mansour et al. [1998]), General Electric LM-6000 (Kim and Menon [2000]) (L1) and DOE-HAT combustor (D1 for Φ>0.6 and D2 for Φ<0.5). Here, l_F is the flame thickness, u' the subgrid velocity fluctuations, S_L the laminar flame speed and $\overline{\Delta}$ is the grid size.

condition becomes leaner, combustion moves into the BRZ regime. This suggests that the type of premixed combustion in a typical gas turbine can vary widely due to operational changes but also due to spatial variability (e.g., partial premixing due to secondary air injection near walls) and thus, a proper simulation model must handle burning modes over a wide range of conditions without any ad hoc adjustments to the model. Furthermore, the model must be able to predict the resulting changes in emission levels with reasonable accuracy. So far, such a generalized method of simulation has not been demonstrated and is a major area of current research.

This work describes a comprehensive simulation method that has the potential to address all regimes of combustion and also predict pollutant emission without any ad hoc adjustments to the model. We discuss the ability of a subgrid mixing and combustion model called the linear-eddy mixing (LEM) model Kerstein [1988], Menon and Kerstein [1992] in LES with a particular focus on its application to combustion near the LBO limit.

Past studies have shown that the LEM model can handle combustion under a wide range of conditions Smith and Menon [1996a], Sankaran and Menon [2000] and thus, is considered a natural candidate for the present application.

1.3 Fluid Mechanics Modeling Methods

Computational Fluid Dynamics (CFD) tools have been developed to solve the flow governing equations, also know as the Navier-Stokes equations, in a full three dimensional system. Except in a very limited number of simple cases, the Navier-Stokes equations have no known general analytical solution. Numerical simulation will therefore solve this set of equations iteratively in time and space. A time accurate study requires all time scales present in a given flow to be resolved. A space accurate study requires all length scales present in a given flow to be resolved. In other words, the grid resolution has to be smaller than the smallest flow structure and the computation time step has to be smaller than the smallest flow time scale.

In a turbulent flow, the inertial forces are not balanced by viscous forces and, as a result, uniformities in the flow velocity field create large rotating structures, whose length scale is defined as the integral length scale L_I. These large scale structures are highly energetic vortices that are stretched. As a result, turbulent kinetic energy cascades from large scale to small scale structures (note that, a turbulent eddy is defined by its diameter - or radius - and that vortex stretching lead to the reduction of the diameter of a given eddy). At the smallest turbulent scales (η), viscous forces convert turbulent kinetic energy into heat (viscous dissipation).

The Reynolds number (Re) links L_I to η. The Reynolds number is defined as $Re = UL/\mu$ where L and U are the characteristics flow length scale and velocity, respectively. L_I is of the order of magnitude of L and L_I/η=$Re^{3/4}$. Therefore, a full three dimensional computation of a given flow field requires $Re^{9/4}$ grid points (from the geometry dimensions to the Kolmogorov scale). Typical combustion chamber have Reynolds number larger than 10^6 and simulating the flow inside such a device would require $Re^{27/2}$ grid points. Such a computation, known as Direct Numerical Simulation (DNS), far exceeds the present

available computational resources. Therefore, DNS is limited to turbulent flows where Re<3000.

The Reynolds Averaged Navier Stokes ($RANS$) technique is at the other extreme of the scope. This technique predicts time-averaged flow solutions by solving the time-averaged Navier-Stokes equations. In this technique, models have to be used in order to close the time-averaged Navier-Stockers equations. The most popular model used for closing the energy equation is the k-ϵ model, where the governing equation for both the turbulent kinetic energy k and its dissipation ϵ are solved. The Reynolds stress tensor is closed using the Boussineq gradient assumption. The $RANS$ model assumes that the Reynolds stresses adjust to changes in the flow at a time scale that is related to the time-averaged rate of strain. Unfortunately, this is not true for flow with rapid change in the mean rate of strain Bradshaw [1973]. This is especially the case for flows with separation, streamline curvature or in the case of swirling flows, which are at the center of this work.

Large-Eddy Simulation (LES) is a compromise between DNS and $RANS$. The major idea behind LES is to simulate all turbulent scale from L_I up to a length scale equal to the grid resolution. All the processes having a length scale smaller than the grid resolution (subgrid processes) are modeled. In LES, the large scale turbulent structures, that are geometry dependent, are simulated while the more universal small scale turbulent eddies are modeled.

The simulation of reacting flow presents other challenges. This is due to the fact that chemical processes (chemical reaction, molecular mixing, turbulent mixing) occurs at length scale ranging from L_I to scales that can be smaller than η. Large scale mixing increases the area separating species while small turbulent scales mixes species at this interface. Furthermore, molecular diffusion also mixes species at the separation interface. For both LES and $RANS$, unresolved turbulent and molecular mixing are non-negligible phenomena in reacting flows.

1.4 Swirling Flows

Swirling flow is an important feature of most gas turbine combustion chambers and is a major technique for flame stabilization. A swirling flow is characterized by its swirl number (S) which is the ratio of angular momentum over axial momentum. In non-reacting flows, studies Lilley [1977] showed that when S>0.6, the axial adverse pressure gradient created by the rotating flow is large enough to lead to the formation of a recirculating flow region, also known as the vortex breakdown region (VB). For reacting flows, the critical value of S increases because the general flow pattern is affected by heat release. However, a VB is still created if S is large enough.

An important mechanism for flame stabilization is the existence of regions were the flow speed matches the flame propagation speed. This is especially true in a swirling flow where the axial velocity decreases as a results of the presence of the swirl in the flow. Also, the presence of a VB ensures that the flame is compact, i.e. its length is smaller than if the incoming flow was not swirling. The point where the flow velocity becomes negative anchors the flame. Controlling the location of this point (via the swirl characteristics) is equivalent to controlling the flame shape and length. In industrial application, it is not desirable to have long and bulky combustion chambers, thus, swirling flows are used in the vast majority of combustion chambers.

1.5 Flame Extinction

The first part of this section considers stagnation point flame quenching, the second part treats the extinction of a freely propagating flame.

1.5.1 Quenching of Stagnation Point Flames

Stagnation point flame (or counter-flow flames) have been extensively studied Bush and Fendell [1970], Libby et al. [1982], Libby and Williams [1983]. Stagnation point flames are positively stretched flames. The relative diffusion of heat and species, which is a critical phenomena in premixed flames, is evaluated by the Lewis Number (Le). Le is the ratio of thermal diffusivity over species diffusivity. The stretched flame propagation speed behavior

is opposite for flame with $Le>1$ and $Le<1$. If one draws a control volume around a stagnation point flame, the control volume gains chemical energy but losses heat energy. For $Le>1$, heat loss exceeds mass gain and the flame propagation speed decreases as curvature and stretch increases. On, the other hand, for $Le<1$, heat loss is lower than mass gain and the flame temperature is higher than the adiabatic laminar unstretched flame temperature, as a consequence, the flame propagation speed increases as curvature and stretch increases. The reverse is true for negatively stretched flames. More details are given in the review of Law and Sung [2000].

Because the stretched flame propagation speed behavior is opposite for flame with $Le>1$ and $Le<1$, two very different mechanisms can lead to the extinction of a stagnation point flame. For flames with $Le>1$, the increase in flow speed increases stretch and decreases the reaction rate, causing the flame to move toward the wall. The flame quenches when the reaction rate decreases such that the flammability limit is reached. For flames with $Le<1$, the increase in the flow speed increases stretch and increases the reaction rate. As the speed increases, the increase in flame propagation speed can not overcome the increase in flow velocity and the flame moves toward the wall. There is a limit when the flame can not progress anymore toward the wall and the distance between the flame front and the wall is fixed even if the flow velocity is further increased. In this case, the residence time of reactants inside the flame decreases and is not balanced by the stretch induced increase in reaction rate. As the residence time decreases, the flame temperature decreases and the flame will quench when the flammability limit is reached Law and Sung [2000].

Therefore, a flame which has $Le>1$ quenches when strain reduces the reaction rate below the quenching reaction rate, while a flame with $Le<1$ quenches because the fuel residence time in the stagnation flame is too low. In other words, for lean methane-air flames, which have a global Lewis number smaller than unity, flame quenching is not caused by large positive strain rate but by the decrease in residence time.

This is confirmed in the work of Meneveau and Poinsot [1991] who studied the interaction between a freely propagating flame strained positively by a vortex. Again, when $Le<1$, strain does not quench the flame and only the introduction of heat losses leads to flame

extinction. As a result, extinction criteria for a freely propagating flame, that can be positively or negatively stretched, can not be directly deduced from the study of stagnation point flames.

1.5.2 Freely Propagating Flames

Flame/vortex interactions have been extensively studied experimentally Jarosinski et al. [1988], Roberts et al. [1993], Müller et al. [1995] as well as numerically Meneveau and Poinsot [1991], Najm and Wyckoff [1997]. In this case, the flame structure is laminar and the stretching effect of the vortex may lead to flame extinction. This is not comparable to a stagnation point flame, because, in this case, the flame propagates freely and the amount of stretch is variable in time.

Kagan and Sivashinsky [2000] argued that the multi-scale nature of the flow field is not crucial for flame extinction. Therefore, flame/turbulence interactions can be treated as the sum of the interactions between the flame front and a succession of isolated vortices (this assumption neglects all non-linear interactions between vortices of different sizes). A key DNS study was performed by Meneveau and Poinsot [1991] where the interaction between a laminar flame front and vortices of different sizes and energy was studied. Using these results, a $RANS$ flame extinction model was derived by Poinsot et al. [1990]. Results show that a lean methane-air flame can not be quenched by any vortex and that only heat losses can lead to extinction of a laminar flame front where the Lewis number is smaller than unity. Based on Kagan's assumption, an adiabatic flame with a Lewis number smaller than unity can not be quenched by any level of turbulence.

However, this has to be put in perspective with the fact that, in the above mentioned flame-vortex interaction study, only positively stretched flame are considered. In a fully turbulent field, the flame may be positively as well as negatively stretched. Furthermore, Meneveau *et al.* considered only two species (reactant and product). In the DNS work of Card et al. [1994], an adiabatic lean non-premixed methane-air flame is quenched by a full two-dimensionnal turbulent field. This is also the conclusion reached by Dinkelacker et al. [1998] and Buschmann et al. [1996]. Their experimental work shows that the propagation

of a lean methane-air and its structure can be drastically perturbed by turbulence and can quench a flame front.

Dinkelacker noticed that both local and global flame quenching can exist in a premixed flame propagating in a highly turbulent flow. Global flame quenching corresponds to a region where the reaction rates are null and no heat release takes place. Local flame quenching, also called "quenched reaction-zone" corresponds to a region where low concentrations of OH radical are present near the border of the unburned gas while the temperature remains close to the adiabatic flame temperature. It is concluded that local flame quenching is observable only in systems where global flame stabilization prevents a flame element to globally quench, i.e. the stabilization process still feeds energy to the flame front, even if the flame front is partially quenched. This corresponds to stabilized flames in gas turbine combustion chambers.

Numerical simulation and modeling of flame extinction near LBO is still an open question. In non-premixed systems, quenching can be predicted by comparing the scalar dissipation rate (χ) to the quenching scalar dissipation (χ_Q)Peters [1984], by using the Eddy Dissipation Concept (EDC) extinction model Byggstoyl and Magnussen [1988]. Quenching criteria can also be derived for premixed systems. Poinsot Poinsot et al. [1991] developed the Intermittent Turbulence Net Flame Stretch ($ITNFS$) model that was successfully used in pollutant prediction studies Eggenspieler and Menon [2003a], Held et al. [2001]. However, this model takes into account heat losses in the post-reaction zone and therefore, is not valid for adiabatic flame. Nonetheless, heat losses are present in a combustion chamber and this can justify the use of the $ITNFS$ model. Another approach, uses the unsteady-flamelet method Pitsch and Duchamp De Lageneste [2002], where the scalar dissipation rate is computed using information on the gradient of the variance of the progress variable Peters [2000]. This dissipation rate could be compared to the quenching scalar dissipation rate (χ_Q=8.0 s^{-1} for methane-air flame), but the capabilities of this model still have to be demonstrated. In the study of Tajiri and Menon [2001], flame quenching via turbulence was simulated by comparing the LES strain rate to the opposed flame (i.e. stagnation point flame) stretch quenching. However, as noted in section 1.5.1, this method is not valid for

freely propagating flames.

Other phenomena like heat losses and inhomogeneities in the incoming flow (either caused by the design of the feeding system or by its perturbation via the system dynamics) can also lead to or facilitate flame extinction.

1.6 Motivations and Objectives

From the three majors CFD methods, namely Direct Numerical Simulation (DNS), Reynolds Navier Stokes Average ($RANS$) technique and Large-Eddy Simulation (LES), only the LES methodology can be considered as relevant for the study of gas turbine combustion chamber. The $RANS$ techniques is not appropriate because of its inability to capture the dynamics of the system and the DNS techniques is not appropriate because of the large Reynolds number of the systems studied in this work.

Prediction of flame extinction in lean premixed systems is of great importance for many reasons. The most obvious is safety. If local and/or partial flame extinction of a limited area of the flame is acceptable, complete flame extinction under nominal operating conditions can have catastrophic consequences. Furthermore, predicting flame extinction is important for both the study of combustion chamber dynamics and pollutant emission.

Flame extinction perturbs the heat release pattern and the succession of flame extinction and re-ignition can drastically change the combustion chamber dynamics. Therefore, in numerical studies of systems operating near the LBO, flame extinction as well as its effect on the flow has to be captured in order to capture the exact combustor dynamics.

Studies of pollutant emission Eggenspieler and Menon [2003a], Held et al. [2001] demonstrated that the formation of Unburnt Hydrocarbons (UHC) is of critical importance when emission of CO are considered. UHC is formed at the flame front whenever flame quenching occurs. Therefore, it is of critical importance to study a model like the Linear-Eddy Mixing (LEM) model which is believed to be valid for all combustion regimes and which is also believed to be able to simulate premixed flame extinction when propagating in the BRZ regime.

The above remarks emphasize the need of a methodology that can simulate flame propagation and structure for all combustion regimes and using the LES technique. In the LES technique, the flame is thinner than the LES resolution and flame turbulence interactions need to be modeled. However, the Linear-Eddy Mixing Model was developed to *simulate*, rather than *model*, these subgrid interactions. In this work, we propose to study the capability of the $LEMLES$ approach to resolve the flame structure of a flame propagating in the TRZ and the BRZ regimes as well as its ability to predict pollutant emission and simulate flame extinction.

1.7 Outline

The second chapter of this thesis presents the mathematical formulation of the LES technique and the combustion models. The third chapter presents the numerical implementation used in this work as well as the geometries and operating conditions of the problem studied. The fourth chapters focuses on the study of CO and NO emission from the $DOE - HAT$ (Department of Energy - Humid Air Turbine) combustion chamber. Chapter V compares the capabilities of the two combustion models used in this study: the $G-equation$ approach and the LEM approach. Chapters VI and VII focus on the simulation of flame extinction and flame lift-off. In Chapter VI, problems with uniform inflow conditions are studied while Chapter VII focuses on the simulation of combustion in systems where the inflow conditions are non-uniform in either space and time. Conclusion of this work are presented in Chapter VIII while Chapter IX presents future research objectives.

CHAPTER II

MATHEMATICAL FORMULATION AND MODELING

In this chapter, we describe the *LES* formulation and subgrid models in some detail in order to establish the methodology used in the current study.

2.1 Gas Phase Governing Equations

The governing equations of motion for an unsteady, compressible, reacting, multi-species fluid are the Navier-Stokes equations describing the conservation of mass, momentum, total energy and species. The fully compressible version is employed since we are interested in the non-linear coupling between acoustic wave motion, vorticity dynamics and combustion heat release.

2.1.1 Governing Equations

The Navier-Stokes equations describing the conservation of mass, momentum, total energy and species are:

$$\begin{cases} \frac{\partial \rho}{\partial t} + \frac{\partial \rho u_i}{\partial x_i} = 0 \\ \frac{\partial \rho u_i}{\partial t} + \frac{\partial}{\partial x_i}\Big[\rho u_i u_j + p\delta_{ij} - \tau_{ij}\Big] = 0 \\ \frac{\partial \rho E}{\partial t} + \frac{\partial}{\partial x_i}\Big[\Big(\rho E + p\Big)u_i + q_i - u_j\tau_{ij}\Big] = 0 \\ \frac{\partial \rho Y_m}{\partial t} + \frac{\partial}{\partial x_i}\Big[\rho Y_m\Big(u_i + V_{im}\Big)\Big] = \dot{w}_m \text{ ,where m = 1,N} \end{cases} \tag{2.1}$$

In the above equations, u_i is the i-th velocity component, ρ is the mass density, p is the pressure and $E = e + \frac{1}{2}(u_k u_k)$ is the total energy. τ_{ij} is the viscous stress tensor expressed as:

$$\tau_{ij} = \mu\Big(\frac{\partial u_i}{\partial x_j} + \frac{\partial u_j}{\partial x_i}\Big) - \frac{2}{3}\mu\frac{\partial u_k}{\partial x_k}\delta_{ij} \tag{2.2}$$

where δ_{ij} is the Kronecker function. $\delta_{ij} = 0$ if $i \neq j$ and $\delta ij = 1$ if $i=j$. e is the internal energy per unit mass computed as the sum of the sensible enthalpy and the stored chemical energy:

$$e = \sum_{m=1}^{N} Y_m h_m - \frac{p}{\rho} \tag{2.3}$$

where h_m is the species enthalpy per unit mass given by:

$$h_m(T) = \Delta h^0_{f,m} + \int_{T_0}^{T} c_{P,m}(T')dT' \tag{2.4}$$

where $\Delta h^0_{f,m}$ is the enthalpy of formation per unit mass of the m-th species at the reference temperature T_0. $c_{P,m}$ is the specific heat at constant pressure for the m-th species. Y_m is the species mass fraction of the m-th species. Furthermore, V_{im} is the diffusion velocity of the m-th species in the i-th direction and $\dot{w}_m$ is the mass reaction rate per unit volume of the m-th species.

The mass reaction rate per unit volume is given by:

$$\dot{w}_m = MW_m \sum_{k=1}^{L} \Big(\nu''_{mk} - \nu'_{mk}\Big) A_k T^{\alpha_k} e^{(-E_{a,k}/R_u T)} \Pi_{n=1}^{N} \Big(\frac{X_n p}{R_u T}\Big)^{\nu'}, m = 1, N \tag{2.5}$$

where L is the number of chemical reactions of the mechanism considered and N is the number of species. MW_m is the mass fraction of the m-th species. ν''_{mk} and ν'_{mk} are the stoichiometric coefficients of the m-th species and for the k-th chemical reaction on the product and reactant side, respectively. A_k, α_k and $E_{a,k}$ are the Arrhenius rate, temperature exponents and activation energy for the k-th chemical reaction, respectively. T is the temperature and R_u is the universal gas constant. X_n is the molar fraction of the n-th species. The heat flux vector $\vec{q}$=(q_1, q_2, q_3) contains the thermal conduction (I), enthalpy diffusion (i.e. diffusion of heat due to species diffusion) (II), the Dufour heat flux and the radiation heat flux. Dufour heat flux and radiation heat flux are neglected, therefore:

$$q_i = \underbrace{-\kappa \frac{\partial T}{\partial x_i}}_{(I)} + \underbrace{\rho \sum_{m=1}^{N} h_m Y_m V_{im}}_{(II)} \tag{2.6}$$

where $\kappa = \overline{c_P}\mu/Pr$ is the mixture averaged thermal conductivity. $\overline{c_P} = \sum_{m=1}^{N} Y_m c_{P,m}$ is the mixture averaged specific heat at constant pressure and Pr is the mixture Prandtl number.

The pressure p is directly derived from the equation of state for perfect gas:

$$p = \rho RT = \rho \frac{R_u}{MW_{mix}} T = \rho R_u T \sum_{m=1}^{N} \frac{Y_m}{MW_m} \tag{2.7}$$

The species diffusion velocity is approximated using Fick's Model:

$$V_{im} = -\frac{D_m}{Y_m} \frac{\partial Y_m}{\partial xi} \tag{2.8}$$

where D_m is the m-th species molecular diffusion coefficient. Gradients of temperature and pressure can also produce species diffusion (Soret and Dufour effects, respectively) but these two contributions are neglected in this work.

The viscosity is given by Sutherland's law:

$$\frac{\mu}{\mu_0} = \frac{T^{3/2}}{T_S + T} \tag{2.9}$$

where μ_0 is the reference viscosity at T_0 and $T_S = 110.4\ K$.

Mass conservation can be represented by the following equations:

$$\sum_{m=1}^{N} Y_m = 1.0 \tag{2.10}$$

$$\sum_{m=1}^{N} V_{im} = 0.0, i = 1, 2, 3 \tag{2.11}$$

2.1.2 *LES* Governing Equations

In the *LES* methodology, the large scale motion is fully resolved on the computational grid using a time- and space-discretization scheme and only the small scales are modeled. The separation between the large (resolved) and the small (unresolved) scales is determined by the grid size ($\overline{\Delta}$). A Favre spatial top-hat filter (which is appropriate for the finite-volume scheme employed here) is employed to derive the LES equations Erlebacher et al. [1992].

The Favre average of a LES-resolved function f ($\widetilde{f}$) is computed as:

$$\widetilde{f} = \frac{\overline{\rho f}}{\overline{\rho}} \tag{2.12}$$

The over-bar represents the spatial filtering defined as:

$$\overline{f(\vec{x},t)} = \int_D f(\vec{x'},t) G_f(\vec{x},\vec{x'}) d\vec{x'} \tag{2.13}$$

where D is the entire computational domain, $\vec{x}$ is the position vector and G_f is the top-hat filter kernel defined as:

$$G_f(\vec{x},\vec{x'}) = \begin{cases} \frac{1}{\overline{\Delta}} & |\vec{x}-\vec{x'}| < \frac{\overline{\Delta}}{2} \\ 0 & otherwise \end{cases}$$

Thus, any variable (f) is decomposed into a resolved quantity ($\widetilde{f}$) and a unresolved quantity (f'') such that $f = \widetilde{f} + f''$. More details regarding the LES filtering and the different techniques are given in Ghosal [1993] and Pope [2000]. Using this technique to the set of equations 2.1, we obtain the filtered Navier-Stockes equations, i.e. the LES governing equations:

$$\begin{cases} \frac{\partial \overline{\rho}}{\partial t} + \frac{\partial \overline{\rho}\widetilde{u_i}}{\partial x_i} = 0 \\ \frac{\partial \overline{\rho}\widetilde{u_i}}{\partial t} + \frac{\partial}{\partial x_j}\Big[\overline{\rho}\widetilde{u_i}\widetilde{u_j} + \overline{p}\delta_{ij} - \overline{\tau_{ij}} + \tau_{ij}^{sgs}\Big] = 0 \\ \frac{\partial \overline{\rho}\widetilde{E}}{\partial t} + \frac{\partial}{\partial x_i}\Big[\Big(\overline{\rho}\widetilde{E} + \overline{p}\Big)\widetilde{u_i} + \overline{q_i} - \widetilde{u_j}\overline{\tau_{ji}} + H_i^{sgs} + \sigma_i^{sgs}\Big] = 0 \\ \frac{\partial \overline{\rho}\widetilde{Y_m}}{\partial t} + \frac{\partial}{\partial x_j}\Big[\overline{\rho}\widetilde{Y_m}\widetilde{u_j} + \overline{\rho D_m}\frac{\partial \widetilde{Y_m}}{\partial x_j} + \Phi_{j,m}^{sgs} + \Theta_{jm}^{sgs}\Big] = \overline{\rho}\widetilde{\dot{w}}_m \text{ , where m = 1,N} \end{cases} \tag{2.14}$$

The subgrid terms resulting from the filtering operation are denoted by the superscript sgs and represent the effect of the small (unresolved) scales structures on the resolved variables. This formulation introduces the subgrid turbulent kinetic energy (k^{sgs}) representing the unresolved turbulent motion of the fluid. The total energy is now written as:

$$\widetilde{E} = \widetilde{e} + \frac{1}{2}\big(\widetilde{u_k}\widetilde{u_k}\big) + k^{sgs} \tag{2.15}$$

The filtered velocity $\widetilde{u_i}$ and temperature $\widetilde{T}$ are used to approximate $\overline{\tau}_{ij}$ and $\overline{q}_i$:

$$\overline{\tau}_{ij} = \mu\Big(\frac{\partial \widetilde{u_i}}{\partial x_j} + \frac{\partial \widetilde{u_j}}{\partial x_i}\Big) - \frac{2}{3}\mu\frac{\partial \widetilde{u_k}}{\partial x_k}\delta ij \tag{2.16}$$

In the same manner:

$$\overline{q_i} = -\overline{\kappa}\frac{\partial \widetilde{T}}{\partial x_i} + \overline{\rho}\sum_{k=1}^{N}\widetilde{h_k}\widetilde{Y_k}\widetilde{V_{ik}} + \sum_{k=1}^{N} q_{ik}^{sgs} \tag{2.17}$$

where the diffusion velocities are computed using the resolved gradient of the species mass fraction ($\widetilde{Y_k}$) and q_{ik}^{sgs} represents the heat transfer via turbulent convection of species. To summarize, five more terms are unclosed and need to be modeled: τ_{ij}^{sgs}, H_i^{sgs}, σ_i^{sgs}, $\Phi_{j,m}^{sgs}$ and Θ_{jm}^{sgs}. These terms are, respectively, the subgrid shear stress tensor, subgrid heat flux, subgrid viscous stress, subgrid mass flux and subgrid diffusive mass flux, and are defined as follows:

$$\begin{cases} \tau_{ij}^{sgs} = \overline{\rho}\Big[\widetilde{u_i u_j} - \widetilde{u}_i\widetilde{u}_j\Big] \\ H_i^{sgs} = \overline{\rho}\Big[\widetilde{E u_i} - \widetilde{E}\widetilde{u}_i\Big] + \Big[\overline{p u_i} - \overline{p}\widetilde{u}_i\Big] \\ \sigma_i^{sgs} = \widetilde{u_j\tau_{ji}} - \widetilde{u}_j\overline{\tau_{ji}} \\ \Phi_{jm}^{sgs} = \overline{\rho}\Big[\widetilde{Y_m u_j} - \widetilde{Y_m}\widetilde{u}_j\Big] \\ \Theta_{jm}^{sgs} = \overline{\rho}\Big[Y_m\widetilde{V_{j,m}} - \widetilde{Y_m}\widetilde{V_{j,m}}\Big] \\ q_{jm}^{sgs} = \Big[\overline{h_m D_m\frac{\partial Y_m}{\partial x_j}} - \widetilde{h_m}\widetilde{D_m}\frac{\partial \widetilde{Y_m}}{\partial x_j}\Big] \end{cases} \tag{2.18}$$

The filtered equation of state is used to compute the filtered pressure:

$$\overline{p} = \overline{\rho}R_u\sum_{m=1}^{N}\frac{\widetilde{Y_m}}{MW_m}\widetilde{T} + \frac{\widetilde{Y_m T} - \widetilde{Y_m}\widetilde{T}}{MW_m} \tag{2.19}$$

It was proved (Fureby [1995], Veynante et al. [1996]) that $T^{sgs} = \frac{\widetilde{Y_m T} - \widetilde{Y_m}\widetilde{T}}{MW_m}$ can be neglected. Therefore, $\overline{p}=\overline{\rho}R\widetilde{T}$.

2.1.3 Subgrid Closure of the LES Equations

The closure of subgrid terms is a major area of research and many approaches have been proposed in the past. In general, since the small scales primarily provide dissipation for the energy that cascades from the large scales through the inertial range, an eddy viscosity type subgrid model appears appropriate to model the subgrid stresses τ_{ij}^{sgs}, heat flux H_i^{sgs} and species flux Φ_{jm}^{sgs}. Assuming that an eddy viscosity ν_T can be prescribed, these subgrid fluxes can be approximated as:

$$\begin{cases} \tau_{ij}^{sgs} = -2\nu_T\left(\frac{\partial \widetilde{u}_i}{\partial x_j} + \frac{\partial \widetilde{u_j}}{\partial x_i}\right) \\ H_i^{sgs} = -\nu_T \frac{\partial \widetilde{h}}{\partial x_i} \\ \Phi_{jm}^{sgs} = -D_T\left(\frac{\partial \widetilde{Y_m}}{\partial x_j}\right) \end{cases} \tag{2.20}$$

Here, $\widetilde{h}$ is the specific enthalpy and $D_T = \nu_T/Sc_t$ is the eddy diffusivity obtained in terms of the eddy viscosity and a turbulent Schmidt number Sc_t (assumed to be unity here). The subgrid diffusive mass flux (Θ_{jm}^{sgs}) and the subgrid heat conduction via turbulent species convection (q_{jm}^{sgs}) are neglected in this study. The closure for the subgrid viscous stress σ_i^{sgs} will be described later. Finally, the closures of the filtered reaction rate $\widetilde{\dot{w}}_m$ is described later. To obtain the subgrid eddy viscosity ν_T, a characteristic subgrid length scale L^{sgs} and a characteristic subgrid velocity scale V^{sgs} for the unresolved scales of motion must be identified and prescribed. The simplest model for ν_T is $\nu_T = C_\nu L^{sgs} V^{sgs}$. Here, C_ν is a coefficient of proportionality. In LES, the grid resolution $\overline{\Delta}$ is typically chosen as the characteristic length scale of the smallest resolved (or alternatively, the largest unresolved) eddy. However, it must be pointed out that, numerically, the smallest eddy that can be resolved requires at least 3-4 grid points which implies that this choice is not necessarily correct but is within the range of acceptable length scales.

Subgrid models for eddy viscosity differ primarily in the prescription of the velocity scale, V^{sgs}. Earlier LES studies Smagorinsky [1993] used the resolved strain rate $\widetilde{S_{ij}} = \frac{1}{2}(\frac{\partial \widetilde{u}_i}{\partial x_j} + \frac{\partial \widetilde{u_j}}{\partial x_i})$ and $\overline{\Delta}$ to obtain V^{sgs} such that $V^{sgs} = \overline{\Delta} S$ where $S = (\widetilde{S_{ij}}\widetilde{S_{ij}})^{1/2}$. With this closure, an algebraic eddy viscosity model is obtained and such a model has been employed in many simulations in the past. However, a limitation of this model is that the formal derivation of this eddy viscosity expression requires that production and dissipation of the turbulent kinetic energy to be in equilibrium. Since this requirement is only satisfied in the dissipation scales range, proper application of the algebraic model requires for the entire inertial range to be well resolved. This requirement is very severe for high-Re flows since the overall grid resolution required to meet this criteria can exceed available computational resource by a substantial amount. Therefore, for complex, high-Re flows an alternate choice of the velocity scale is needed.

In this work, a transport model for the subgrid kinetic energy k^{sgs} is employed to obtain V^{sgs}. More precisely:

$$\nu_t = C_\nu \sqrt{k^{sgs}}\Delta \tag{2.21}$$

The next section discusses the governing equation of the subgrid kinetic energy (k^{sgs}).

2.1.4 Subgrid Turbulent Kinetic Energy Model

A transport equation is formally derived for k^{sgs} and solved along with he rest of the LES equations. Since k^{sgs} evolves locally and temporally in the flow, the equilibrium assumption is relaxed and the cutoff between the resolved and the unresolved scales can be in the inertial range instead of the dissipation range, hence, a relatively coarse grid can be used to simulate high-Re flows. Past studies Menon et al. [1996], Kim and Menon [1999], Kim et al. [1999], Kim and Menon [2000] have demonstrated the ability and accuracy of this model.

The k^{sgs} transport model is given as:

$$\frac{\partial \overline{\rho} k^{sgs}}{\partial t} + \underbrace{\frac{\partial}{\partial x_i}\left(\overline{\rho}\widetilde{u}_i k^{sgs}\right)}_{I} + \underbrace{\frac{\partial}{\partial x_i}\left(\widetilde{\rho k u_i} - \overline{\rho}\widetilde{k}\widetilde{u}_i\right)}_{II} =$$
$$\underbrace{-\left(\overline{u_i \frac{\partial p}{\partial x_i}} - \widetilde{u}_i \frac{\partial \overline{p}}{\partial x_i}\right)}_{III} \underbrace{-\left(\widetilde{u_i \frac{\partial \tau_{ij}}{\partial x_i}} - \widetilde{u}_i \frac{\partial \overline{\tau_{ij}}}{\partial x_i}\right)}_{IV} \underbrace{-\frac{\partial}{\partial x_i}\left(\widetilde{u}_j \tau_{ij}^{sgs}\right)}_{V} \underbrace{-\tau_{ij}^{sgs}\frac{\partial \widetilde{u}_j}{\partial x_i}}_{VI} \tag{2.22}$$

where $k{=}\frac{1}{2}\widetilde{u_k}\widetilde{u_k}$. Here, the subgrid kinetic energy is defined as $k^{sgs} = \frac{1}{2}\left[\widetilde{u_k^2} - \widetilde{u_k}^2\right]$. k^{sgs} is resolved at the LES level but represents a subgrid quantity. Therefore, the governing equation for $\widetilde{k^{sgs}}$ is given above. However, for simplicity, the resolved subgrid turbulent energy will be denoted k^{sgs} instead of $\widetilde{k^{sgs}}$.

The different terms of Eq. 2.22 are the resolved convection (I), the subgrid turbulent convection (II, III and IV), the turbulent energy dissipation (V) and production (VI). Again, terms (II) to (VI) require closure.

The three subgrid turbulent convection terms are combined into one term and modeled as:

$$\text{Subgrid turbulent convection} \approx \frac{\partial}{\partial x_i}\Big(\overline{\rho}\frac{(\nu+\nu_t)}{Pr_t}\frac{\partial k^{sgs}}{\partial x_i}\Big) \tag{2.23}$$

Here, and Pr_y is a turbulent Prandtl number. The production of subgrid turbulent kinetic energy (P^{sgs}) is a function of the subgrid stress tensor:

$$P^{sgs} = -\tau_{ij}^{sgs}\frac{\partial \widetilde{u_i}}{\partial \widetilde{x_j}} \tag{2.24}$$

The subgrid stress tensor is modeled as:

$$\tau_{ij}^{sgs} = -2\overline{\rho}\nu_T\Big(\widetilde{S_{ij}} - \frac{1}{3}\widetilde{S_{kk}}\delta_{ij}\Big) + \frac{2}{3}\overline{\rho}k^{sgs}\delta_{ij} \tag{2.25}$$

The dissipation of subgrid turbulent kinetic energy (D^{sgs}) is derived following the scaling law of the turbulence dissipation ϵ. ϵ can be related to the level of velocity fluctuations u' and the characteristic length scale $\overline{\Delta}$:

$$\epsilon \approx \frac{u'^3}{\overline{\Delta}} \tag{2.26}$$

Using the analogy between ϵ and k^{sgs}:

$$D^{sgs} = C_\epsilon\overline{\rho}\frac{\sqrt{(k^{sgs})^3}}{\overline{\Delta}} \tag{2.27}$$

To summarize:

$$\frac{\partial\overline{\rho}\widetilde{k^{sgs}}}{\partial t} + \frac{\partial}{\partial x_i}\Big(\overline{\rho}\widetilde{u_i}\widetilde{k^{sgs}}\Big) = \frac{\partial}{\partial x_i}\Big(\overline{\rho}\frac{(\nu+\nu_t)}{Pr_t}\frac{\partial k^{sgs}}{\partial x_i}\Big) - \tau_{ij}^{sgs}\frac{\partial\widetilde{u_i}}{\partial\widetilde{x_j}} - C_\epsilon\overline{\rho}\frac{\sqrt{(k^{sgs})^3}}{\overline{\Delta}} \tag{2.28}$$

There are two model coefficients C_ϵ and C_ν that must be prescribed or obtained dynamically as a part of the solution Kim and Menon [1995], Kim et al. [1998].

2.1.5 Localized Dynamic k^{sgs} Model ($LDKM$)

In the above paragraph, C_ϵ and C_ν are prescribed as constant. However, these two coefficients vary throughout the flow. This coefficients can be dynamically computed as a part of the solution and this technique is described in this section.

This model was developed by Kim and Menon [1995] for incompressible flows and was extended by Nelson [1997] for compressible flows. This model was used with success in

many studies of non-reacting flows Menon and Kim [1996], Patel et al. [2003] as well as in studies of reacting flows Kim et al. [1999], Kim and Menon [2000]. The $LDKM$ is not the only method available for the dynamic evaluation of C_ϵ and C_ν: another similar model was developed by Germano et al. [1991]. However, the $LDKM$ presents the advantage that no far-reaching spatial averages are required, i.e. the $LDKM$ model is easily implementable in complex geometries.

The idea behind the $LDKM$ model is to assume that the behavior of the resolved small scales is comparable to the behavior of the unresolved scales and, thus, the model coefficients can be computed using similarity relations. This is done by defining a $test-filter$, denoted $\widehat{}$, which filters these small, but resolved, scales. Usually, this $test-filter$ is taken as twice the LES resolution, i.e. $\widehat{\Delta}=2\overline{\Delta}$. Once the turbulence quantities are known at the $test-filter$ level, the LES model coefficients are extracted by comparing quantities resolved at $\overline{\Delta}$.

2.1.5.1 Computation of C_ν

We consider the subgrid stress tensor τ_{ij}^{sgs}:

$$\tau_{ij}^{sgs} = \overline{\rho}(\widetilde{u_i u_j} - \widetilde{u}_i\widetilde{u}_j) = -2\overline{\rho}C_\nu\sqrt{k^{sgs}}\overline{\Delta}\Big(\widetilde{S_{ij}} - \frac{1}{3}\widetilde{S_{kk}}\delta_{ij}\Big) + \frac{2}{3}\overline{\rho}k^{sgs}\delta_{ij} \tag{2.29}$$

Using the $test-filter$, it is possible to construct an expression similar to Eq. 2.29:

$$\begin{aligned}\tau_{ij}^{sgs,test} = \widehat{\overline{\rho}\widetilde{u}_i\widetilde{u}_j} - \frac{\widehat{\overline{\rho}\widetilde{u}_i}\widehat{\overline{\rho}\widetilde{u}_j}}{\widehat{\overline{\rho}}} \approx -2C_\nu\widehat{\Delta}\widehat{\overline{\rho}}\Big(\frac{\widehat{\overline{\rho}\widetilde{u_k u_k}}}{2\widehat{\overline{\rho}}} - \frac{\widehat{\overline{\rho}\widetilde{u}_k}}{4\widehat{\overline{\rho}}\widehat{\overline{\rho}}}\Big)^{\frac{1}{2}}\Big(\widehat{\widetilde{S_{ij}}} - \frac{1}{3}\widehat{\widetilde{S_{kk}}}\delta_{ij}\Big) \\ +\frac{1}{3}\Big(\widehat{\overline{\rho}\widetilde{u_k u_k}} - \frac{\widehat{\overline{\rho}\widetilde{u}_k}\widehat{\overline{\rho}\widetilde{u}_k}}{\widehat{\overline{\rho}}}\Big)\delta_{ij}\end{aligned} \tag{2.30}$$

where $\widehat{\widetilde{S_{ij}}}$ is defined as:

$$\widehat{\widetilde{S_{ij}}} = \frac{1}{2}\Big[\frac{\partial}{\partial x_i}\Big(\frac{\widehat{\overline{\rho}\widetilde{u}_j}}{\widehat{\overline{\rho}}}\Big) + \frac{\partial}{\partial x_j}\Big(\frac{\widehat{\overline{\rho}\widetilde{u}_i}}{\widehat{\overline{\rho}}}\Big)\Big] \tag{2.31}$$

C_ν can not be extracted directly from Eq. 2.30. Lilly [1992] proposed a method that formulate an expression for the subgrid stress tensor E_{ij} and the minimize it with respect to C_ν. E_{ij} can be written as:

$$\begin{aligned}E_{ij} = \widehat{\overline{\rho}\widetilde{u}_j\widetilde{u}_i} - \frac{\widehat{\overline{\rho}\widetilde{u}_j}\widehat{\overline{\rho}\widetilde{u}_i}}{\widehat{\overline{\rho}}} - \frac{1}{3}\Big(\widehat{\overline{\rho}\widetilde{u_k u_k}} - \frac{\widehat{\overline{\rho}\widetilde{u}_k}\widehat{\overline{\rho}\widetilde{u}_k}}{\widehat{\overline{\rho}}}\Big)\delta_{ij} + \\ 2C_\nu\widehat{\Delta}\widehat{\overline{\rho}}\Big(\frac{\widehat{\overline{\rho}\widetilde{u_k u_k}}}{2\widehat{\overline{\rho}}} - \frac{\widehat{\overline{\rho}\widetilde{u}_k}}{2\widehat{\overline{\rho}}}\frac{\widehat{\overline{\rho}\widetilde{u}_k}}{2\widehat{\overline{\rho}}}\Big)^{\frac{1}{2}}\Big(\widehat{\widetilde{S_{ij}}} - \frac{1}{3}\widehat{\widetilde{S_{kk}}}\delta_{ij}\Big)\end{aligned} \tag{2.32}$$

which can be more simply expressed as:

$$E_{ij} = L_{ij} + 2C_\nu D_{ij} \tag{2.33}$$

where L_{ij} and D_{ij} are the exact and modeled $test-filter$ subgrid stress tensor, respectively:

$$\begin{aligned} L_{ij} &= \widehat{\overline{\rho}\widetilde{u_j}\widetilde{u_i}} - \frac{\widehat{\overline{\rho}\widetilde{u_j}}\widehat{\overline{\rho}\widetilde{u_i}}}{\widehat{\overline{\rho}}} - \frac{1}{3}\Big(\widehat{\overline{\rho}\widetilde{u_k}\widetilde{u_k}} - \frac{\widehat{\overline{\rho}\widetilde{u_k}}\widehat{\overline{\rho}\widetilde{u_k}}}{\widehat{\overline{\rho}}}\Big)\delta_{ij} \\ D_{ij} &= \widehat{\Delta}\widehat{\overline{\rho}}\Big(\frac{\widehat{\overline{\rho}\widetilde{u_k}\widetilde{u_k}}}{2\widehat{\overline{\rho}}} - \frac{\widehat{\overline{\rho}\widetilde{u_k}}}{2\widehat{\overline{\rho}}}\frac{\widehat{\overline{\rho}\widetilde{u_k}}}{2\widehat{\overline{\rho}}}\Big)^{\frac{1}{2}}\Big(\widehat{\widetilde{S_{ij}}} - \frac{1}{3}\widehat{\widetilde{S_{kk}}}\delta_{ij}\Big) \end{aligned} \tag{2.34}$$

E_{ij} can be positive or negative and it is easier to minimize its rms error, in other words, the derivative of $E_{ij}E_{ij}$ with respect to C_ν must be zero:

$$\frac{\partial E_{ij}E_{ij}}{\partial C_\nu} = 4D_{ij}L_{ij} + 8C_\nu D_{ij}L_{ij} = 0 \tag{2.35}$$

Thus:

$$C_\nu = -\frac{D_{ij}L_{ij}}{2D_{ij}D_{ij}} \tag{2.36}$$

2.1.5.2 Computation of C_ϵ

For the computation of this coefficient, an expression for the rate of k^{sgs} dissipation ϵ is needed. The viscous term can be expressed as:

$$\begin{aligned} \overline{u_i\frac{\partial \tau_{ij}}{\partial x_j}} - \overline{u_i}\frac{\partial \overline{\tau_{ij}}}{\partial x_j} = &\overline{u_j\frac{\partial}{\partial x_i}\Big[\mu\Big(\frac{\partial u_i}{\partial x_j} + \frac{\partial u_i}{\partial x_j}\Big) - \frac{2}{3}\mu\frac{\partial u_k}{\partial x_k}\delta_{ij}\Big]} \\ &-\widetilde{u_j}\overline{\Big[\mu\Big(\frac{\partial u_i}{\partial x_j} + \frac{\partial u_i}{\partial x_j}\Big) - \frac{2}{3}\mu\frac{\partial u_k}{\partial x_k}\delta_{ij}\Big]} \end{aligned} \tag{2.37}$$

Note that, in the above equation, the over-bar sign ($\overline{()}$) has been used in place of the standard tilde for formatting purposes.

For incompressible systems, the viscosity is assumed to be locally invariant, i.e. the fluctuations of μ at the small scales are ignored. This assumption is only used for the computation of C_ϵ. This assumption is supported by the fact that both the resolved and subgrid viscous terms are usually small when compared to the convective terms in high-Reynolds flows Nelson [1997]. As a result, Eq. 2.37 can be simplified:

$$\overline{u_i\frac{\partial\tau_{ij}}{\partial x_j}}-\overline{u_i}\frac{\partial\overline{\tau_{ij}}}{\partial x_j}\approx-\overline{\mu}\Big[\overline{\Big(\frac{\partial u_j}{\partial x_i}\Big)^2}-\Big(\frac{\partial\overline{u_j}}{\partial x_i}\Big)^2+\frac{\partial^2}{\partial {x_i}^2}\Big(\overline{\frac{u_ju_j}{2}}-\frac{\overline{u_j}\,\overline{u_j}}{2}\Big)\Big]$$
$$-\overline{\mu}\Big[\Big(\overline{\frac{\partial u_j}{\partial x_i}\frac{\partial u_i}{\partial x_j}}-\frac{\partial\overline{u_j}}{\partial x_i}\frac{\partial\overline{u_i}}{\partial x_j}\Big)-\frac{2}{3}\Big(\overline{\frac{\partial u_i}{\partial x_i}\frac{\partial u_j}{\partial x_j}}-\frac{\partial\overline{u_i}}{\partial x_i}\frac{\partial\overline{u_j}}{\partial x_j}\Big)\Big]$$
$$+\overline{\mu}\Big[\frac{\partial}{\partial x_i}\Big(\overline{u_j\frac{\partial u_i}{\partial x_j}}-\overline{u_j}\frac{\partial\overline{u_i}}{\partial x_j}\Big)-\frac{2}{3}\Big(\frac{\partial}{\partial x_i}\Big(\overline{u_j}\frac{\partial u_j}{\partial x_j}-\overline{u_i}\frac{\partial\overline{u_j}}{\partial x_j}\Big)\Big)\Big] \tag{2.38}$$

Here also, the over-bar sign ($\overline{()}$) has been used in place of the standard tilde for formatting purposes.

The first two terms on the right hand side of the previous equation are the dissipation and viscous transport terms, respectively. The two last terms arise from compressibility and acts as an additional dissipation and viscous transport terms, respectively Nelson [1997].

It is expected that the Mach number is very low in simulation of combustion chambers thus, the compressibility effect is of relative low importance. Therefore, we can simplify Eq. 2.38:

$$\epsilon\approx\widetilde{\mu}\Big(\widetilde{\frac{\partial u_j}{\partial x_i}}\frac{\partial u_j}{\partial x_i}-\frac{\partial\widetilde{u_j}}{\partial x_i}\frac{\partial\widetilde{u_j}}{\partial x_i}\Big)\approx\overline{\rho}C_\epsilon\frac{(k^{sgs})^{\frac{3}{2}}}{\overline{\Delta}} \tag{2.39}$$

Following the same idea, an expression for ϵ at the $test-filter$ level can be derived:

$$\epsilon\approx\widehat{\mu}\Big[\widehat{\frac{\partial\widetilde{u_j}}{\partial x_i}}\frac{\partial\widetilde{u_j}}{\partial x_i}-\frac{\partial}{\partial x_i}\Big(\frac{\widehat{\overline{\rho}\widetilde{u_j}}}{\widehat{\overline{\rho}}}\Big)\frac{\partial}{\partial x_i}\Big(\frac{\widehat{\overline{\rho}\widetilde{u_j}}}{\widehat{\overline{\rho}}}\Big)\Big]\approx\frac{C_\epsilon\widehat{\overline{\rho}}}{\widehat{\Delta}}\Big(\frac{\widehat{\overline{\rho}\widetilde{u_k}\widetilde{u_k}}}{2\widehat{\overline{\rho}}}-\frac{\widehat{\overline{\rho}\widetilde{u_k}}}{2\widehat{\overline{\rho}}}\frac{\widehat{\overline{\rho}\widetilde{u_k}}}{\widehat{\overline{\rho}}}\Big)^{\frac{3}{2}} \tag{2.40}$$

Rewriting Eq. 2.40 leads to:

$$C_\epsilon=\frac{\widehat{\mu}\widehat{\Delta}}{\widehat{\overline{\rho}}}\frac{\Big[\widehat{\frac{\widetilde{u_j}}{\partial x_i}\frac{\widetilde{u_j}}{\partial x_i}}-\frac{\partial}{\partial x_i}\Big(\frac{\widehat{\overline{\rho}\widetilde{u_j}}}{\widehat{\overline{\rho}}}\Big)\frac{\partial}{\partial x_i}\Big(\frac{\widehat{\overline{\rho}\widetilde{u_j}}}{\widehat{\overline{\rho}}}\Big)\Big]}{\Big[\frac{\widehat{\overline{\rho}\widetilde{u_k}\widetilde{u_k}}}{2\widehat{\overline{\rho}}}-\frac{\widehat{\overline{\rho}\widetilde{u_k}}}{2\widehat{\overline{\rho}}}\frac{\widehat{\overline{\rho}\widetilde{u_k}}}{\widehat{\overline{\rho}}}\Big]^{\frac{3}{2}}} \tag{2.41}$$

2.1.5.3 Constraints on Realizability

The value of C_ν must be constrained such that τ_{ij}^{sgs} is positive and finite Nelson [1997]. Several conditions are used to satisfy these constraints Vreman et al. [1994]:

$$
\begin{aligned}
\tau_{11}^{sgs} &\geq 0 \\
\tau_{22}^{sgs} &\geq 0 \\
\tau_{33}^{sgs} &\geq 0 \\
|\ \tau_{12}^{sgs}\ |^2 &\leq \tau_{11}^{sgs}\tau_{22}^{sgs} \\
|\ \tau_{13}^{sgs}\ |^2 &\leq \tau_{11}^{sgs}\tau_{33}^{sgs} \\
|\ \tau_{23}^{sgs}\ |^2 &\leq \tau_{22}^{sgs}\tau_{33}^{sgs} \\
det(\tau_{ij}^{sgs}) &\leq 0
\end{aligned}
\tag{2.42}
$$

Note that these conditions are satisfied for the vast majority of the computational domain Nelson [1997].

2.2 Combustion Modeling

In this study, we distinguish between the model needed to predict the flame structure (and its propagation characteristics) and the model needed to predict pollutant emission. To predict the overall heat release, the flame structure and its propagation, we use two different approaches. In the first approach (level set approach Peters [2000]), the premixed flame front is represented by an infinitely thin surface that is advected by the turbulent flow in the 3D LES grid while propagating normal to itself at a characteristic flame speed S_F. This approach is called $GLES$ hereafter. The second approach uses a simplified chemical mechanism and resolves the governing equations of each species at a sub-LES level. This closure is known as the Linear-Eddy Mixing (LEM) subgrid closure model. The technique, when applied as a LES closure, is called $LEMLES$, hereafter, and is described in section 2.2.2.

2.2.1 Combustion Modeling: Level Set Approach ($GLES$ Model)

The G-equation model is a flamelet model where G(x,t) represents the distance from any point to the flame front. The G-field is a non-reactive field propagating perpendicular to itself at a given flame speed. The flame surface corresponds to the isosurface $G(x,t) = G_0$. $G(x,t)>G_0$ corresponds to the unburnt reactants and $G(x,t)<G_0$ corresponds to the burnt products. The G-Field governing equation (aka G-equation) is:

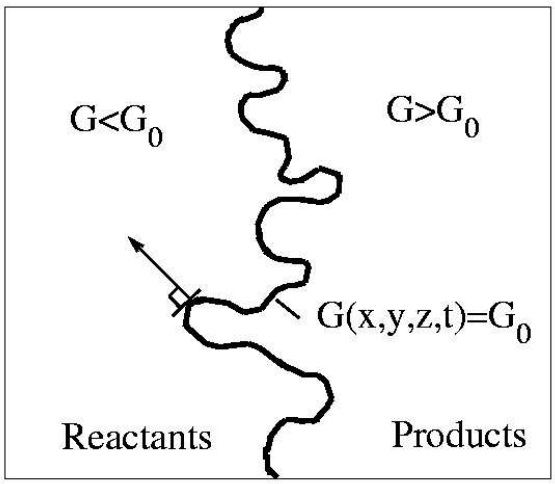

Figure 2.1: Schematic representation of the flame front in the G-equation level approach

By differentiating $G(x,t) = G_0$ with respect to time, we obtain:

$$\frac{\partial G}{\partial t} + \nabla G \cdot \frac{d\vec{x}}{dt}\Big|_{G=G_0} = 0 \tag{2.43}$$

The flame is convected by the flow at a speed $\vec{v}$ and propagates normal to itself at a speed $S_L^0\vec{n}$. Therefore:

$$\frac{d\vec{x}}{dt}\Big|_{G=G_0} = \vec{v} + S_L\vec{n} \tag{2.44}$$

Here, S_L is the laminar flame speed and differs from the unstretched laminar flame speed S_L^0, S_L takes into account the flame curvature and stretching. This correction is now described.

Finally:

$$\frac{\partial G}{\partial t} + \vec{v}\nabla G = -S_L\Big|\nabla G\Big| \tag{2.45}$$

or, written in a tensor notation:

$$\frac{\partial G}{\partial t} + u_i\frac{\partial G}{\partial x_i} = -S_L\Big|\nabla G\Big| \tag{2.46}$$

The correction for flame strain and flame curvature was derived by Pelce and Clavin [1982] and is valid for small values of both curvature and strain. The expression for the modified propagating speed (S_L) is:

$$S_L = S_L^0 - S_L^0\mathscr{L}\kappa - \mathscr{L}S \tag{2.47}$$

where κ is the flame curvature and S is the flow strain rate imposed on the flame by the flow velocity gradients. The strain rate is computed as:

$$S = -\vec{n} \cdot \nabla \vec{v} \cdot \vec{n} \tag{2.48}$$

where $\vec{v}$ is the flow velocity vector. The flame curvature term is computed as:

$$\kappa = \nabla \vec{n} = \nabla \Big(- \frac{\nabla G}{|\nabla G|} \Big) = - \frac{\nabla^2 G - \vec{n} \cdot (\vec{n} \cdot \nabla G)}{|\nabla G|} \tag{2.49}$$

The Markstein length ($\mathscr{L}$) is proportional to the flame thickness δ_F. The proportionality coefficient is called the Markstein number $\mathscr{M}$ and is of the order of magnitude of 1. More information on the computation of the $\mathscr{M}$ can be found in Clavin [1985].

Using the fact that $\vec{n}$=$-\nabla G/|\nabla G|$ and multiplying every term by the density ρ, we obtain the G-Equation formula:

$$\frac{\partial \rho G}{\partial t} + \frac{\partial}{\partial x_i} \Big(\rho u_i G \Big) = -\rho S_L |\nabla G| \tag{2.50}$$

Once filtered at the LES level, the G-equation becomes:

$$\frac{\partial \bar{\rho} \widetilde{G}}{\partial t} + \frac{\partial}{\partial x_i} \Big(\overline{\rho} \widetilde{u_i} \widetilde{G} \Big) = - \frac{\partial}{\partial x_i} \overline{\rho} \Big(\widetilde{u_i G} - \widetilde{u_i} \widetilde{G} \Big) - \overline{\rho S_L |\nabla G|} \tag{2.51}$$

The flame front propagation term $\overline{\rho S_L |\nabla G|}$ is modeled as $\overline{\rho} S_F |\nabla \widetilde{G}|$ where S_F is the flame speed propagation. S_F depends upon the combustion regime. In laminar uniform flows, S_F is equal to the unstretched laminar flame propagation speed S_L^0. In laminar non-uniform flows, S_F is equal to the laminar flame propagation speed S_L. In turbulent flows, S_F is taken as the turbulent flame speed S_T which has to be modeled. The model used in this study takes into account the increase in reaction rate caused by the increase in subgrid flame surface caused by subgrid velocity fluctuations (u'=$\sqrt{(2/3) k^{sgs}}$). The model used in this study was developed by Pocheau [1992]:

$$S_T = S_L^0 \Big(1 + \beta \Big(\frac{u'}{S_L^0} \Big)^2 \Big)^{\frac{1}{2}} \tag{2.52}$$

where β is a constant that is usually set to 20 Chen.Y.C. et al. [1996] and u'/S_L^0 is limited by a maximum value ζ. ζ is usually set to 16.56. One could expect that S_L and not S_L^0 would be used in Eq. 2.52. However, Eq. 2.47 is not derived in the LES framework. κ, S and $\mathscr{L}$

can not be computed, only $\widetilde{\kappa}$, $\widetilde{S}$ and $\widetilde{\mathscr{L}}$ can. The original terms can not be substituted by the LES filtered terms, hence, S_L^0 is used in the computation of the turbulent flame speed S_T.

Other turbulent flame speed models are also available. The above model was proved to be well-suited for numerical simulations of swirling flows. Another famous turbulent flame speed model was developed by Yakhot and it is interesting to note that this model provides a much lower value for S_T when compared to the model of Pocheau. Because Eq. 2.52 was proved to yield good results when used for simulation of flame propagation in swirling flows Kim et al. [1999], Stone and Menon [2001], this model is chosen for this study.

The unclosed term $\frac{\partial}{\partial x_i}\overline{\rho}\Big(\widetilde{u_i G} - \widetilde{u}_i\widetilde{G}\Big)$ can be modeled using a gradient diffusion model Kim et al. [1999], Stone and Menon [2001]. In this case:

$$\frac{\partial}{\partial x_i}\Big(\widetilde{u_i G} - \widetilde{u}_i\widetilde{G}\Big) = \overline{\rho} D_T \nabla\widetilde{G} \tag{2.53}$$

Finally:

$$\frac{\partial\overline{\rho}\widetilde{G}}{\partial t} + \frac{\partial}{\partial x_i}\Big(\overline{\rho}\widetilde{u}_i\widetilde{G}\Big) = \overline{\rho} S_T|\nabla G| - \overline{\rho} D_T\nabla\widetilde{G} \tag{2.54}$$

where, as before, $\overline{\rho} S_L|\nabla G| = \overline{\rho} S_T|\nabla G|$.

Peters [2000] argued that the gradient diffusion closure is not valid for the thin reaction zone Peters [2000]. Instead, Peters proposed the following governing equation for G:

$$\frac{\partial G}{\partial t} + \frac{\partial}{\partial x_i}\Big(\rho u_i G\Big) = (s_n + s_r)|\nabla G| - D\kappa|\nabla G| \tag{2.55}$$

where s_n is the contribution due to normal diffusion and s_r represents the displacement speed related to the reaction rate. More precisely, we have:

$$s_n = \frac{\vec{n}\cdot\nabla(\rho D\vec{n}\cdot\nabla G)}{\rho|\nabla G|} \tag{2.56}$$

$$s_r = \frac{\dot{w}}{\rho|\nabla G|} = S_L \tag{2.57}$$

The normal diffusion is already taken into account in the computation of S_L^0 and, therefore, $s_n = 0$. Obviously, $s_r = S_L|\nabla G|$. Thus:

$$\frac{\partial G}{\partial t} + \frac{\partial}{\partial x_i}\Big(\rho u_i G\Big) = S_L|\nabla G| - D\kappa|\nabla G| \tag{2.58}$$

Once filtered using the LES filter, the equation becomes:

$$\frac{\partial \overline{\rho}\widetilde{G}}{\partial t} + \frac{\partial}{\partial x_i}\Big(\overline{\rho}\widetilde{u_i}\widetilde{G}\Big) = -\frac{\partial}{\partial x_i}\overline{\rho}\Big(\widetilde{u_i G} - \widetilde{u_i}\widetilde{G}\Big) - \overline{\rho S_L^0 |\nabla G|} \tag{2.59}$$

where, as before, $\overline{\rho} S_L |\nabla G| = \overline{\rho} S_T |\nabla G|$. However, contrary to Eq. 2.54, the term $\frac{\partial}{\partial x_i}\overline{\rho}\Big(\widetilde{u_i G}\Big)$ is modeled differently:

$$\frac{\partial}{\partial x_i}\overline{\rho}\Big(\widetilde{u_i G}\Big) = \overline{\rho} D_T \widetilde{\kappa} |\nabla \widetilde{G}| \tag{2.60}$$

Finally:

$$\frac{\partial \overline{\rho}\widetilde{G}}{\partial t} + \frac{\partial}{\partial x_i}\Big(\overline{\rho}\widetilde{u_i}\widetilde{G}\Big) = \overline{\rho} S_T |\nabla G| - \overline{\rho} D_T \widetilde{\kappa} |\nabla \widetilde{G}| \tag{2.61}$$

The only difference between Eq. 2.54 and Eq. 2.61 is that the resolved flame curvature ($\widetilde{\kappa}$) is taken into account in Peter's approach. According to Stone [2004], there are no major differences between these two approaches but Peter's approach is more computationally expensive.

In this work, the G-equation was not implemented in a fully level-set approach. In this work, the G-field is not taken as a distance function but ranges between 0 and 1, where G=1 represents the unburnt reactants and G=0 represents the burnt products. The region where 0<G<1 is know as the flame brush and represents the average location of the thin flame surface over the LES integration time step Δt_{LES}.

On the other hand, if the value of G is not bounded and the flame surface is defined as G=G_0, G can be compared to a distance function. However, this distance function needs to be renormalized at every time step. The common method is to ensure that $|\nabla \widetilde{G}|$=1. The method developed by Russo and Smereka [1994] is widely used. The following equation is solved iteratively using a non-physical time t_1:

$$\begin{aligned} \frac{\partial \widetilde{G}}{\partial t_1} &= \quad sgn(\widetilde{G_0})(1 - |\nabla \widetilde{G}|) \\ \widetilde{G}(x,0) &= \qquad\quad \widetilde{G_0}(x) \end{aligned} \tag{2.62}$$

where $sgn(\widetilde{G_0})$ is a smooth sign function. The system is solved until a steady state is reached. When the steady state is reached:

$$|\nabla \widetilde{G}| = 1 \tag{2.63}$$

This solution was tested and was proved to be largely more computationally expensive and results were comparable to the other technique, where $0<G<1$. Therefore, this method was not used.

2.2.2 Combustion Modeling: Linear-Eddy Mixing Model ($LEMLES$ Model)

.

In model like the level set approach or the Eddy Break-Up models Fureby and Löfström [1994] , the subgrid processes (namely subgrid diffusion, subgrid convection and reaction) are modeled via the use of a mathematical model applied at the resolved (or LES) level. This can be sufficient when flames evolving in the wrinkled or corrugated flamelet regime are studied. But one could doubt the accuracy of such models when the combustion takes place in the TRZ or BRZ regime. In these turbulent premixed regimes, the interactions between the finest turbulent structures and the flame, as well as the molecular diffusion process, are of great importance. Unfortunately, these processes can not be resolved at the LES level. A resolution that would enable us to resolve all these critical processes would require an extremely large computational power that may not be available in the foreseeable future.

The main idea behind the Linear-Eddy Mixing model is to increase the grid resolution using a one dimensional computational domain instead of a three dimensional computational domain. If the resolution has to be increased by a factor F, using a one-dimensional domain increases the number of computational points by a factor of F while the more classic increase of resolution via the use of a three dimensional grid increases the number of point by a factor F^3. Considering that, for typical LES resolution, to resolve all relevant subgrid processes involved in the propagation of premixed flame in the TRZ or BRZ requires an increase of resolution of the order of 20, one understand why the use of a $1D$ computational domain as a subgrid domain is ratinal.

The LEM model was first developed by Kerstein [1988, 1989, 1991a,b]. The motivation was to accurately represents all the processes involved (large scale advection, small scales advection, molecular diffusion and chemical reaction) and to resolve them at their own time

and length scales. The main strength of this model is its ability to accurately reproduce the effect of $3D$ turbulence on a $1D$ scalar field. Therefore, the action of eddies of all relevant length scales can be modeled without using a DNS approach.

Numerous validations of the LEM model have been carried out Kerstein [1989, 1990, 1991a,b], Kerstein and Ashurst [1992], Kerstein [1992]. Naturally, LEM was considered as a subgrid model for LES of reacting flow. The idea is to include a LEM domain into each LES cells. The was first applied to non-premixed combustion by Menon et al. [1993]. Other studies were performed by McMurtry et al. [1992, 1993b,a], Calhoon and Menon [1996], Calhoon [1996], Smith and Menon [1998], Smith [1998], Chakravarthy and Menon [2000], Pannala and Menon [1998], Sankaran et al. [2003].

2.2.2.1 Description of the LEMLES Model

In the $LEMLES$ approach, all processes involved in turbulent mixing and combustion are explicitly included using a multi-scales approach. Large-scale advection has time and length scales much larger than combustion processes and only wrinkles the flame front. This effect is incorporated using a Lagrangian transport model that conserves mass exactly Kerstein [1991a] at the LES level. The action of LES unresolved turbulent structures via the stochastic re-arrangement of the species field by eddies provides a mechanism for additional subgrid wrinkling of the flame (in the flamelet regime), and results in an effective increase in the reactant consumption rate Smith and Menon [1996a]. In the TRZ regime, these small-scale eddies can penetrate into the preheat zone of the flame and promote heat transport ahead of the flame. In the BRZ regime, turbulent eddies can penetrate into flame reaction zone and modify its structure. In the $LEMLES$ approach Chakravarthy and Menon [2000, 2001a,b], these processes are explicitly included in the subgrid using a stirring process that mimics the effect of turbulent eddies on the scalar field Kerstein [1991a], Smith and Menon [1996a]. Although details of this procedure have been given elsewhere Kerstein [1991a], we summarize some of the salient features of this method.

Consider a transport model for a scalar Ψ and split the velocity field according to the

LES technique ($u_k = \widetilde{u_k} + u'_k$):

$$\frac{\partial \Psi}{\partial t} = -\widetilde{u_k}\frac{\partial \Psi}{\partial x_k} - u'_k\frac{\partial \Psi}{\partial x_k} + \frac{\partial}{\partial x_m}\Big(D_\Psi \frac{\partial \Psi}{\partial x_m}\Big) + \dot{w_\Psi} \tag{2.64}$$

where D_Ψ is the molecular diffusion coefficient and $\dot{w}_\Psi$ is the chemical source term. In $LEMLES$, the two-scale numerical procedure is represented as:

$$\frac{\Psi^* - \Psi^n}{\Delta t_{LES}} = -\widetilde{u_k}\frac{\partial \Psi^n}{\partial x_k} - \left(u'_k\right)^{face}\frac{\partial \Psi^n}{\partial x_k} \tag{2.65}$$

$$\Psi^{n+1} - \Psi^* = \int_t^{t+\Delta t_{LES}} \Big[u'_k\frac{\partial \Psi^n}{\partial x_k} + \frac{\partial}{\partial x_m}\Big(D_\Psi \frac{\partial \Psi^n}{\partial x_m}\Big) + \dot{w}_{\Psi^n}\Big]dt \tag{2.66}$$

Equation 2.65 describes the large-scale $3D$ Lagrangian LES-resolved convection of the scalar field and is implemented via the transfer of fluid between LES cells through the control volume surfaces (see sec. 2.2.3. The convection due to the subgrid velocity field through the control volume surfaces is represented by the term $\Big(\left(u'_k\right)^{face}\frac{\partial \Psi^n}{\partial x_k}\Big)$. Equation 2.66 describes the subgrid mixing $\Big(\int_t^{t+\Delta t_{LES}} u'_k\frac{\partial \Psi^n}{\partial x_k}dt\Big)$, the molecular diffusion $\Big(\int_t^{t+\Delta t_{LES}}\Big(D_\Psi\frac{\partial \Psi^n}{\partial x_m}\Big)dt\Big)$ and the chemical reaction rate $\Big(\int_t^{t+\Delta t_{LES}}\dot{w}_{\Psi^n}dt\Big)$ processes that occur within each LES cell during the LES integration time step (Δt_{LES}).

2.2.2.2 LEM Domain and Governing Equations

The LEM domain is a one-dimensional line. LEM domains are embedded in every LES cell. The number of LEM cells per LES cells is N^{LEM}. N^{LEM} is a function of the LES resolution and the level of turbulence. More information on the choice of N^{LEM} is given in section 6.4.1. The length of the LEM domain (L^{LEM}) is defined as:

$$L^{LEM} = \frac{\Delta V_{LES}^{\frac{1}{3}}}{N^{LEM}} \tag{2.67}$$

where ΔV_{LES} is the volume of the LES cell. The resolution on the LEM domain is uniform and the number of LEM grid point has to be larger than 6 and is conveniently chosen as a multiple of 3 (this is justified in section 2.2.3.2). LEM cells have a fixed volume (V^{LEM}) that is equal to the ration of V_{LES} over the number of LEM grid points. The LEM domain governing equations are shown below. Note that Eqs. 2.64 to 2.66 are not

geoverning equations but are only written here for illustration purposes:

$$\rho^{LEM}\frac{\partial Y_k^{LEM}}{\partial t} + F_k^{stir} + \underbrace{\rho_{LEM}\frac{\partial}{\partial s}\Big(-D_k\frac{\partial Y_k^{LEM}}{\partial s}\Big)}_{\text{species molecular diffusion}} = \underbrace{\dot{w}_k MW_k}_{\text{chemical reaction}} \tag{2.68}$$

$$\rho^{LEM}C_P\frac{\partial T^{LEM}}{\partial t} + F_T^{stir} - \underbrace{\sum_{k=1}^{N}\rho C_{P,k}D_k\Big(\frac{\partial Y_k^{LEM}}{\partial s}\Big)\Big(\frac{\partial T^{LEM}}{\partial s}\Big)}_{\text{diffusion of heat via species molecular diffusion}} - \underbrace{\frac{\partial}{\partial s}\Big(\overline{\kappa}\frac{\partial T^{LEM}}{\partial s}\Big)}_{\text{heat diffusion}} = \underbrace{-\sum_{k=1}^{N}h_k\dot{w}_k MW_k}_{\text{chemical reaction heat release}} \tag{2.69}$$

where Y^{LEM}, T^{LEM} and ρ^{LEM} are the subgrid LEM species mass fraction, temperature and density, respectively. s is the coordinate along the LEM line, D_k is the molecular diffusion coefficient of the $k-th$ species, $C_{P,k}$ is the specific heat coefficient per unit mass of the $k-th$ species, D_k is the ion coefficient of the $k-th$ species and MW_k is the molecular weight of the $k-th$ species. F_k^{stir} and F_T^{stir} are terms that represent the action of subgrid turbulence and are described in section 2.2.3.2.

A calorically perfect gas is assumed. Therefore, the pressure at the LEM level (P^{LEM}) is to be computed as follows:

$$P^{LEM} = \rho^{LEM}T^{LEM}\sum_{k=1}^{N}Y_k^{LEM}\frac{R_u}{MW_k} \tag{2.70}$$

However, P^{LEM} is not taken into account. ρ^{LEM} is computed using Eq. 2.70. However, only T^{LEM} is known and P^{LEM} has to be known in order to compute ρ^{LEM} and it is assumed that $P^{LEM} = P^{LES}$. This implies that pressure waves can not locally perturb a given LEM field. In absence of strong pressure gradients (e.g. shocks), this assumption is valid. Radiation is neglected in this study but can be included easily Zimberg et al. [1998] if desired.

As described in section 2.2.3, the LEM domain does not have any physical orientation. However, Kerstein Kerstein [1991b] demonstrated that the LEM $1D$ scalar fields can be considered as being oriented in the direction of maximum strain, i.e. perpendicular to the flame surface.

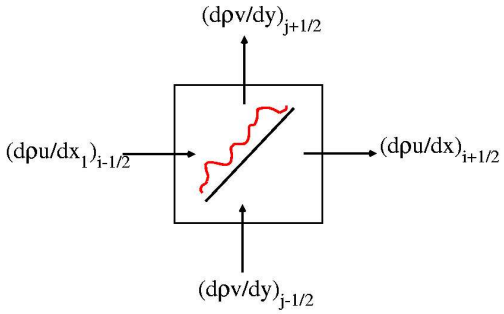

Figure 2.2: $2D$ representation of the LES cells, the LEM domain and the surface fluxes responsible for convection of the LEM scalars

2.2.3 Lagrangian Tracking of the Scalar Field - Splicing

As stated above, the scalar fields are tracked in a Lagragian manner inside the LES domain. Note that the LES scalar field is not known and only its distribution at the LEM level is known. The goal is to transport scalars from one LEM domain located in a given LES cell to another LEM domain located in another LES cell. The sufficiently small LES time step ensures that scalars are transported from one LES cell only to an adjacent LES cell, thus drastically reducing the complexity of the problem.

The transport of species across the LES domain is based on LES resolved quantities and is computed using the LES resolved transport of mass, i.e. $\frac{\partial \overline{\rho}\widetilde{u}_i}{\partial x_i}$. A $2D$ representation is shown in Figure 2.2.

The goal is to use the $3D$ LES mass flux information to perform the transport of species between adjacent LES domains. This is done by splicing the species field successively in the three different directions following a set of established rules.

- Rule 1: In a given direction, splicing is done at once.
- Rule 2: Splicing is performed using an upwind-like scheme.
- Rule 2: The absolute value and the sign of $\frac{\partial \overline{\rho}\widetilde{u}_i}{\partial x_i}$ determine the order in which splicing is performed.

Still using the 2D approach of Figure 2.2, we assume that:

$$\frac{\partial \overline{\rho}\widetilde{u}}{\partial x}\Big|_{(i-\frac{1}{2})} < \frac{\partial \overline{\rho}\widetilde{u}}{\partial x}\Big|_{(i+\frac{1}{2})} < 0 < \frac{\partial \overline{\rho}\widetilde{v}}{\partial y}\Big|_{(j-\frac{1}{2})} < \frac{\partial \overline{\rho}\widetilde{v}}{\partial y}\Big|_{(j+\frac{1}{2})} \tag{2.71}$$

For clarity, we designate these fluxes as:

$$\begin{aligned}
\frac{1}{\delta t_{LES}}\frac{\delta m_1}{V^{LES}} &= F_i^0 = \frac{\partial \overline{\rho}\widetilde{u}}{\partial x}\Big|_{(i-\frac{1}{2})} \\
\frac{1}{\delta t_{LES}}\frac{\delta m_2}{V^{LES}} &= F_i^1 = \frac{\partial \overline{\rho}\widetilde{u}}{\partial x}\Big|_{(i+\frac{1}{2})} \\
\frac{1}{\delta t_{LES}}\frac{\delta m_3}{V^{LES}} &= F_j^0 = \frac{\partial \overline{\rho}\widetilde{u}}{\partial y}\Big|_{(j-\frac{1}{2})} \\
\frac{1}{\delta t_{LES}}\frac{\delta m_4}{V^{LES}} &= F_j^1 = \frac{\partial \overline{\rho}\widetilde{u}}{\partial y}\Big|_{(j+\frac{1}{2})}
\end{aligned} \tag{2.72}$$

All species that are in the LEM domain exit the domain via the cell number N^{LEM} and enter via the cell number 1. The largest negative flux (i.e. mass exits the LES cell) is the first one to be transported through its respective surface. In the same idea, the largest positive flux (i.e. mass enters the LES cell) is the last one to enter the LES cell.

Splicing being done by considering the mass of the system, the following relationship can be written:

$$F_j^1 V^{LES} = \sum_{l=0}^{L} \rho_l^{LEM} V^{LEM} + R_m \tag{2.73}$$

where V^{LEM} is the volume of an LEM cell, L is the maximum number of cells than can be transfered to another LEM domain and R_m is the residual ($0<R_m<\rho_{L+1}^{LEM} V^{LEM}$). Figures. 2.3 (before splicing) and 2.4 (after splicing) are schematic representations of the splicing process. Splicing is done at both the predictor and corrector step of the *McCormack*-scheme.

2.2.3.1 Molecular Diffusion and Chemical Reaction

Species molecular diffusion, heat diffusion and heat diffusion via molecular diffusion is performed on the LEM domain following Eq. 2.68. The chemical mechanisms are described in section 3.6.

A large range of time scales is involved in diffusion-reaction processes. The idea is to simulate all relevant subgrid processes at their respective time scale. The time scale

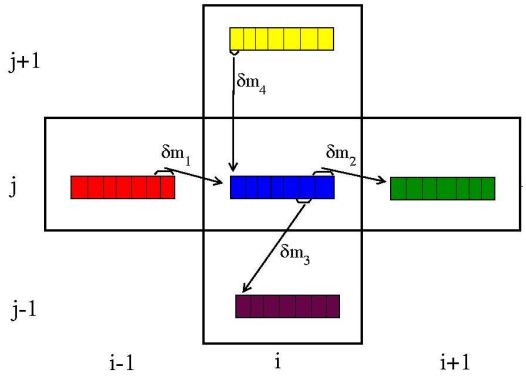

Figure 2.3: *LEM* species field before the splicing of the cell (i,j).

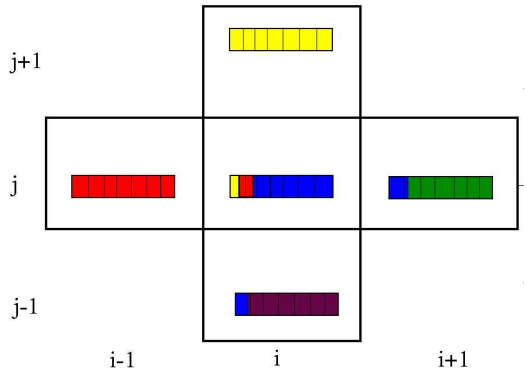

Figure 2.4: *LEM* species field after the splicing of the cell (i,j).

related to the chemical reaction (Δt_{chem}) is related to the stiffness of the set of equations describing the species reaction rates. The time scale related to the molecular diffusion (Δt_{diff}) corresponds to the stability limit of the diffusion equation. The diffusion time step is defined as follow:

$$\Delta t_{diff} = C_d \frac{\left(\Delta s\right)^2}{max_{k=1,N}(D_k)} \tag{2.74}$$

where Δs is the LEM grid spacing and C_d=0.25 for numerical stability purposes.

Turbulent combustion processes are taken into account. The time scale of these processes (Δt_{stir}) is defined in sec. 2.2.3.2 The scheme of the LES solver being explicit, it is natural to solve all the subgrid processes in an explicit manner. This is possible through the use of an operator splitting method Smith and Menon [1996b], Calhoon and Menon [1996]. More details on this technique are given in section 2.2.3.3.

Volumetric gas expansion is simulated. Contrary to the LES finite volume approach, the LEM cells are able to expand and contract, i.e. to change volume, depending upon the amount of heat release when chemical reaction occurs. If the index 0 defines the state of the LEM variables before volumetric expansion and the index 1 defines the state of the LEM variable after this expansion, the following relation can be derived:

$$\frac{V_1^{LEM}}{V_0^{LEM}} = \frac{T_1^{LEM}}{T_0^{LEM}} \tag{2.75}$$

After volumetric expansion, the cells of the LEM domain are not of equal volume and the LEM domain has to be re-gridded. Contrary to previous studies (Smith and Menon [1998], Chakravarthy and Menon [2000]), the LEM cells are re-gridded after the splicing. Re-griding of the scalar field acts as a numerical diffusion and is discussed in section 5.2.5.

2.2.3.2 Subgrid Turbulence

Subgrid convection (also called turbulent stirring) due to subgrid turbulence is simulated at the LEM level and is represented by the terms F_k^{stir} and F_T^{stir} (see Eq. 2.68).

The subgrid stirring is modeled by rearranging the species field on the LEM domain such that this rearrangement mimics the action of half a turnover of a subgrid eddy on the LEM scalar field. The rearrangement technique used here is the *triplet mapping* defined

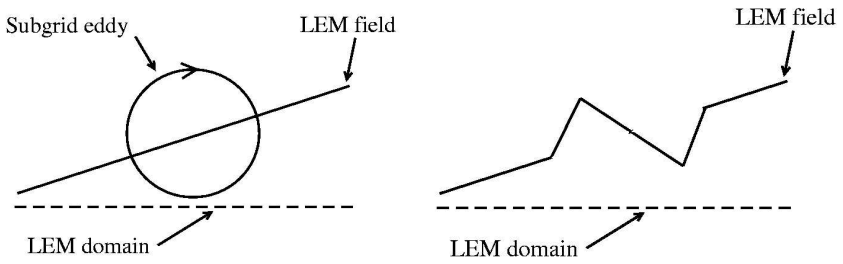

(a) Before the rearrangement is performed. The rearrangement mimics the action of the subgrid eddy shown on the figure.

(b) After the rearrangement is performed.

Figure 2.5: Schematic representation of the action of a subgrid eddy on a *LEM* scalar field.

by Kerstein [1989]. Kerstein demonstrated that this technique captures accurately the increase in scalar gradient without affecting the mean scalar field (i.e., *triplet mapping* is mass conservative). This rearrangement is performed on the $1D$ *LEM* line, hence explicitly assuming that the subgrid turbulence is isotropic. A schematic of this rearrangement is shown in Figure 2.5.

Mathematically, the triplet mapping can be defined as a function transforming the initial scalar field $\Psi^0(x,t)$ into a *stirred* scalar field $\Psi(x,t)$:

$$\Psi^0(x,t) = \begin{cases} \Psi^0(3x-2x_0,t) & x_0 \leq x \leq x_0 + l/3 \\ \Psi^0(3x-2x_0,t) & x_0 + l/3 \leq x \leq x_0 + 2l/3 \\ \Psi^0(3x-2x_0,t) & x_0 + 2l/3 \leq x \leq x_0 + l \\ \Psi^0(3x-2x_0,t) & otherwise \end{cases} \tag{2.76}$$

The function inputs are the eddy size l and the location of the stirring event. The location of the stirring event is chosen from a uniform distribution, the frequency of stirring per unit length (λ) is derived from 3D scaling laws Kerstein [1989] as:

$$\lambda = \frac{54}{5} \frac{\nu Re_{\overline{\Delta}}}{C_\lambda \overline{\Delta}^3} \frac{[(\overline{\Delta}/\eta)^{5/3} - 1]}{[1 - (\eta/\overline{\Delta})^{4/3}]} \tag{2.77}$$

C_λ represents the scalar turbulent diffusivity and is determined to be 0.067 Smith and

Menon [1996a]. The time interval between stirring events is defined as:

$$\Delta t_{stir} = \frac{1}{\lambda \overline{\Delta}} \tag{2.78}$$

The eddy size (l) is chosen from the following PDF:

$$f(l) = \frac{(5/3) l^{-8/3}}{\eta^{-5/3} - \overline{\Delta}^{-5/3}} \tag{2.79}$$

where:

$$\eta = N_\eta \overline{\Delta} Re_{\overline{\Delta}}^{-4/3} \tag{2.80}$$

The empirical constant N_η reduces the effective range of scale between the integral length scales and η but does not change the turbulent diffusivity ($N_\eta \in [1.3;10.78]$) Smith and Menon [1996a].

Note that the two empirical coefficients (N_η and C_λ) are present because *scaling* laws are used. In the study of Smith and Menon [1996a], N_η and C_λ are determined by comparing LEM turbulent flame speed to the turbulent flame speed model of Pocheau [1992]. Following the argument that the momentum diffusivity in the inertial range must be equal to the scalar diffusivity in the inertial range (the same turbulent structures are responsible for both phenomena), Chakravarthy and Menon [2000] concluded that the turbulent eddy viscosity C_λ must be equal to C_ν.

2.2.3.3 Splitting Operator

This techniques allows for decoupled time resolution of the chemical, diffusion and turbulent processes. This allows to consider the time scales attached to each processes as the integration time step of the respective process. In other words, stirring is performed at Δt_{stir}, diffusion at Δt_{diff} and chemical reaction at Δt_{reac} is assumed to be equal to Δt_{diff}.

The implementation of the time splitting operator is presented in this paragraph.

- ***Step*1**: Δt_{diff} is compared to Δt_{LES}. N_{diff}=max($\Delta t_{LES}/\Delta t_{diff}$,1).
- ***Step*2**: Δt_{stir} is compared to Δt_{LES}. N_{stir}=max($\Delta t_{LES}/\Delta t_{stir}$,1).
- ***Step*3**: N_{iter} is defined as the maximum of N_{diff} and N_{stir}.

- ***Step4***: Reaction, diffusion and stirring are performed N_{iter}-th time. Stirring is only performed when $n^*N_{diff} < \Delta t_{stir} < (n+1)^*N_{diff}$ where n is the iteration index $n \in [1; N_{iter}]$.

- ***Step5***: Due to thermal expansion, the LEM domain is re-gridded such that all LEM cells have the same volume.

2.3 Flamelet Modeling and Flamelet Library

As described in section 1.2, a turbulent flame can be, under certain conditions, considered as being formed by a succession of laminar flame elements. This assumption is of great use to compute flame properties like S_L, product temperature, etc. The idea behind the flamelet library is to use the CHEMKIN-PREMIX package Kee et al. [1992] to compute the various flame properties. These properties are a function of the the mixture fraction Z.

2.3.1 Mixture Fraction Governing Equation

The mixture fraction is defined as the ratio of mass of material having its origin in the fuel stream over the mass of mixture. Consider a three species (fuel, oxidizer and product) system. We have the following chemical mechanism:

$$\underbrace{Fuel}_{1kg} + \underbrace{Oxidizer}_{\nu kg} \leftrightarrow \underbrace{Products}_{(1+\nu)kg} \tag{2.81}$$

Using the above definition of Z:

$$Z = \underbrace{1}_{\frac{\text{kg of fuel stuff}}{\text{kg of fuel}}} \underbrace{Y_F}_{\frac{\text{kg of fuel}}{\text{kg of mixture}}} + \underbrace{\frac{1}{1+\nu}}_{\frac{\text{kg of fuel stuff}}{\text{kg of products}}} \underbrace{Y_{Pr}}_{\frac{\text{kg of products}}{\text{kg of mixture}}} + \underbrace{0}_{\frac{\text{kg of fuel stuff}}{\text{kg of oxidizer}}} \underbrace{Y_{Ox}}_{\frac{\text{kg of oxidizer}}{\text{kg of mixture}}} \tag{2.82}$$

The above equation can be written as:

$$Z = Y_F + \Big(\frac{1}{1+\nu}\Big) Y_{Pr} \tag{2.83}$$

This approach is usually used for diffusion flames but can also be employed for numerical simulation of premixed flame propagation. This approach implicitly assumes that the molecular diffusion coefficients of all species are the same. This is a limitation of the model

and is assumed to have no influence on the results that are presented in the rest of this work.

The mixture fraction is a conservative scalar, therefore, no source term is present in the governing equation of Z (except if, for example, droplet evaporation is considered). The governing equation of Z is:

$$\frac{\partial(\rho Z)}{\partial t} + \frac{\partial}{\partial x_i}\Big(\rho u_i Z\Big) = -\frac{\partial}{\partial x_i}\Big(D\rho\frac{\partial Z}{\partial x_i}\Big) \tag{2.84}$$

The LES filtered governing equation is:

$$\frac{\partial(\overline{\rho}\widetilde{Z})}{\partial t} + \frac{\partial}{\partial x_i}\Big(\overline{\rho}\widetilde{u_i}\widetilde{Z}\Big) = -\frac{\partial}{\partial x_i}\Big(D\overline{\rho}\frac{\partial\widetilde{Z}}{\partial x_i}\Big) - \frac{\partial}{\partial x_i}\Big(\overline{\rho}(\widetilde{u_i Z} - \widetilde{u_i}\widetilde{Z})\Big) \tag{2.85}$$

The LES averaged governing equation is closed using a turbulent gradient assumption closure:

$$\overline{\rho}(\widetilde{u_i Z} - \widetilde{u_i}\widetilde{Z}) = -\overline{\rho}D_T\frac{\partial\widetilde{Z}}{\partial x_i} \tag{2.86}$$

where D_T=ν_T/Le. Thus:

$$\frac{\partial(\overline{\rho}\widetilde{Z})}{\partial t} + \frac{\partial}{\partial x_i}\Big(\overline{\rho}\widetilde{u_i}\widetilde{Z}\Big) = \frac{\partial}{\partial x_i}\Big((D + D_T)\overline{\rho}\frac{\partial\widetilde{Z}}{\partial x_i}\Big) \tag{2.87}$$

The information about the LES filtered value of the mixture fraction is not sufficient. The level of "unmixedness" of the premixed mixture in a given LES cell is needed and is measured using the variance of the mixture fraction $\widetilde{Z''^2}$. The LES filtered governing equation for $\widetilde{Z''^2}$ is Peters [2000]:

$$\frac{\partial\overline{\rho}\widetilde{Z''^2}}{\partial t} + \frac{\partial}{\partial x_i}\Big(\rho\widetilde{u_i}\widetilde{Z''^2}\Big) = \frac{\partial}{\partial x_i}\Big(D_T\overline{\rho}\frac{\partial Z''^2}{\partial x_i} + 2\overline{\rho}D_T\sum_{i=1}^{3}\frac{\partial\widetilde{Z''^2}}{\partial x_i} - \overline{\rho}\widetilde{\chi}\tag{2.88}$$

To determine the mean scalar dissipation $\widetilde{\chi}$, the following model is used Peters [2000]:

$$\widetilde{\chi} = 2D|\nabla Z''^2| \tag{2.89}$$

and $\widetilde{\chi}$ is computed as:

$$\widetilde{\chi} = 2D\frac{\epsilon}{k^{sgs}}\widetilde{Z''^2} \tag{2.90}$$

With the above closure, any resolved chemical parameter $\widetilde{\Psi}$ is determined using an assumed probability density function (PDF) f (beta PDF), that is a function of $\widetilde{Z}$ and $\widetilde{Z''^2}$:

$$\widetilde{\Psi}(\widetilde{Z}) = \int_0^\infty \Psi(\widetilde{Z})f(\widetilde{Z},\widetilde{Z''^2})dZ''^2 \tag{2.91}$$

For perfectly premixed combustion, $\widetilde{Z}$ is constant and $\widetilde{Z''^2}$ is equal to zero, hence, the above method is considerably simplified. However, some simulations assuming partially premixed state at the inflow were also conducted, as discussed in section 4.3. The mixture fraction approach is valid only if the molecular diffusion coefficients of all species are equal. This is implicit in the $GLES$ approach. In $LEMLES$, the 1-step chemistry uses different diffusion coefficients but this is assumed to have no significant effect on final pollutant emission prediction.

2.3.2 Flamelet Library Generation and Usage

The flamelet library is a database of all information relevant to the study and simulation of the flame propagation, product temperature, pollutants formation and consumption, etc. The information used in this study are:

- Flame laminar speed S_L
- Product temperature T_P
- Mass fraction of CO formed at the flame front, $Y_{CO,ff}$
- Equilibrium mass fraction of CO in the post-flame, $Y_{CO,eq}$
- Rate of oxidation of CO in the post-flame region, $\tau_{CO,ox}$
- Mass fraction of NO formed at the flame front, $Y_{NO,ff}$
- Rate of formation of NO in the post-flame region, $\tau_{NO,pf}$

The method used to generate the flamelet library is now described. As stated previously, outputs from the CHEMKIN-PREMIX package are used to generate the flamelet library. For example, multiple outputs are generated for equivalence ratios ranging from Φ_A and Φ_B. S_L and T_P are easily interpolated for all equivalence ratio ranging between Φ_A and Φ_B.

The amount of CO formed at the flame front as well as the rate of oxidation of CO are determined by analyzing the species mass fraction profile along the flame. A typical CO

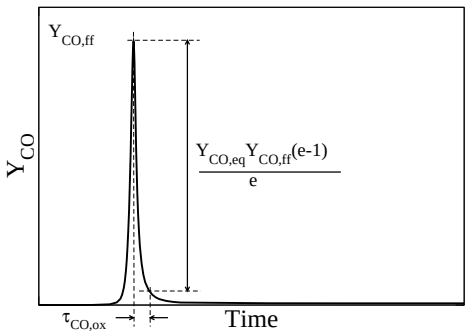

Figure 2.6: Laminar profile of the CO mass fraction obtained from CHEMKIN output.

profile is shown in Figure 2.6. The amount of CO formed at the flame front is taken as the maximum amount of CO formed ($Y_{CO,ff}$). The equilibrium mass fraction of CO in the post-flame is also trivial to determine. Because the oxidation of CO follows an exponential decrease, the oxidation rate of CO is computed as the time taken by Y_{CO} mass fraction to go from $Y_{CO,ff}$ to $\frac{Y_{CO,eq}+Y_{CO,ff}(e-1)}{e}$ where e=$exp(1)$. Thus:

$$Y_{CO}(t) = Y_{CO,eq} + \big(Y_{CO,ff} - Y_{CO,eq}\big) exp(-\frac{t-t_0}{\tau_{CO,ox}}) \tag{2.92}$$

where t_0 corresponds to the time where $Y_{CO} = Y_{CO,ff}$. Eq. 2.92 is valid for t>t_0, i.e. on the product side. One the reactant side (t<t_0), $Y_{CO} = 0$.

The NO profile is shown of Figure 2.7. Two different regions are noticeable. The first one corresponds to the formation of NO at the flame front (t<t_1) and the second linear part of the curve corresponds to the formation of NO in the post-flame region via the Zeldovitch mechanism. In this case, the following general relation can be derived:

$$Y_{NO}(t) = Y_{NO,ff} + \tau_{NO,pf}(t - t_1) \tag{2.93}$$

Again, Eq. 2.93 is valid for t>t_1, i.e. on the product side. One the reactant side (t<t_1), $Y_{NO} = 0$.

2.4 Pollutant Modeling

In the present study, we employ $GLES$ and $LEMLES$ to primarily predict the global heat release and the flame characteristics. To properly capture pollutant emission, a multi-species, detailed reaction mechanism is needed since emission occurs both in the flame zone

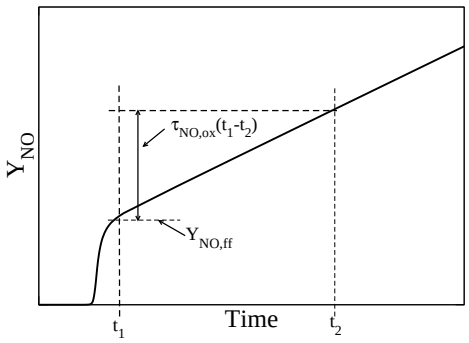

Figure 2.7: Laminar profile of the NO mass fraction obtained from CHEMKIN output.

and in the post-flame zone. However, detailed reaction kinetics modeling is not consistent with the $GLES$ approach, and can be considerably expensive in the $LEMLES$. Therefore a model approach is used to track pollutants (CO, NO and UHC) at the LES level in both $GLES$ and $LEMLES$ approaches. For the $LEMLES$ approach, only a computationally expensive chemical mechanism will include both CO and NO. In the study of pollutant emission, a basic 1-step reduced chemical mechanism is used and, even in the $LEMLES$ case, the CO and NO governing equations are resolved at the LES level. The pollutants source and sink terms are discussed in the next sections.

2.4.1 Carbon Monoxide

CO is formed and/or destroyed by three major mechanisms: (i) the formation of CO at the flame front, (ii) the oxidation of CO in the post-flame region and the dissociation of CO_2 and (iii) the formation of CO via oxidation of unburned CH_4.

A large amount of CO is produced at the flame front ($Y_{CO,ff}$). The rate of formation of CO at the flame front $\widetilde{\dot{w}_{CO,ff}}$ is proportional to the rate of fuel consumption $\dot{w}_{fuel}$ Held et al. [2001], Held and Mongia [1998], and is modeled as:

$$\widetilde{\dot{w}_{CO,ff}} = -\frac{\dot{w}_{fuel}}{C_{ref}} Y_{CO,ff} \tag{2.94}$$

Here, $\dot{w}_{fuel} = -S_T|\nabla \widetilde{G}|$ and $C_{ref} = 1$ in the $GLES$ approach. In the $LEMLES$ approach, $\dot{w}_{fuel}$ is taken as the arithmetic average of the fuel consumption rate of all the LEM cells contained inside an LES cell and C_{ref} is equal to the local filtered value of the mixture fraction. Flame curvature effects are not taken into account.

Once CO is formed it will be oxidized into CO_2. From the flamelet library the rate of oxidation is given by $\dot{w}_{CO,ox} = -\frac{1}{\tau_{CO,ox}}\widetilde{Y_{CO}}$. The oxidation time scale is based upon the product temperature at a given equivalence ratio. To account for the change in temperature due to heat losses, if present, the CO oxidation time scale is corrected, as follow:

$$\frac{1}{\tau_{CO,ox}} = \frac{1}{\tau_{CO,ox}} exp\Big(E_A \frac{\widetilde{T} - T_b}{\widetilde{T} T_b}\Big) \tag{2.95}$$

Here, $\widetilde{T}$ is the actual LES temperature, T_b is the adiabatic flame temperature predicted by the flamelet library, and E_A is the activation energy chosen by curve fitting the flamelet library data. Note that, the reaction rate of CO oxidation in the post-flame region in the current closure is independent of the subgrid turbulence since CHEMKIN does not take into account the influence of turbulence. Also the influence of flame curvature is neglected.

CO reaches its equilibrium value when the consumption rate equals the production rate via CO_2 dissociation. The rate of formation of CO via CO_2 dissociation is taken as:

$$\widetilde{\dot{w}}_{CO,eq} = P_b \frac{\dot{w}_{fuel}}{C_{ref}} Y_{CO,ff} \tag{2.96}$$

where $P_b = 0$ on the reactant side and $P_b = 1$ on the product side. When $\widetilde{Y_{CO}} = Y_{CO,eq}$, then $\widetilde{\dot{w}}_{CO,ox} + \widetilde{\dot{w}}_{CO,eq} = 0$. The last mechanism of CO formation via oxidation of unburned hydrocarbon (UHC) is treated explicitly, as described in sec. 2.4.2.

2.4.2 Unburnt Hydrocarbons (UHC)

Intense turbulence combined with heat loss has the capacity to quench a premixed flame Meneveau and Poinsot [1991]. If the flame front is partially quenched, pockets of unburnt methane (UHC) are released into the post-flame region and are oxidized at a rate governed by an Arrhenius-law. The UHC oxidation into CO is computed as:

$$\frac{d[UHC]}{dt} = -[UHC][O_2] A exp\Big(-\frac{E_A}{R_U \widetilde{T}}\Big) \tag{2.97}$$

Therefore, in terms of mass fraction:

$$\frac{d}{dt}\Big(\frac{Y_{UHC}}{MW_{CH_4}}\Big) = -\Big[\frac{\overline{p}}{R_U \widetilde{T}}\Big]\Big(\frac{\widetilde{Y_{UHC}}}{MW_{CH_4}}\Big)\Big(\frac{\widetilde{Y_{O_2}}}{MW_{O_2}}\Big) A exp\Big(-\frac{E_A}{R_U \widetilde{T}}\Big) \tag{2.98}$$

In order to predict the appropriate amount of UHC released into the post-flame zone, it is necessary to model local flame quenching. Currently, no robust method exists to include

this effect in an unsteady simulation, other than including detailed kinetics in $LEMLES$ or using the unsteady flamelet approach Pitsch and Duchamp De Lageneste [2002] (Note that, for both methods, the ability to predict flame quenching still has to be demonstrated). Here, a model developed for steady-state application, called the Intermittent Turbulence Net Flame Stretch Model (ITNFS Meneveau and Poinsot [1991]) is employed.

The entire amount of UHC oxidized is assumed to be converted into CO, therefore:

$$\widetilde{\dot{w}}_{CO,oxuhc} = -\frac{MW_{CO}}{MW_{CH_4}}\widetilde{\dot{w}}_{UHC} \tag{2.99}$$

2.4.3 Oxides of Nitrogen (NO_x)

Two mechanisms related to NO_x formation are taken into account in the present work. The first mechanism is the production of NO_x at the flame front (prompt NO_x) and the second one is the production of nitric monoxide in the post-flame region (thermal NO_x). These mechanisms are described in details elsewhere Hill and Douglas Smoot [2000]. Prompt NO_x is formed at the flame front ($Y_{NO,ff}$, value computed by the flamelet library) and its rate of formation ($\widetilde{\dot{w_{NO,ox}}}$) at the flame front is computed as follow:

$$\widetilde{\dot{w_{NO,ff}}} = -\frac{\overline{\dot{w_{fuel}}}}{C_{ref}}Y_{NO,ox} \tag{2.100}$$

The rate of formation of thermal NO_x ($\widetilde{\dot{w_{NO,ox}}}$) is given by the following relationship:

$$\widetilde{\dot{w_{NO,pf}}} = \frac{1}{\tau_{NO,pf}} \tag{2.101}$$

CHAPTER III

NUMERICAL IMPLEMENTATION

In the preceding chapter, the LES governing equations were presented. Here, the numerical implementation used to solve the set of Navier-Stokes equations is described. In this study, a finite volume scheme is used. This scheme is second order in time and can be second or fourth order in space. A finite volume approach has two major advantages when compared to a finite difference scheme: finite volume approach can handle skewed grids and solve the discretized governing equations in a conservative form, i.e. strict conservation of mass, momentum and energy is enforced.

This chapter also describes the different geometries that are simulated in this work. Two geometries are used. The one denoted $DOE - HAT$ (Department of Energy - Humid Air Turbine) is the same as a previous experimental work Bhargava et al. [2000] and was primary used to asses the validity of the pollutant emission models. The second geometry is a a dump combustor used to study flame structure and flame extinction in lean systems.

3.1 Finite Volume Scheme

The governing equations can be written in conservative vector form:

$$\frac{\partial \vec{Q}}{\partial t} + \nabla \cdot \vec{F} = \vec{S} \tag{3.1}$$

The state vector $\vec{Q}$ represents the conserved variables (mass, momentum, energy and species) while $\vec{F}$ represents the flux of $\vec{Q}$ through the cell control surface A. $\vec{S}$ represents the different source terms. This equation is integrated over the control volume V:

$$\int_V \frac{\partial \vec{Q}}{\partial t} dV + \int_V \Delta \cdot \vec{F} dV = \int_V \vec{S} dV \tag{3.2}$$

By permuting $\int_V$ and $\frac{\partial}{\partial t}$ and using Gauss' theorem, the following equation is obtained:

$$\frac{\partial}{\partial t} \int_V \vec{Q} dV + \oint_A \vec{F} \cdot d\vec{A} = \int_V \vec{S} dV \tag{3.3}$$

where A is the closed area surrounding the control volume V. $\vec{Q}$, $\vec{F}$ and $\vec{S}$ are uniform inside the control volume, i.e. their values are averaged over V. In this study, a structured grid approach is used. The control volume V has six faces (computations are three-dimensional). The area of the six faces of the control volume are denoted dA_i, i=1,6. The vector normal to the surface i is denoted as $d\vec{A}_i$ and its amplitude is dA_i. Therefore, one can rewritten Eq. 3.3:

$$\vec{Q} + \frac{1}{V}\sum_{i=1}^{6} \vec{F} \cdot \vec{A}_i = \vec{S} \tag{3.4}$$

Using Eq. 2.14, we can define $\vec{Q}$, $\vec{F}$ and $\vec{S}$.

$$\vec{Q} = \begin{pmatrix} \overline{\rho} \\ \overline{\rho}\widetilde{u} \\ \overline{\rho}\widetilde{v} \\ \overline{\rho}\widetilde{w} \\ \overline{\rho}\widetilde{E} \\ \overline{\rho}k^{sgs} \\ \overline{\rho}\widetilde{Y_i} \end{pmatrix}$$

$$\vec{S} = \begin{pmatrix} 0 \\ 0 \\ 0 \\ 0 \\ 0 \\ P^{sgs} - D^{sgs} \\ \widetilde{\dot{w}} \end{pmatrix}$$

The flux vector has three components (one for each spatial direction):

$$\vec{F} = \vec{F_x} + \vec{F_y} + \vec{F_z} \tag{3.5}$$

Finally:

$$\vec{F}_x = \begin{pmatrix} \overline{\rho}\widetilde{u} \\ \overline{\rho}\widetilde{u}\widetilde{u} + \overline{p} \\ \overline{\rho}\widetilde{u}\widetilde{v} \\ \overline{\rho}\widetilde{u}\widetilde{w} \\ \overline{\rho}\widetilde{u}\big(\widetilde{E} + \overline{p}\big) \\ \overline{\rho}\widetilde{u}k^{sgs} \\ \overline{\rho}\widetilde{u}\widetilde{Y}_i \end{pmatrix} - \begin{pmatrix} 0 \\ \overline{\tau}_{xx} \\ \overline{\tau}_{xy} \\ \overline{\tau}_{xz} \\ \overline{\sigma_x} - \overline{q_x} \\ 0 \\ \overline{\rho}D_i\frac{\partial\widetilde{Y}_i}{\partial x} \end{pmatrix} + \begin{pmatrix} 0 \\ \tau_{xx}^{sgs} \\ \tau_{xy}^{sgs} \\ \tau_{xz}^{sgs} \\ \frac{\overline{\rho}\nu_t}{Pr_t}\frac{\widetilde{H}}{\partial x} \\ \frac{\overline{\rho}\left(\nu+\nu_t\right)}{Pr_t}\frac{\widetilde{k^{sgs}}}{\partial x} \\ \overline{\rho}D_t\frac{\partial\widetilde{Y}_i}{\partial x} \end{pmatrix}$$

$$\vec{F}_y = \begin{pmatrix} \overline{\rho}\widetilde{v} \\ \overline{\rho}\widetilde{v}\widetilde{u} \\ \overline{\rho}\widetilde{v}\widetilde{v} + \overline{p} \\ \overline{\rho}\widetilde{v}\widetilde{w} \\ \overline{\rho}\widetilde{v}\big(\widetilde{E} + \overline{p}\big) \\ \overline{\rho}\widetilde{v}k^{sgs} \\ \overline{\rho}\widetilde{v}\widetilde{Y}_i \end{pmatrix} - \begin{pmatrix} 0 \\ \overline{\tau}_{yx} \\ \overline{\tau}_{yy} \\ \overline{\tau}_{yz} \\ \overline{\sigma_y} - \overline{q_y} \\ 0 \\ \overline{\rho}D_i\frac{\partial\widetilde{Y}_i}{\partial y} \end{pmatrix} + \begin{pmatrix} 0 \\ \tau_{yx}^{sgs} \\ \tau_{yy}^{sgs} \\ \tau_{yz}^{sgs} \\ \frac{\overline{\rho}\nu_t}{Pr_t}\frac{\widetilde{H}}{\partial y} \\ \frac{\overline{\rho}\left(\nu+\nu_t\right)}{Pr_t}\frac{\widetilde{k^{sgs}}}{\partial y} \\ \overline{\rho}D_t\frac{\partial\widetilde{Y}_i}{\partial y} \end{pmatrix}$$

$$\vec{F}_z = \underbrace{\begin{pmatrix} \overline{\rho}\widetilde{w} \\ \overline{\rho}\widetilde{w}\widetilde{u} \\ \overline{\rho}\widetilde{w}\widetilde{v} \\ \overline{\rho}\widetilde{w}\widetilde{w} + \overline{p} \\ \overline{\rho}\widetilde{w}\big(\widetilde{E} + \overline{p}\big) \\ \overline{\rho}\widetilde{w}k^{sgs} \\ \overline{\rho}\widetilde{w}\widetilde{Y}_i \end{pmatrix}}_{F^E} - \underbrace{\begin{pmatrix} 0 \\ \overline{\tau}_{zx} \\ \overline{\tau}_{zy} \\ \overline{\tau}_{zz} \\ \overline{\sigma_z} - \overline{q_z} \\ 0 \\ \overline{\rho}D_i\frac{\partial\widetilde{Y}_i}{\partial z} \end{pmatrix}}_{F^V} + \underbrace{\begin{pmatrix} 0 \\ \tau_{zx}^{sgs} \\ \tau_{zy}^{sgs} \\ \tau_{zz}^{sgs} \\ \frac{\overline{\rho}\nu_t}{Pr_t}\frac{\widetilde{H}}{\partial z} \\ \frac{\overline{\rho}\left(\nu+\nu_t\right)}{Pr_t}\frac{\widetilde{k^{sgs}}}{\partial z} \\ \overline{\rho}D_t\frac{\partial\widetilde{Y}_i}{\partial z} \end{pmatrix}}_{F^{sgs}}$$

where F^E, F^V and F^{sgs} are the Eulerian Fluxes, viscous fluxes and subgrid fluxes, respectively.

The method used to compute the mass, momentum, energy and species fluxes is discussed in sec. 3.3.2.

3.2 Time Integration

A time integration method is needed to integrate Eq. 3.1 with regard to time. There are two categories of time integration schemes: *implicit* and *explicit* schemes. In sec. 3.2.1, the two schemes are discussed. In sec. 3.2.2, the explicit scheme used in this work is discussed.

3.2.1 Explicit and Implicit Time Integration Scheme

Two categories of time integration scheme are available. They are known as *explicit* schemes or *implicit* schemes. *Explicit* schemes uses information at a given time t to compute the new value of the different variables at time $t + \Delta t$. Implementation of such schemes is straightforward.

On the other hand, *implicit* schemes use information at time $t+\Delta t$ to compute the value of the different variables at time $t + \Delta t$. The latter is made possible via the resolution of large system of equations. This requires numerous matrix inversion and can be challenging to implement.

Every time integration scheme has a characteristic integration time step Δt. Δt is determined as a function of the numerical stability of the scheme. *Implicit* schemes are usually more stable than *explicit* schemes, therefore, Δt is larger for *implicit* schemes. As a consequence, a computation spanning over a finite time t_0 requires less computation steps if an *implicit* scheme is used. However, the total computational cost of such a scheme is larger than the computational cost of an *explicit* scheme.

Furthermore, in the case of the simulation of reacting flows, the integration time step can be limited by time scales related to combustion processes. In this case, it is not desirable to have a large Δt and the use of an *explicit* time integration scheme is justified. Therefore, for this work, the *explicit MacCormack* time-integration scheme is used MacCormack [1969].

3.2.2 MacCormack Time Integration Scheme

The *MacCormack* method integrates Eq. 3.1 with regard to time in a two steps manner. These two steps are known as the *predictor* step and the *corrector* step. The combination of the two steps leads to a scheme with a global second order accuracy in time (i.e. the

error in the time integration is of the order of $(\Delta t)^2$, where Δt is the actual integration time). The computation of Δt is discussed in section 3.2.3. The time integration of Eq. 3.1 can be written as:

$$\begin{aligned} \text{Predictor} \quad \vec{Q}^{*} &= \vec{Q}^{n} + d\vec{Q}^{n}\Delta t \\ \text{Corrector} \quad \vec{Q}^{n+1} &= \tfrac{1}{2}\Big[\vec{Q}^{n} + \vec{Q}^{*} + d\vec{Q}^{*}\Delta t\Big] \end{aligned} \tag{3.6}$$

Here, $\vec{Q}^{n}$ represents the state of the conserved variables at a time t. The variation $d\vec{Q}$ of the conserved variable $\vec{Q}$ is a function of both the fluxes $\vec{F}$ and the source term $\vec{S}$. The variation of $d\vec{Q}$ is computed as:

$$\begin{aligned} d\vec{Q}^{n} &= -\Delta t\Big[\frac{1}{V}\sum_{i=1}^{6}\Big(\vec{F}_i^{+^n}\cdot d\vec{A}_i\Big) - \vec{S}^{n}\Big] \\ d\vec{Q}^{*} &= -\Delta t\Big[\frac{1}{V}\sum_{i=1}^{6}\Big(\vec{F}_i^{-^*}\cdot d\vec{A}_i\Big) - \vec{S}^{*}\Big] \end{aligned} \tag{3.7}$$

The quantities denoted with the superscript $(*)$ represents the intermediate quantities computed by the *predictor* step. Both *predictor* and *corrector* steps use Δt as the integration time and the factor 1/2 in Eq. 3.6 ensures that $\vec{Q}^{n+1}$ represents the state of the conserved variables at $t+\Delta t$. $\vec{F}_i^{+^n}$ and $\vec{F}_i^{-^n}$ represent the fluxes at the surface i which are evaluated using a forward and backward difference method, respectively. Alternating between forward (+) and backward (-) difference method in a two steps time integration scheme is equivalent to a central scheme. In order to avoid any bias caused by the forward and backward difference methods, the computation of the fluxes are alternated as a function of the direction and the time step. If n is the time step, i,j and k are the three spatial directions and $+$ and $-$ represents forward and backward difference respectively, the rule for alternating $+$ and $-$ is shown on Table 3.1. The accuracy of the spatial discretization depends upon the accuracy in the computation of the fluxes. More details are given in section 3.3.2.

Table 3.1: Forward and backward computation of the fluxes as a function of the time step and the direction.

Time Step	Direction I Predictor / Corrector	Direction J Predictor / Corrector	Direction K Predictor / Corrector
n	+/-	+/-	+/-
n+1	-/+	+/-	+/-
n+2	+/-	-/+	+/-
n+3	-/+	-/+	+/-
n+4	+/-	+/-	-/+
n+5	-/+	+/-	-/+
n+6	+/-	-/+	-/+
n+7	-/+	-/+	-/+

3.2.3 Computation of Δt

As stated above, the integration time step is chosen as the time step which ensures a numerically stable computation. Stability theory stipulates that a given $information$ can not travel more than a certain portion of the grid spacing. The velocity of this $information$ (v_p) can be compared to its wave speed. The grid spacing is a direct function of the grid volume V and the norm of the cell area vector ($\mid d\vec{A} \mid$). The portion of the grid that the $information$ can travel is known as the CFL number, named after $Courant - Friedric - Levy$. The grid spacing is evaluated as $V/|d\vec{A}|$, therefore:

$$\Delta t = CFL * \frac{V}{|d\vec{A}| \cdot v_p} \tag{3.8}$$

When using the $MacCormack$ method, a single time step must be used for the entire computational domain. If MIN_D represents the minimum value over the entire computational domain, the computational time step is defined as:

$$\Delta t = CFL * MIN_D\Big(\frac{V}{|d\vec{A}| \cdot v_p}\Big) \tag{3.9}$$

Note that no analytical stability condition was derived for the Navier-Stokes equations. Therefore, v_p is based on physical theory and numerical experiments. v_p is taken as the sum of the convective (v_c), the acoustic (v_a) and the diffusive (v_d) velocities.

$$|d\vec{A}| \cdot v_p = |d\vec{A}| \cdot \big(v_c + v_a + v_d\big) \tag{3.10}$$

The convective velocity is given by the flow velocity $\vec{u}$ ($\vec{u}$=(u,v,w)). The acoustic velocity is given by the speed of sound a. The diffusive velocity is:

$$v_d = \frac{2\gamma\mu}{\overline{\rho}Pr}\Delta x \tag{3.11}$$

where Δx is the characteristic grid size evaluated as $\mid d\vec{A} \mid^2/V$. Therefore:

$$|d\vec{A}\cdot v_p| = \mid u.d\vec{A}_x \mid + \mid v.d\vec{A}_y \mid + \mid w.d\vec{A}_z \mid + c \mid d\vec{A} \mid + \frac{2\gamma\mu}{\overline{\rho}Pr}\frac{\mid d\vec{A} \mid^2}{V} \tag{3.12}$$

If the characteristic length scales in the three dimensions are Δx, Δy and Δz, the components of $d\vec{A}$ are dA_x=$\Delta y\Delta z$, dA_y=$\Delta x\Delta z$ and dA_z=$\Delta y\Delta z$ and the volume is $\Delta x\Delta y\Delta z$. Finally, using Eq. 3.9, the following expression is obtained:

$$\Delta t = MIN_D\Big[\frac{CFL}{\frac{|u|}{\Delta x}+\frac{|v|}{\Delta y}+\frac{|w|}{\Delta z}+c\sqrt{\frac{1}{(\Delta x)^2}+\frac{1}{(\Delta y)^2}+\frac{1}{(\Delta z)^2}}+\frac{2\gamma\mu}{\overline{\rho}Pr}\Big(\frac{1}{(\Delta x)^2}+\frac{1}{(\Delta y)^2}+\frac{1}{(\Delta z)^2}\Big)}\Big] \tag{3.13}$$

3.3 Flux Vector

In a finite-volume scheme, the different values of the variables are known at the center of each control volume. However, mass, momentum, energy and scalars fluxes are computed at the surface of each control volume. In the first part of this section, general considerations regarding the computations of the fluxes are given. In the second part of this section, the actual method used to compute these fluxes is given.

3.3.1 Control Volume, Control Surface and Fluxes

A schematic of a control volume is shown in Figure 3.1. For clarity, only a two dimensional example is shown here.

The control volume (i,j) is considered. The neighboring points control volumes are $(i+1,j)$, $(i-1,j)$, $(i,j-1)$ and $(i,j+1)$. The meshes used in this study are structured and it is therefore easy to determine the neighbors of a given cell, as well as the area that separates these two cells.

As shown in Figure 3.1, fluxes are computed at the cell surface and the fluxes in the i-direction, for example, are denoted $\vec{F}_{i-1/2,j}$ and $\vec{F}_{i+1/2,j}$.

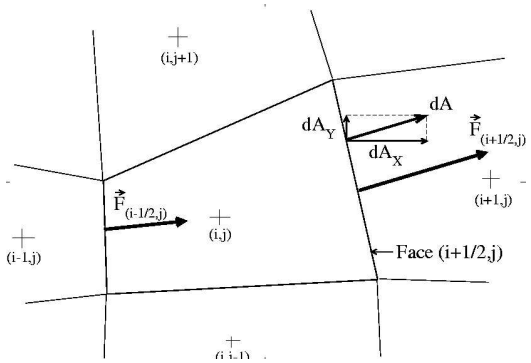

Figure 3.1: Schematic of a *LES* control volume. Fluxes ($\vec{F}$) and cell surfaces ($d\vec{A}$) are shown. For clarity, the figure is two dimensional.

3.3.2 Flux Vector Computation

3.3.2.1 General Notions

As stated previously, fluxes are computed at the cell surfaces while all information regarding the flow are localized at the center of each cell, or control volume. Therefore, interpolation techniques have to be used in order to translate information from the cell center to the cell face.

The *MacCormack* method MacCormack [1976], simply uses fluxes computed using cell center information:

$$\begin{aligned} \vec{F}^{+}_{i+\frac{1}{2}} &= \vec{F}_{i+1} \\ \vec{F}^{-}_{i+\frac{1}{2}} &= \vec{F}_{i} \end{aligned} \tag{3.14}$$

where $\vec{F}_i$ and $\vec{F}_{i+1}$ represent the fluxes computed using information from the cell i and $i+1$, respectively. The use of this technique in a *MacCormack* time integration scheme ensures a global spatial second order accurate scheme

Often, a higher order spatial accurate scheme is needed. In this study, two fourth order spatial accurate schemes are primary used. The first one is the Turkel and Gottlied scheme Turkel [1987]. The second one was developed by Nelson [1997].

In the Turkel-Gottlied scheme, the fluxes are approximated as follow:

$$\begin{aligned} \vec{F}^{+}_{i+\frac{1}{2}} &= \frac{1}{6}\Big(7\vec{F}_{i+1} - \vec{F}_{i+2}\Big) \\ \vec{F}^{-}_{i+\frac{1}{2}} &= \frac{1}{6}\Big(7\vec{F}_{i} - \vec{F}_{i-1}\Big) \end{aligned} \tag{3.15}$$

This scheme is closer to be third order accurate in space rather than fourth order. However, when compared to the MacCormack method of fluxes computation, this method is more accurate and still very stable.

In Nelson scheme, the fluxes are approximated as follow:

$$\begin{aligned} \vec{F}^{+}_{i+\frac{1}{2}} &= \frac{1}{6}\Big(2\vec{F}_{i} + 5\vec{F}_{i+1} - \vec{F}_{i+2}\Big) \\ \vec{F}^{-}_{i+\frac{1}{2}} &= \frac{1}{6}\Big(-\vec{F}_{i-1} + 5\vec{F}_{i} + 2\vec{F}_{i-1}\Big) \end{aligned} \tag{3.16}$$

This scheme is fourth order but is more unstable than the Turkel-Gottlied scheme. As a consequences, the CFL number of computation using the latest flux computation scheme is half the CFL number of computation using the MacCormack method. This is directly related to the fact that the method described by Eq. 3.16 is less dissipative than the scheme written in Eqs. 3.14 and 3.15.

Furthermore, Nelson developed a technique that interpolate information known at the cell center in order to deduce the value of the different scalars and vectors at the cell surface. The interpolation can be second order, when second order flux computational schemes are used, or fourth order, when fourth order flux computational schemes are used. In the following paragraph, this technique is described using a one dimensional example (see Figure 3.2)

The control volume (i) is considered. The neighboring control volumes are denoted $(i-1)$ and $(i+1)$. In order to compute the flux at the $i+1/2$ cell, the information are interpolated using the following formula (valid for second order interpolation):

$$AF = \frac{2d_X(i)}{D_X(i)} \tag{3.17}$$

$$Q_{i+\frac{1}{2}} = AF * Q_i \tag{3.18}$$

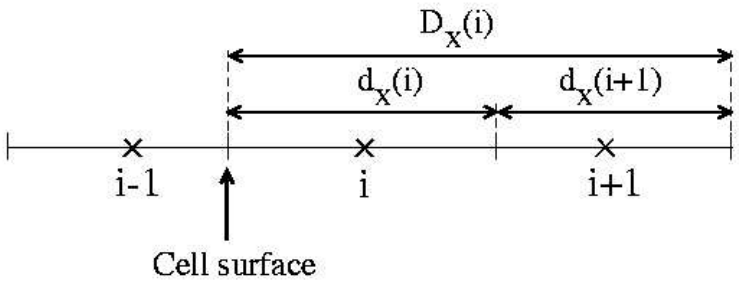

Figure 3.2: Schematic of the computational stencil. For clarity, only a one dimensional stencil is shown.

The fourth order interpolation uses the following formula:

$$\begin{aligned} AF = &\ \tfrac{2}{3}\big(1 - \tfrac{d_X(i)}{D_X(i)}\big) \\ BF = &\ \tfrac{1}{3}\big(1 + \tfrac{d_X(i+1)}{D_X(i+1)} + 2\tfrac{d_X(i)}{D_X(i)}\big) \\ CF = &\ -\tfrac{1}{3}\tfrac{d_X(i+1)}{D_X(i+1)}\big) \\ Q_{i+\frac{1}{2}} = &\ AF * Q_{i_1} + BF * Q_{i_2} + CF * Q_{i_3} \end{aligned} \tag{3.19}$$

In the forward step, i_1=$i+1$, i_2=i and i_3=$i+2$. In the backward step, i_1=i, i_2=$i-1$ and i_3=$i-2$.

This technique increases the accuracy of the flux computation but also increases the cost of the computation by approximately 60%. Furthermore, the second order correction, designed for second order spatial accuracy methods is unstable and creates numerical oscillations. However, the method is well suited for fourth order spatial accuracy methods.

3.3.2.2 Computation of the Eulerian Flux $\vec{F}^E$

Depending upon the step of the *MacCormack* scheme, the different fluxes of Q are:

$$\begin{aligned} F^-_{(i-1/2,j)} = &\ \Big(Q_{(i-1,j)}u_{(i-1,j)} + Q_{(i-1,j)}v_{(i-1,j)}\Big) \cdot dA_{(i+1/2,j)} \\ F^+_{(i-1/2,j)} = &\ \Big(Q_{(i,j)}u_{(i,j)} + Q_{(i-1,j)}v_{(i-1,j)}\Big) \cdot dA_{(i+1/2,j)} \end{aligned} \tag{3.20}$$

or

$$
\begin{aligned}
F^{-}_{(i+1/2,j)} = & \quad \Big((Q_{(i,j)}u_{(i,j)} + Q_{(i,j)}v_{(i,j)}\Big) \cdot dA_{(i+1/2,j)} \\
F^{+}_{(i+1/2,j)} = & \quad \Big((Q_{(i+1,j)}u_{(i+1,j)} + Q_{(i+1,j)}v_{(i+1,j)})\Big) \cdot dA_{(i+1/2,j)}
\end{aligned} \tag{3.21}
$$

For the *predictor* and *corrector* steps, the variation dQ of Q during Δt is computed, depending if the step is backward or forward, as:

$$
dQ_{(i,j)} = \Big(F^{-}_{(i-1/2,j)} - F^{-}_{(i+1/2,j)}\Big)\frac{\Delta t}{V} \tag{3.22}
$$

or

$$
dQ_{(i,j)} = \Big(F^{+}_{(i-1/2,j)} - F^{+}_{(i+1/2,j)}\Big)\frac{\Delta t}{V} \tag{3.23}
$$

3.3.2.3 Computation of the Viscous Flux $\vec{F}^E$ and Subgrid Flux $\vec{F}^S$

The viscous and subgrid fluxes are computed differently than the Eulerian fluxes and are function of scalar gradients. There are many ways to compute scalar gradients. However, the use of the *MacCormack* time integration scheme dictates the manner in which these gradients are computed. Gradients can be computed using a second order accurate scheme, or a fourth order accurate scheme, depending upon the desired global spatial accuracy.

In the *MacCormack* method, the computation of the fluxes is direction biased, therefore, the computation of the gradients also has to be direction biased. For example, the i-direction is considered. The i-direction derivatives are computed using either a backward or a forward formula, depending upon the *MacCormack* step. The other derivatives are computed using a central difference scheme. If we consider the scalar Ψ, its derivative in the i-direction are:

$$
\begin{array}{llll}
2^{nd} \text{ order} & \text{Backward step} & \frac{\partial \Psi}{\partial x} = \frac{\Psi_{i,j} - \Psi_{i-1,j}}{\Delta x} \\
2^{nd} \text{ order} & \text{Forward step} & \frac{\partial \Psi}{\partial x} = \frac{\Psi_{i+1,j} - \Psi_{i,j}}{\Delta x} \\
4^{th} \text{ order} & \text{Backward step} & \frac{\partial \Psi}{\partial x} = \frac{\Psi_{i-1,j} + 8\Psi_{i,j} - 7\Psi_{i+1,j}}{6\Delta x} \\
4^{th} \text{ order} & \text{Forward step} & \frac{\partial \Psi}{\partial x} = \frac{-\Psi_{i+2,j} + 8\Psi_{i+1,j} - 7\Psi_{i,j}}{6\Delta x}
\end{array} \tag{3.24}
$$

When fluxes in the i-direction are evaluated, the j-direction derivatives of Ψ are:

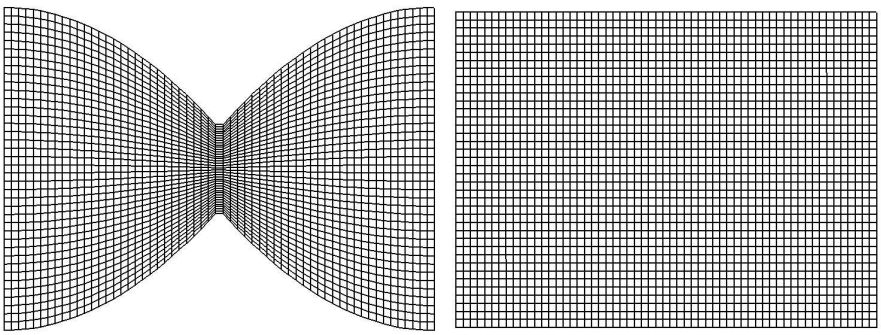

(a) Geometrical grid in the (x,y) referential.

(b) Computational grid in the (ξ,η) referential.

Figure 3.3: Geometrical and computational grids. For simplicity and clarity a two dimensional representation is given

.

$$\begin{array}{ll} 2^{nd} \text{ order} & \frac{\partial \Psi}{\partial y} = \frac{\Psi_{i,j+2} - \Psi_{i,j-1}}{\Delta y} \\ 4^{nd} \text{ order} & \frac{\partial \Psi}{\partial y} = \frac{-\Psi_{i,j+2} + 8\Psi_{i,j+1} - 8\Psi_{i,j-1} + \Psi_{i,j-2}}{\Delta y} \end{array} \tag{3.25}$$

Note that, when volumetric source term are evaluated, only central scheme are used.

3.4 Generalized Grid Coordinates

The geometrical meshes used in numerical simulations reported in this work are fitted to the geometry of interests. In engineering problems, these geometries are rarely simple and, therefore, the grids associated with these geometries are not trivial. As a results, the mesh can be highly skewed and/or highly stretched and the computational cell is often not orthogonal (as represented in Figure 3.3 (a)).

The representation in Figure 3.3 (a) is not practical to compute derivatives, Hence, the geometrical grid is transformed in a so-called computational grid which is uniform and Cartesian and the grid spacing of a computational grid is equal to unity. Such a grid is shown in Figure 3.3 (b).

Let the coordinates of the geometrical grid be (x,y,z) and the coordinates of the computational grid be (ξ,η,ζ). For example, computing the second order derivative of Ψ with regard to x is done using the following formula:

$$\frac{\partial \Psi}{\partial x} = \frac{\partial \xi}{\partial x}\frac{\partial \Psi}{\partial \xi} + \frac{\partial \eta}{\partial x}\frac{\partial \Psi}{\partial \eta} + \frac{\partial \zeta}{\partial x}\frac{\partial \Psi}{\partial \zeta} \tag{3.26}$$

where the derivatives (second order accurate) of Ψ with regard to ξ,η and ζ are easily computed as follow ($\Delta\xi$=$\Delta\eta$=$\Delta\zeta$=1):

$$\frac{\partial \Psi}{\partial \xi} = \Psi_{(i+1,j,k)} - \Psi_{(i-1,j,k)} \tag{3.27}$$
$$\frac{\partial \Psi}{\partial \eta} = \Psi_{(i,j+1,k)} - \Psi_{(i,j-1,k)} \tag{3.28}$$
$$\frac{\partial \Psi}{\partial \zeta} = \Psi_{(i,j,k+1)} - \Psi_{(i,j,k-1)} \tag{3.29}$$

The following set of formulas describes how derivatives like $\partial\xi/\ \partial x$ are computed.

$$\frac{\partial x}{\partial \xi} = \frac{x_{(i+1,j,k)} - x_{(i-1,j,k)}}{2} \tag{3.30}$$
$$\frac{\partial x}{\partial \eta} = \frac{x_{(i,j+1,k)} - x_{(i,j-1,k)}}{2} \tag{3.31}$$
$$\frac{\partial x}{\partial \zeta} = \frac{x_{(i,j,k+1)} - x_{(i,j,k-1)}}{2} \tag{3.32}$$
$$\frac{\partial y}{\partial \xi} = \frac{y_{(i+1,j,k)} - y_{(i-1,j,k)}}{2} \tag{3.33}$$
$$\frac{\partial y}{\partial \eta} = \frac{y_{(i,j+1,k)} - y_{(i,j-1,k)}}{2} \tag{3.34}$$
$$\frac{\partial y}{\partial \zeta} = \frac{y_{(i,j,k+1)} - y_{(i,j,k-1)}}{2} \tag{3.35}$$
$$\frac{\partial z}{\partial \xi} = \frac{z_{(i+1,j,k)} - z_{(i-1,j,k)}}{2} \tag{3.36}$$
$$\frac{\partial z}{\partial \eta} = \frac{z_{(i,j+1,k)} - z_{(i,j-1,k)}}{2} \tag{3.37}$$
$$\frac{\partial z}{\partial \zeta} = \frac{z_{(i,j,k+1)} - z_{(i,j,k-1)}}{2} \tag{3.38}$$

Furthermore, using the chain rule, we have:

$$\underbrace{\begin{bmatrix} \frac{\partial x}{\partial \xi} & \frac{\partial x}{\partial \eta} & \frac{\partial x}{\partial \zeta} \\ \frac{\partial y}{\partial \xi} & \frac{\partial y}{\partial \eta} & \frac{\partial y}{\partial \zeta} \\ \frac{\partial z}{\partial \xi} & \frac{\partial z}{\partial \eta} & \frac{\partial z}{\partial \zeta} \end{bmatrix}}_{M} \begin{bmatrix} \frac{\partial}{\partial x} \\ \frac{\partial}{\partial x} \\ \frac{\partial}{\partial x} \end{bmatrix} = \begin{bmatrix} \frac{\partial}{\partial \xi} \\ \frac{\partial}{\partial \eta} \\ \frac{\partial}{\partial \zeta} \end{bmatrix} \tag{3.39}$$

The matrix M is known as the inverse *grid matrix*. M^{-1} is known as the *grid metrics* and is used to compute $\partial/\partial x$, $\partial/\partial y$ and $\partial/\partial z$.

$$\underbrace{\begin{bmatrix} \frac{\partial \xi}{\partial x} & \frac{\partial \xi}{\partial y} & \frac{\partial \xi}{\partial z} \\ \frac{\partial \eta}{\partial x} & \frac{\partial \eta}{\partial y} & \frac{\partial \eta}{\partial z} \\ \frac{\partial \zeta}{\partial x} & \frac{\partial \zeta}{\partial y} & \frac{\partial \zeta}{\partial z} \end{bmatrix}}_{M^{-1}} \begin{bmatrix} \frac{\partial}{\partial \xi} \\ \frac{\partial}{\partial \eta} \\ \frac{\partial}{\partial \zeta} \end{bmatrix} = \begin{bmatrix} \frac{\partial}{\partial x} \\ \frac{\partial}{\partial y} \\ \frac{\partial}{\partial z} \end{bmatrix} \tag{3.40}$$

Because derivatives are computed at each surfaces of the control volume, a set of three *grid metrics* matrix (one for each directions) is needed. Some derivatives are computed at the cell center and, as a consequence, the total number of *grid metrics* matrix necessary is four.

3.5 Boundary Conditions

LES simulation of compressible flows requires an accurate control of wave reflections from the boundaries of the computational domain. The initial flow instabilities as well as the growth of non-reacting shear layers are sensitive to the behavior and characteristics of these acoustic waves.

The derivation of the boundary conditions used in this study follows the work of Poinsot and Lele [1992]. The general set of equations is derived and discussed in the next section. Then, the method is applied for different types of boundary conditions (section 3.5.2).

3.5.1 Characteristic Boundary Conditions

The technique used in the derivation of the boundary conditions Poinsot et al. [1991] uses relations based on the analysis of the different waves crossing the domain boundary. This approach is valid in any hyperbolic system of equations.

In the rest of the section, boundary conditions are derived for boundaries located in the $y-z$ plane. Therefore, for all expression regarding the boundary conditions, the derivatives $\partial/\partial x$ (denoted d_i in Eq. 3.41) can not be computed and have to be modeled.

The set of filtered Navier-Stokes equations (See Eq. 2.14) is rewritten as:

$$
\left\{
\begin{array}{l}
\frac{\partial \overline{\rho}}{\partial t} + d_1 + \frac{\partial \overline{\rho}\widetilde{u_2}}{\partial x_2} = 0 \\
\frac{\partial \overline{\rho}\widetilde{u_1}}{\partial t} + \widetilde{u_1}d_1 + \overline{\rho}d_3 \ + \frac{\partial \overline{\rho}\widetilde{u_1}\widetilde{u_2}}{\partial x_2} + \frac{\partial \overline{\rho}\widetilde{u_1}\widetilde{u_3}}{\partial x_3} = \frac{\partial \tau_{1j}}{\partial x_j} \\
\frac{\partial \overline{\rho}\widetilde{u_2}}{\partial t} + \widetilde{u_2}d_1 + \overline{\rho}d_4 \ + \frac{\partial \overline{\rho}\widetilde{u_2}\widetilde{u_2}}{\partial x_2} + \frac{\partial \overline{\rho}\widetilde{u_2}\widetilde{u_3}}{\partial x_3} = \frac{\partial \tau_{2j}}{\partial x_j} \\
\frac{\partial \overline{\rho}\widetilde{u_3}}{\partial t} + \widetilde{u_3}d_1 + \overline{\rho}d_5 \ + \frac{\partial \overline{\rho}\widetilde{u_3}\widetilde{u_2}}{\partial x_2} + \frac{\partial \overline{\rho}\widetilde{u_3}\widetilde{u_3}}{\partial x_3} = \frac{\partial \tau_{3j}}{\partial x_j} \\
\frac{\partial \overline{\rho}\widetilde{E}}{\partial t} + \overline{\rho}\widetilde{u_1}d_3 + \overline{\rho}\widetilde{u_2}d_4 + \overline{\rho}\widetilde{u_3}d_5 + \frac{1}{2}\Big(\frac{\partial(\widetilde{u_1}\widetilde{u_1})}{\partial x_1} + \frac{\partial(\widetilde{u_2}\widetilde{u_2})}{\partial x_2} + \frac{\partial(\widetilde{u_3}\widetilde{u_3})}{\partial x_3}\Big) \\
+\frac{d_2}{\gamma-1} + \frac{\partial}{\partial x_2}\Big(\overline{\rho}\widetilde{E} + \overline{p}\Big)\widetilde{u_2} + \frac{\partial}{\partial x_3}\Big(\overline{\rho}\widetilde{E} + \overline{p}\Big)\widetilde{u_3} + \Big[\Big(\widetilde{e} - \frac{a^2}{\gamma(\gamma-1)}\Big)d_1\Big] \\
+\sum_{m=1}^{N}\overline{\rho}d_{6+m}\Big[\widetilde{e_m} - \frac{\widetilde{R_u}\widetilde{T}}{MW_m(\gamma-1)}\Big] = -\frac{\partial \overline{q_j}}{\partial x_j} + \frac{\partial(\widetilde{u_i}\overline{\tau_{ij}})}{\partial x_j} \\
\frac{\partial \overline{\rho}k^{sgs}}{\partial t} + k^{sgs}d_1 + \overline{\rho}d_6 + \frac{\partial(\overline{\rho}\widetilde{u_2}k^{sgs})}{\partial x_2} + \frac{\partial(\overline{\rho}\widetilde{u_3}k^{sgs})}{\partial x_3} = \\
\frac{\partial}{\partial x_j}\Big(\overline{\rho}\nu_t\frac{\partial k^{sgs}}{\partial x_j}\Big) + P^{sgs} - D^{sgs} \\
\frac{\partial \overline{\rho}\widetilde{Y_m}}{\partial t} + \widetilde{Y_m}d_1 + \overline{\rho}d_{6+m} + \frac{\partial(\overline{\rho}\widetilde{u_2}\widetilde{Y_m})}{\partial x_2} + \frac{\partial(\overline{\rho}\widetilde{u_3}\widetilde{Y_m})}{\partial x_3} = \\
\frac{\partial}{\partial x_j}\Big(\overline{\rho}D_m\frac{\partial \widetilde{Y_m}}{\partial x_j}\Big) + \overline{\rho}\widetilde{\dot{w}}_m, m = 1, N
\end{array}
\right. \tag{3.41}
$$

where the different derivatives with regard to the x-direction are:

$$
\vec{d} = \begin{pmatrix} d_1 \\ d_2 \\ d_3 \\ d_4 \\ d_5 \\ d_6 \\ d_{6+m} \end{pmatrix} = \begin{pmatrix} \frac{\partial \overline{\rho}\widetilde{u_1}}{\partial x_1} \\ \overline{\rho}c^2\frac{\partial \widetilde{u_1}}{\partial x_1} + \widetilde{u_1}\frac{\partial \overline{p}}{\partial x_1} \\ \widetilde{u_1}\frac{\partial \widetilde{u_1}}{\partial x_1} + \frac{1}{\overline{\rho}}\frac{\partial \overline{p}}{\partial x_1} \\ \widetilde{u_1}\frac{\partial \widetilde{u_2}}{\partial x_1} \\ \widetilde{u_1}\frac{\partial \widetilde{u_3}}{\partial x_1} \\ \widetilde{u_1}\frac{\partial k^{sgs}}{\partial x_1} \\ \widetilde{u_1}\frac{\partial \widetilde{Y_m}}{\partial x_1} \end{pmatrix} = \begin{pmatrix} \frac{1}{c^2}\Big[\mathscr{L}_2 + \frac{1}{2}\Big(\mathscr{L}_5 + \mathscr{L}_1\Big)\Big] \\ \frac{1}{2}\Big(\mathscr{L}_5 + \mathscr{L}_1\Big) \\ \frac{1}{2\overline{\rho}c}\Big(\mathscr{L}_5 - \mathscr{L}_1\Big) \\ \mathscr{L}_3 \\ \mathscr{L}_4 \\ \mathscr{L}_6 \\ \mathscr{L}_{6+m} \end{pmatrix} \tag{3.42}
$$

where the $\mathscr{L}_i$'s are the amplitudes of the characteristic waves associated with each eigenvalue λ_i:

$$\vec{\lambda} = \begin{pmatrix} \lambda_1 \\ \lambda_2 \\ \lambda_3 \\ \lambda_4 \\ \lambda_5 \\ \lambda_6 \\ \lambda_{6+m} \end{pmatrix} = \begin{pmatrix} \widetilde{u_1} - c \\ \widetilde{u_1} \\ \widetilde{u_1} \\ \widetilde{u_1} \\ \widetilde{u_1} + c \\ \widetilde{u_1} \\ \widetilde{u_1} \end{pmatrix} \tag{3.43}$$

where c is the speed of sound (c=$\sqrt{\gamma \widetilde{R_u} \widetilde{T}}$). λ_1 and λ_5 are the velocity of the sound waves in the positive and negative x_1-direction; λ_2 is the convection velocity (the speed of the entropy wave), λ_3, λ_4, λ_6 and λ_{6+m} are the velocity at which $\widetilde{u_2}$, $\widetilde{u_3}$, k^{sgs} and $\widetilde{Y_m}$ are advected in the x_1-direction, respectively.

The $\mathscr{L}_i$'s are given by:

$$\begin{pmatrix} \mathscr{L}_1 \\ \mathscr{L}_2 \\ \mathscr{L}_3 \\ \mathscr{L}_4 \\ \mathscr{L}_5 \\ \mathscr{L}_6 \\ \mathscr{L}_7 \end{pmatrix} = \begin{pmatrix} \lambda_1 \left(\frac{\partial \overline{p}}{\partial x_1} - \overline{\rho} c \frac{\partial \widetilde{u_1}}{\partial x_1} \right) \\ \lambda_2 \left(c^2 \frac{\partial \overline{\rho}}{\partial x_1} - \frac{\partial \overline{p}}{\partial x_1} \right) \\ \lambda_3 \frac{\partial \widetilde{u_2}}{\partial x_1} \\ \lambda_4 \frac{\partial \widetilde{u_3}}{\partial x_1} \\ \lambda_5 \left(\frac{\partial \overline{p}}{\partial x_1} + \overline{\rho} c \frac{\partial \widetilde{u_1}}{\partial x_1} \right) \\ \lambda_6 \frac{\partial k^{sgs}}{\partial x_1} \\ \lambda_{6+m} \frac{\partial \widetilde{Y_m}}{\partial x_1} \end{pmatrix} \tag{3.44}$$

From the analysis of Poinsot et al. [1991], Local One-Dimensional Inviscid ($LODI$) relations are obtained. This approach is used to infer values of the wave amplitude variations in the viscous, three-dimensional Navier-Stokes equations. The $LODI$ relations are:

$$
\begin{aligned}
\frac{\partial \overline{\rho}}{\partial t} + \frac{1}{c^2}\Big[\mathscr{L}_2 + \frac{1}{2}\big(\mathscr{L}_5 + \mathscr{L}_1\big)\Big] &= 0 \\
\frac{\partial \overline{p}}{\partial t} + \frac{1}{2}\big(\mathscr{L}_5 + \mathscr{L}_1\big) &= 0 \\
\frac{\partial \widetilde{u_1}}{\partial t} + \frac{1}{2\overline{\rho}c}\big(\mathscr{L}_5 - \mathscr{L}_1\big) &= 0 \\
\frac{\partial \widetilde{u_2}}{\partial t} + \mathscr{L}_3 &= 0 \\
\frac{\partial \widetilde{u_3}}{\partial t} + \mathscr{L}_4 &= 0
\end{aligned}
\tag{3.45}
$$

Based on the above set of characteristic wave equations and their amplitudes, different boundary computations can be computed.

3.5.2 Derivation of the Boundary Conditions

In this section, different boundary conditions are derived. The boundary conditions of interest are:

- Subsonic Inflow (Section 3.5.2.1).
- Subsonic partially reflecting outflow (Section 3.5.2.2).
- No flux, no-slip wall boundary conditions (Section 3.5.2.3).

3.5.2.1 Subsonic Inflow Boundary Conditions

In this study, u_1, u_2 and u_3 as well as the inflow temperature T are imposed at the inflow. This case is typical of LES of turbulent reacting flows, where we wish to control the inlet shear and introduce flow perturbations. For a subsonic, three dimensional, $N-$species reacting flow, five+N characteristic waves enter the domain; namely $\mathscr{L}_2$, $\mathscr{L}_3$, $\mathscr{L}_4$, $\mathscr{L}_5$, $\mathscr{L}_6$ and $\mathscr{L}_{6+N}$. $\mathscr{L}_1$ leaves the domain at λ_1=$u_1 - c$. The density ρ has to be determined from the local flow conditions. The following technique is used:

Step 1. The know inlet conditions are imposed (namely, u_1, u_2, u_3, T and Y_m). As a results, the second, third and forth relation from Eq. 3.41 are not needed.

Step 2. As u_1 and p are fixed, $\mathscr{L}_1$ can be deduced:

$$
\mathscr{L}_1 = (u_1 - c)\Big(\frac{\partial \overline{p}}{\partial x_1} - \overline{\rho}c\frac{\partial \widetilde{u_1}}{\partial x_1}\Big) \tag{3.46}
$$

where:

$$\frac{\partial \overline{p}}{\partial x_1} = \frac{\overline{p}(1,j,k) - \overline{p}(0,j,k)}{\Delta x} \tag{3.47}$$

$$\frac{\partial \widetilde{u_1}}{\partial x_1} = \frac{\widetilde{u_1}(1,j,k) - \widetilde{u_1}(0,j,k)}{\Delta x} \tag{3.48}$$

Here, the inflow plane is located at i=0 and Δx is the grid spacing between the inflow cell at i=0 and the first cell at i=1.

Step 3. As T is fixed, $\mathscr{L}_5$ can be deduced using the third relation of Eq. 3.42:

$$\mathscr{L}_5 = \mathscr{L}_1 - \frac{1}{2}\overline{\rho}c\frac{\partial \widetilde{u_1}}{\partial t} \tag{3.49}$$

where:

$$\frac{\partial \widetilde{u_1}}{\partial t} = \frac{\widetilde{u_1}(t+\Delta t) - \widetilde{u_1}(t)}{\Delta t} \tag{3.50}$$

Step 4. Using Eq. the second relation of Eq. 3.44:

$$\mathscr{L}_2 = \frac{1}{2}\big(\gamma - 1\big)\big(\mathscr{L}_5 + \mathscr{L}_1\big) + c^2\frac{\partial \overline{\rho}}{\partial t} \tag{3.51}$$

where $\partial\overline{\rho}/\partial t$ is unknown and is computed as:

$$\frac{\partial \overline{\rho}}{\partial t} = \frac{\overline{\rho}}{\widetilde{T}}\frac{\partial \widetilde{T}}{\partial t} \tag{3.52}$$

$$\frac{\partial \widetilde{T}}{\partial t} = \frac{\widetilde{T}(t+\Delta t) - \widetilde{T}(t)}{\Delta t} \tag{3.53}$$

Step 5. Finally, d_1 is computed as:

$$d_1 = \frac{1}{c^2}\Big[\mathscr{L}_2 + \frac{1}{2}\big(\mathscr{L}_1 + \mathscr{L}_5\big)\Big] \tag{3.54}$$

and:

$$d\overline{\rho} = -d_1 * \Delta t \tag{3.55}$$

In this case, $\mathscr{L}_3$ and $\mathscr{L}_4$ are not needed.

3.5.2.2 Partially Reflecting Subsonic Outflow

For this outflow boundary condition, the pressure at the outlet (p_∞) is imposed. As a result, the fifth relation of Eq. 3.41 is not needed.

Step 5. The condition of constant p_∞ is used to compute the amplitude variation of the ingoing wave $\mathscr{L}_1$. If the current pressure $\overline{p}$ at the outlet is different from p_∞, reflected waves will enter the domain through the outlet to bring the pressure back to p_∞. Therefore:

$$\mathscr{L}_1 = \beta\big(\overline{p} - p_\infty\big) \tag{3.56}$$

with:

$$\beta = \sigma\big(1 - \mathscr{M}^2\big)\frac{c}{L} \tag{3.57}$$

where $\mathscr{M}$ is the maximum Mach number in the flow, L is a characteristic length scale and σ is the reflection coefficient which sets the amplitude of the reflected waves.

3.5.2.3 No-Flux, Adiabatic Wall Boundary Conditions

This is a straightforward boundary condition. If the wall is located in the y-z plane and between the x-direction coordinates i and $i+1$ (this is the case in finite volume scheme), the no-flux wall boundary conditions are:

$$\begin{aligned}
\overline{\rho}(i+1) &= \overline{\rho}(i) \\
\widetilde{u}_1(i+1) &= -\widetilde{u}_1(i) \\
\widetilde{u}_2(i+1) &= C\widetilde{u}_2(i) \\
\widetilde{u}_3(i+1) &= C\widetilde{u}_3(i) \\
\widetilde{T}(i+1) &= \widetilde{T}(i) \\
k^{sgs}(i+1) &= -k^{sgs}(i) \\
\widetilde{Y}_m(i+1) &= \widetilde{Y}_m(i)
\end{aligned} \tag{3.58}$$

where C=1 for slip wall boundary condition and C=−1 for no-slip wall boundary condition.

3.6 Finite Rate Reaction Rates Computation

The mass reaction rate is computed using either a 1-step [Westbrook and Dryer, 1981] chemical mechanism or a 4-step [Card et al., 1994] chemical mechanism. These mechanisms are summarized below. Mechanism A: 1-step:

$$CH_4 + 2O_2 + N_2 \rightleftharpoons CO_2 + 2H_2O + N_2 \tag{3.59}$$

Mechanism B: 4-step:

$$\begin{aligned} CH_4 + 2H + H_2O + N_2 &\rightleftharpoons CO + 4H_2 + N_2 \\ CO + H_2O &\rightleftharpoons CO_2 + H_2 \\ 2H + M &\rightleftharpoons H_2 + M \\ O_2 + 3H_2 &\rightleftharpoons 2H + 2H_20 \end{aligned} \tag{3.60}$$

For these two mechanisms, the cost of direct integration is prohibitive. In this study, the use of an In-Situ-Adaptive-Tabulation ($ISAT$) method was proved to not speed-up the chemical rates computation. Instead, a simple, cost effective and accurate method for the computation of the reaction rates is used. This method is valid for both chemical mechanisms and is described below.

The idea behind the $ISAT$ Pope [1997] method is to store reaction rates computed via direct integration as a function of the initial species mass fraction and temperature. As the computation progresses, more and more reaction rates are obtained by retrieving informations from the table rather than re-computing them via direct integration. As long as the table is not too large, the computational time needed to retrieve information is smaller than the time required to perform the direct integration. In other studies Sankaran and Menon [2000], this speed-up was found to be of the order of 30 (16-species mechanism). However, this speed-up is directly related to the actual computational time step and the ratio of the $ISAT$ table size to the total number of computational points.

First, the influence of the computational time step is analyzed. The larger the integration time step, the larger the number of chemical integration time steps of direct integration. In the study of Sankaran et al., the time step is set to 10^{-6} second. If a direct integration method using the $DVODE$ (Double precision and Variable coefficient ODE solver) is employed, a large number of $DVODE$ iteration steps is needed to compute the reaction rate over 10^{-6} second and the computational time required for this direct integration is large. When the $ISAT$ method is used, the computational time for retrieval from the table is much smaller, therefore, $ISAT$ allows a speed-up of the computation of the order of 30. However, in the full-scale combustion chamber simulations presented in this work, the computational

time step is of the order of 10^{-7} second. The number of iterations needed to compute the reaction rate over 10^{-7} second is ten times smaller than its computation over 10^{-6} second, while the computational time for retrieval from the $ISAT$ table is the same. Therefore, the speed-up related to the use of $ISAT$ decreases by a factor of ten and is only 3.

The second relevant parameter is the ratio of the $ISAT$ table size (N_{ISAT}) to the total number of computational points (N_{PTS}). In the previous study Sankaran and Menon [2000], the number of mixture states (species mass fraction and temperature) that could be stored in the table was of the order of 10,000 while the number of computational points was of the order of 250 ($N_{ISAT}/N_{PTS} = 40$). In the computations presented here, N_{ISAT} is chosen to be 20,000 while the average N_{PTS} is 320,000 (this number is equal to the number of points per processor multiplied by the number of LEM cells). In this case, $N_{ISAT}/N_{PTS} = 0.0625$. When $N_{ISAT}/N_{PTS}>>1$, the table is never filled and quasi-irrelevant information (i.e. mixture states that have a low probability of occurrence) can be stored without impacting the retrieval speed (note that the larger the amount of information stored in the table, the larger the time needed to retrieve a given reaction rate). However, when $N_{ISAT}/N_{PTS}<<1$, the $ISAT$ table is saturated after only a limited number of computational steps and the cost of retrieving the information becomes comparable to the cost of performing a direct integration (this is especially true for both the 5- and the 4-step chemical mechanisms).

In the computation performed in this study, the limiting factor for the use of $ISAT$ is the fast rate of information storage in the table. This would not be a problem if the table would fill less rapidly. One solution to achieve this goal is to reduce the accuracy of the retrieval of information in the table. The larger the allowed error on the retrieval of the reaction rates, the larger the probability of retrieval, the smaller the probability of the use of direct integration and the slower the rate of growth of the table. For obvious reasons (accuracy consideration), this solution can not be considered. Another solution is to reduce the actual chemical integration time. It has been observed that, when the chemical integration time step (τ_{ci}) is lower than a critical time step (τ_{crit}), the growth rate of the $ISAT$ table is relatively low, whereas when $\tau_{ci}>\tau_{crit}$, the growth rate of the $ISAT$ table is exponential. In this work, τ_{crit} is of the order of 10^{-8} second, ten time smaller

than the computational time step. As a consequence, τ_{ci} is chosen to be τ_{crit} and the number of chemical integration performed during a given computational time step (Δt_{LES}) is chosen as the ratio of the computational time step to τ_{crit}. For the studies reported in this work, ten chemical integrations were performed for each computational time step. Using this method, the table growth rate was low and thousands of iteration can be completed without saturating the $ISAT$ table. However, in this case, both for the 1- and 4-step chemical mechanisms, the cost of ten chemical integrations, even when the retrieval rate from the table was extremely high, is larger than the cost of direct integration. Therefore, the $ISAT$ method was not used in this work. Note that, for a 16-species mechanism, the approach described above is valid, but still extremely computationally expensive.

The cost of direct integration being prohibitive, a solution had to be found to ensure an accurate and fast computation of the chemical reaction rates. This was done by studying the direct integration algorithm (i.e. $SVODE$) and its behavior. For both chemical mechanisms, the computation of the reaction rate per computational time step is performed by dividing the actual LES computational time step and performing a direct computation of the reactions rate over this smaller time step. It was found that the time step used by the $SVODE$ (Δt_{SVODE}) algorithm is fairly constant. Hence, $K\Delta t_{SVODE}$=Δt_{LES}.

As a result, the computation of the reaction rate is performed directly at the time step Δt_{SVODE} and K times during a LES time step. Δt_{SVODE} is determined by studying the chemical mechanism on a $1D$ problem. K is defined as $\Delta t_{LES}/\Delta t_{SVODE}$ and is an input to the LES program. Replacing the use of $SVODE$ to compute the local Δt_{SVODE} by a fixed Δt_{SVODE} speed the LES computation. The species mass fraction at time $n+1$ is therefore computed as:

$$Y^{n+1} = Y^n + \sum_{k=1}^{K} \dot{w}(Y^{k-1})\Big(\frac{\Delta t_{LES}}{K}\Big) \tag{3.61}$$

where Y^0=Y^n.

The accuracy of this method is shown in Table 3.2. For the computations considered in this study, K is fixed to 5 and 16 for the 1- and 4-step mechanism, respectively. This technique tends to be more accurate for the 1-step mechanism. Note the different trends for

Table 3.2: Accuracy of the method for the computation of the reaction rates (in percentage). The reaction rates computed with the method described in the above paragraph is $\dot{w}_{step}$ and is compared to the reaction rates computed with the ODE solver ($\dot{w}_{ODE}$). The error in computed as ($|\dot{w}_{step} - \dot{w}_{ODE}|$) / ($|\dot{w}_{ODE}|$). C describe the number of chemical iterations performed per LES time step. C=0 means that 1 chemical iteration is performed. For larger values of C, CN iteration are performed, where N is the number of species in the chemical mechanism

	Φ=0.45		Φ=1.0	
C	1-step	4-step s	1-step	4-step
0	0.5	45.0%	1.4	16.0%
1	0.3	10.0%	1.0	3.0%
2	0.3	3.0%	1.0	1.5%
3	0.3	2.0%	1.0	1.0%

both mechanisms; for the 1-step mechanism, the technique is more accurate for low values of Φ while, for the 4-step mechanism, the technique is more accurate for large values of Φ.

This method is also time expensive but four times faster than direct integration via $SVODE$ for the 1-step chemical mechanism and three times faster for the 4-step chemical mechanism (see Table 6.2).

3.7 Parallel Implementation and Performance

To perform the computations described in this work, a large amount of memory is required. As a results, memory sharing has to be used and the computational grid is equally divided into separates sub-elements. Each sub-element is assigned to a single processor. Therefore, the entire computation is divided between many processors and makes the LES technique affordable.

Because memory is divided, processors have to communicate to each others to exchange different information related to the computation. The two main information that are shared are the global LES time step (Δt_{LES}) and variables (mass, momentum and scalars) at the boundary of each sub-element of the grid. These variables are used as boundary conditions for the computations at the sub-element (or processor) level. This is made possible by the use of the Message-Passing Interface (MPI) protocol.

The performance of the solver used in this study was evaluated and the speed-up is

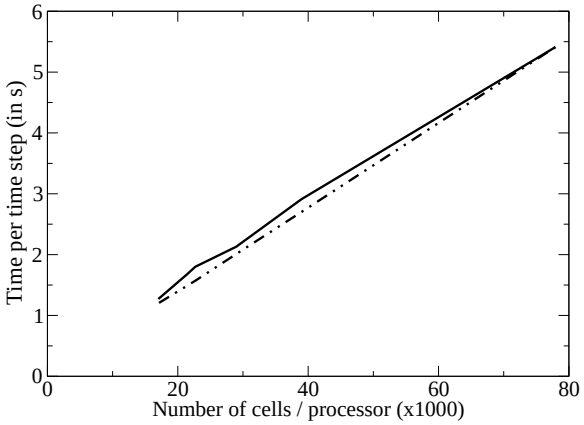

Figure 3.4: Time needed to perform one LES iteration as a function of the number of LES points per processor. Solid line: speed-up of the $LEMLES$ solver - dashed line: ideal speed-up.

presented in Figure 3.4. Computational times were obtained using the $LEMLES$ approach with 18 LEM cells per LEM domain and with the 1-step chemical mechanism. Computational times are plotted as a function of the number of LES cells contained in each grid sub-elements, i.e. the number of computational points per processor. As a reference, ideal computation times are plotted. Computational times are said to be 'ideal' when a increase of the number of processors by a factor of N leads to a decrease in computational time by a factor of N. As shown in Figure 3.4, the behavior of the program is close to the ideal behavior. This contradicts previous results Stone and Menon [2001] which showed that, as the number of processors increases, the computation time required for message passing becomes more important, hence the gain of computational time is only a fraction of the ideal gain when the number of processors increases. This contradiction can easily be explained. In the $LEMLES$ model, a large fraction of the computational cost (57% and 65% for the 1- and 4-step chemical mechanism, respectively) is due to the computation of the reaction rates. Hence, because the other sub-programs have a low computational cost when compared to the cost of the computation of the reaction rates, the later controls the cost of the whole computations. For example, if the number of processors is multiplied by two, the number of points where the chemical rates are computed is divided by two and the computational cost is also divided by two.

3.8 Combustion Chamber Geometries

3.8.1 DOE-HAT Combustion Chamber

The geometry of the DOE-HAT combustor is shown in Figure 3.5 (a). In this combustor, the swirling premixed mixture enters the combustor through an annular slot. The flame is stabilized by the recirculation at the base of the dump-plane and also by the recirculation created by the center bluff-body. The length of the combustion chamber is 0.5 m, its radius is R = 0.053 m and the inlet is located between 0.0173 m and 0.0314 m from the centerline. The inflow conditions mimic, as much as possible, the experiment data: the fuel is methane (CH_4) and the reactants enter the combustor with a temperature of 700 K, a pressure of 1.378 MPa, and a mean inflow velocity of 68.6 m/s. The inflow swirl number is 0.6. The swirl number is defined as the ratio of tangential momentum divided over the axial momentum and is computed using the following formula:

$$S = \frac{\int_0^R \rho u_x u_\theta r^2 dr}{R \int_0^R \rho u_x u_x r dr} \tag{3.62}$$

The Reynolds number (based on the inlet velocity and the diameter of the center-body) is 230,000. Inflow profile and inflow turbulence level are obtained from experimental data. No-slip adiabatic wall, and characteristic based inflow and outflow boundary conditions Poinsot and Lele [1992] are employed for all the reported simulations. The inflow equivalence ratio ranges from 0.41 to 0.53.

3.8.2 Dump Combustor

The combustion inside the dump combustor is simulated using a three dimensional geometry. Dimensions are given on Figure 3.6. The grid resolution is 140x75x81 for the cylindrical grid that fits the combustion chamber geometry and 140x21x21 for the Cartesian grid that is used to resolve the centerline region. The inflow pressure is 6 bar, the inflow temperature is 644 K and the reacting mixture is a premixed mixture of methane and air. Operating conditions were chosen to match the General Electric LM6000 combustion chamber, to ensure realistic operating conditions.

Four different simulations are conducted. The first simulation (Case 1) models the propagation of a premixed flame. The equivalence ratio (Φ) is 1. The inflow equivalence

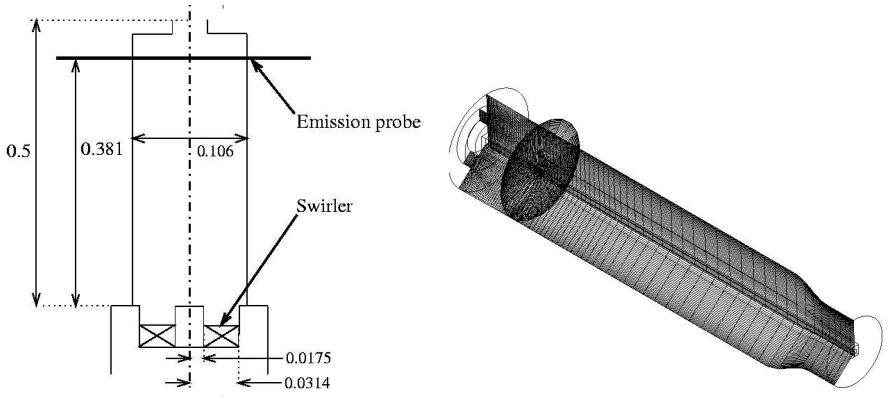

(a) (b)

Figure 3.5: Geometry and dimensions of the DOE-HAT combustor. Dimension are given in meters. The location of the emission probe where CO and NO was obtained is also shown

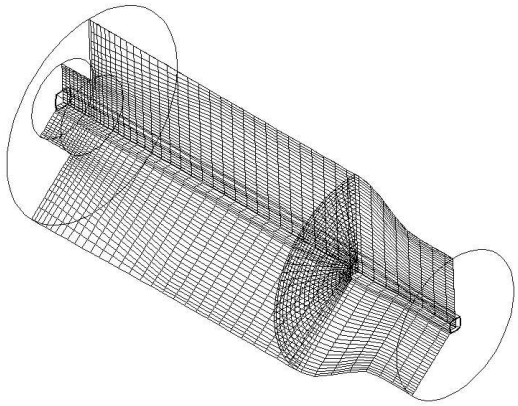

Figure 3.6: General view of the computational domain. The total combustion chamber length is 0.21m. The length of the inflow pipe is 0.015m. The radius of the combustion chamber and the inflow pipe are 0.045m and 0.017m, respectively. The centerline region is meshed using a Cartesian grid and the rest of the domain is meshed using a cylindrical grid. Both grids are continuous. For the cylindrical grid, the resolution is 140x75x81 grid points in the axial,radial and circumferential directions, respectively. For the Cartesian grid, the resolution is 140x21x21 grid points in the axial, horizontal and vertical directions, respectively.

ratio is uniform in space and time. The second test (Case 2) is identical to the first one, but the inflow reactant equivalence ratio is 0.45, close to the flammability limit of the mixture. The inflow equivalence ratio of the third simulation (Case 3) is uniform in time but non-uniform in space. Φ varies from 0.30 at the wall of the inflow pipe to 0.7 in the centerline region. The inflow equivalence ratio of the fourth simulation (Case 4) uniform in space but varies in time, Φ decreases from 1.0 to 0.45 and increases back to 1.0 with a frequency of 300 Hz. Many cycles are simulated. Heat losses are simulated in case 1, 2 and 4. For case 3, the equivalence ratio uniformities leads to flame lift-off and heat losses are not required.

3.8.3 Chemical Mechanisms Used for the Different Geometries

Due to computation costs, a full chemical mechanism can not be used in the current simulations, therefore, reduced mechanism have to be used.

Besides the G-equation model, a 1-step global mechanism (see Eq. 3.59) is used in the $DOE-HAT$ combustor pollutant emission study. This model is used in the $LEMLES$ approach.

For all the dump combustor $LEMLES$ studies, finite-rate kinetic is employed within the subgrid LEM model. Two chemical mechanisms are used in this work: a 1-step global mechanism (see Eq. 3.59) and a 4-step reduced mechanism (see Eq. 3.60).

3.9 Computational Grid

3.9.1 Resolution of the Centerline Region

In order to resolve shear layer and flame features without being restricted by the cylindrical grid restriction at the centerline, a two-grid approach is employed in this work. The region near the centerline is resolved using a Cartesian grid whereas a cylindrical grid is used elsewhere. Second-order interpolation between the two grid is employed to transfer information back and forth. This two-grid approach is shown in Figure 3.8. For the $DOE-HAT$ combustor, all the combustion process occur in regions far from the centerline and the two-grid approach effectively eliminates the centerline time restriction without impacting the physics of interest. Studies were conducted by varying the grid resolution and the size of the inner grid to ensure smooth continuity between the solution in the two grids and also to ensure

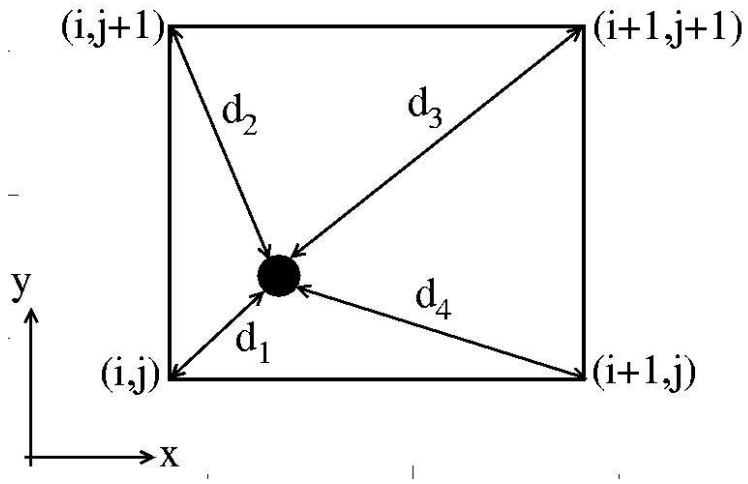

Figure 3.7: Schematic of the stencil used in the interpolation method. • represents the point where the value of f has to be known. The *closest* points where the value of f is known is denoted by the indexes i and j.

grid independence is achieved for the resolved scales.

This numerical algorithm is implemented in parallel using Message-Passing Interface (MPI). The two grids overlap, and so once the MPI operations are completed, the interpolation depends only on the information contained in one grid. In the present application, a 2D interpolation at each axial location is carried out and seems to suffice. A quantity f at a location (x,y) is determined by interpolating the values of the neighboring points. The interpolation uses a third order polynomial function and is second order in space. The polynom has the following form:

$$f(x,y) = a_1x^3 + a_2x^2y + a_3xy^3 + a_4y^3 + a_5x^2 + a_6xy + a_7y^2 + a_8x + a_9y + a_{10} \quad (3.63)$$

where the coefficients a_l, l ranging from 1 to 10, have to be determined. An example of the interpolation technique is given below.

The value of f has to be known at the location (x,y). The *closest* points where the value of f is known is located at x=x_0 and y=y_0 and is denoted by the indexes i and j. The three other closest point are indexed ($i+1$,j), (i,$j+1$) and ($i+1$,$j+1$). A schematic is shown in Figure 3.7.

The 10 unknowns (a_1 to a_{10}) are determined using the value of f and their derivatives

at the four closest points. The 10 informations (b_l) required to determines these unknowns are:

$$
\begin{aligned}
b_1 &= f(i,j) && (3.64)\\
b_2 &= f(i+1,j) && (3.65)\\
b_3 &= f(i,j+1) && (3.66)\\
b_4 &= f(i+1,j+1) && (3.67)\\
b_5 &= \frac{\partial f}{\partial x}(i,j) && (3.68)\\
b_6 &= \frac{\partial f}{\partial x}(i+1,j) && (3.69)\\
b_7 &= \frac{\partial f}{\partial x}(i,j+1) && (3.70)\\
b_8 &= \frac{\partial f}{\partial y}(i,j) && (3.71)\\
b_9 &= \frac{\partial f}{\partial y}(i+1,j) && (3.72)\\
b_{10} &= \frac{\partial f}{\partial y}(i,j+1) && (3.73)\\
& && (3.74)
\end{aligned}
$$

If Δx is the grid spacing in the x-direction and Δy is the grid spacing in the y-direction, the derivatives can be computed as follow:

$$
\begin{aligned}
\frac{\partial f}{\partial x}(i,j) &= \frac{f(i+1,j)-f(i-1,j)}{2\Delta x} && (3.75)\\
\frac{\partial f}{\partial x}(i+1,j) &= \frac{f(i+2,j)-f(i,j)}{2\Delta x} && (3.76)\\
\frac{\partial f}{\partial x}(i,j+1) &= \frac{f(i+1,j+1)-f(i-1,j+1)}{2\Delta x} && (3.77)\\
\frac{\partial f}{\partial y}(i,j) &= \frac{f(i,j+1)-f(i,j-1)}{2\Delta y} && (3.78)\\
\frac{\partial f}{\partial y}(i+1,j) &= \frac{f(i+1,j+1)-f(i+1,j-1)}{2\Delta y} && (3.79)\\
\frac{\partial f}{\partial y}(i,j+1) &= \frac{f(i,j+2)-f(i,j)}{2\Delta y} && (3.80)\\
& && (3.81)
\end{aligned}
$$

Eq. 3.75 to Eq. 3.80 are easily modified to compute the derivatives in the (ξ, η,ζ)

space and transfered into the (x,y,z) space. This technique is valid for curved, non-uniform grids. This approach has two major advantages. First, there is no special treatment at the centerline: this method allow large fluxes of mass, momentum and species through the centerline. Second, the time step of the computation can be increased. Nevertheless, interpolation errors (or inaccuracy) can introduce oscillations. Our studies suggest that to avoid these oscillations, the boundary between the two grids should not lie in region of high shear or in regions of high pressure or density spatial gradients.

This approach is well-suited for the $DOE - HAT$ geometry but is not valid for the dump combustor geometry. In the dump combustor simulation, the flame is located at the centerline of the domain, while, in the $DOE - HAT$ combustion chamber geometry, the flame is located far from the centerline. At the flame front, large velocity, temperature and density gradient exists. The interpolation method is able to transfer the information from one grid to the other. However, the interpolated values are not fully accurate and small errors are introduced. These errors introduces imbalance in the energy equation and pressure pulses are created in the region of interpolation. These numerical instabilities (1 in Figure 3.9) produce numerical fluctuations in the momentum and scalar fields and these fields are not suited for interpolation (2 in Figure 3.9). As a result, interpolation errors propagate to the second grid (3 in Figure 3.9) and the cycle continues (4 and 5 in Figure 3.9).

As a results, a new technique was developed. The main goal is, again, to resolve the centerline region using a Cartesian grid and the rest of the domain using a cylindrical grid, such that the circular geometry of the dump combustor can be meshed by the computational grid. The newly developed computational grid is continuous at the interface between both grids and is shown in Figure 3.10. This technique requires some modifications of the $LEMLES$ splicing models when message-passing (MPI) is performed. These adjustments are described in the next paragraph.

In the $LEMLES$ method, the LES mass fluxes are used to splice LEM fields across LES cells. These fluxes are computed in the i-, j- and k-direction. However, these directions change between the Cartesian grid and the cylindrical grid (see Figure 3.11. $F^1_{j,cyl}$, $F^2_{j,cyl}$,

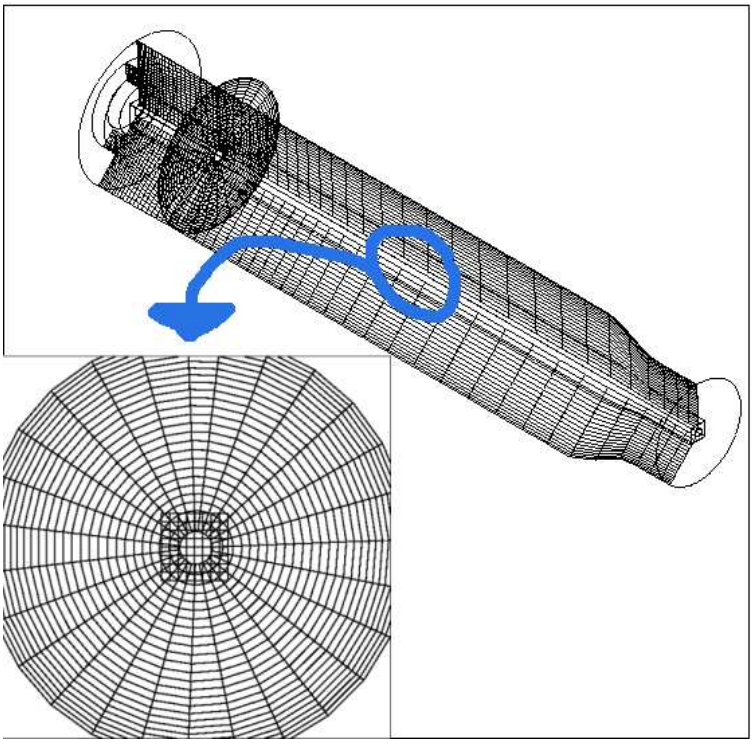

Figure 3.8: Two grids approach. The centerline region is resolved using a Cartesian grid while the rest of the combustion chamber geometry is fitted using a cylindrical grid. Both grids overlap. This grid is used for the $DOE - HAT$ combustor studies.

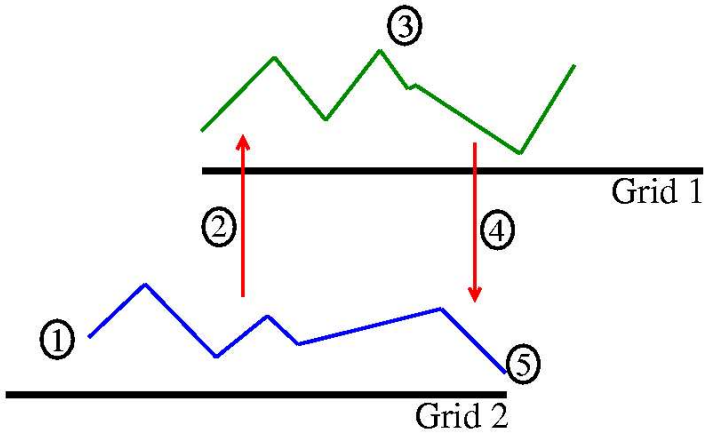

Figure 3.9: Self-sustained oscillations phenomena in the overlapping grids technique.

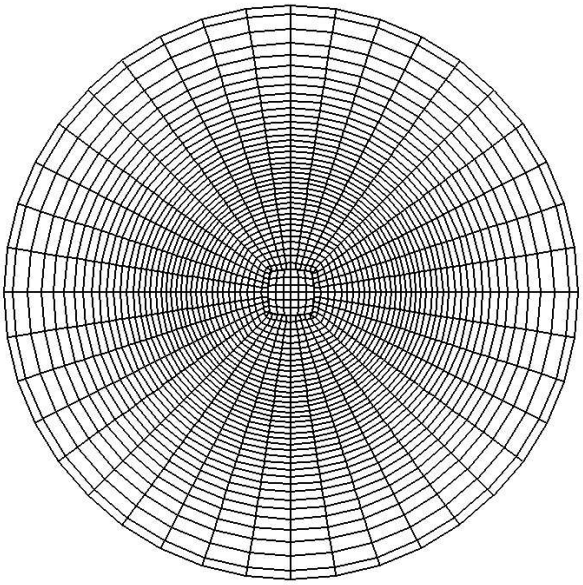

(a) General front view of the 2 grids.

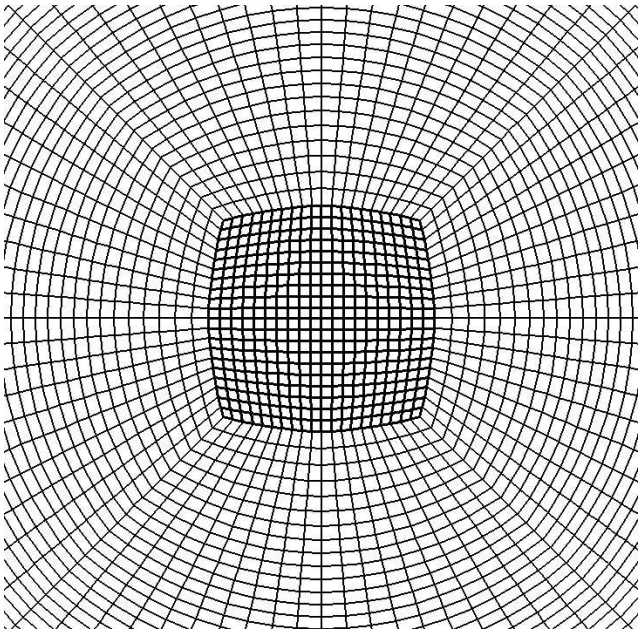

(b) Zoom-in of the centerline region of the front view of the 2 grids.

Figure 3.10: Two grids approach. The centerline region is resolved using a Cartesian grid while the rest of the combustion chamber geometry is fitted using a cylindrical grid. Both grids are continuous. This grid is used for the dump combustor studies.

$F^3_{j,cyl}$ and $F^4_{j,cyl}$ denote the fluxes of mass in the cylindrical grid, in the j-direction for face 1, 2, 3 and 4, respectively. In the same manner, one can denote the other fluxes by: $F^1_{k,cyl}$, $F^2_{k,cyl}$, $F^3_{k,cyl}$, $F^4_{k,cyl}$, $F^1_{j,car}$, $F^2_{j,car}$, $F^3_{j,car}$, $F^4_{j,car}$, $F^1_{k,car}$, $F^2_{k,car}$, $F^3_{k,car}$ and $F^4_{k,car}$.

In order to pass the information from the Cartesian grid to the cylindrical grid (and vice-versa), the following relations must be used:

$$\begin{aligned}
F^1_{j,car} &= F^1_{j,cyl} \\
F^1_{k,car} &= F^1_{k,cyl} \\
F^2_{j,car} &= -F^2_{k,cyl} \\
F^2_{k,car} &= F^2_{j,cyl} \\
F^3_{j,car} &= -F^2_{j,cyl} \\
F^3_{k,car} &= -F^2_{k,cyl} \\
F^2_{j,car} &= F^2_{k,cyl} \\
F^2_{k,car} &= -F^2_{j,cyl}
\end{aligned} \tag{3.82}$$

This work and a study of Patel [2005] demonstrate the validity of this technique.

3.9.2 Resolution of the Turbulent Scales

In this work, no grid dependency study was conducted. However, in the regions where recirculation regions are present, high shear combustion are present, the grid is chosen to resolve into the inertial range length scales since these scales contains the vast majority of the turbulent energy. In region downstream of the flame, the grid resolution is larger to reduce the overall computational cost. The validity of the grid resolution is assessed by studying the spectrum of the turbulent velocity fluctuations in the regions of interest. Such a spectrum is shown in Figure 3.12 for the grid used to mesh the dump combustor geometry. The region were the energy decays following the -5/3 law is large and proves that the inertial range is well-resolved with the computational grid used in this study. Identical

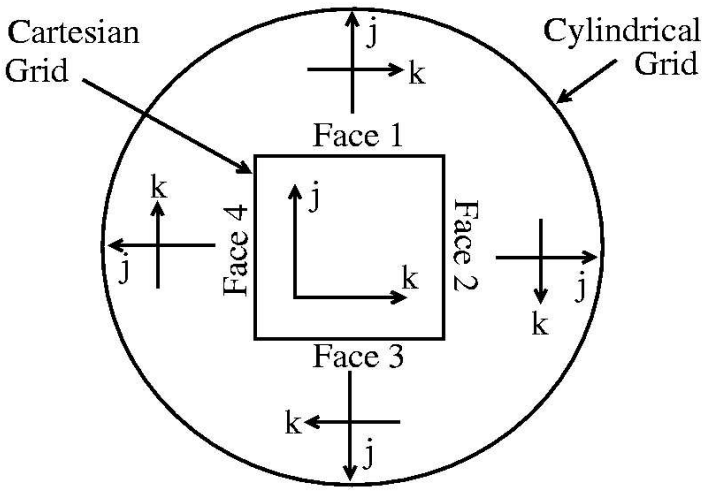

Figure 3.11: Schematic representation of the Cartesian and cylindrical grids in the y-z plane. The computational directions (i and j) are indicate for both grids.

results are obtained when the grid used to mesh the $DOE - HAT$ combustor geometry is studied.

3.9.3 *LES* and *LEM* Resolution

The 3-dimensional *LES* and 1-dimensional *LEM* resolutions can not be arbitrarily chosen. Sec. 3.9.2 explained the link between the resolution of the inertial range and the computational mesh. Therefore, the *LES* resolution is determined by the resolved turbulence of the system. On the other hand, the resolution of the *LEM* computational domain is determined by the *LES*-unresolved turbulence. Sec. 6.4.1 shows how the chosen *LEM* resolution capture the vast majority of the subgrid turbulence. In this section, the results are obtained from the data of the dump combustor study but identical results are obtained when data of the $DOE - HAT$ combustion chamber are studied.

To a lesser extend, the *LES* resolution is a function of the flame thickness. While the flame can be resolved at the *LEM* level, independently of the *LES* resolution, two or three *LES* grid points are needed to resolve the heat release region. In the simulation of flame propagation in combustion chamber, this criteria would lead to extremely large computational grids. Therefore, the flame is always under resolved at the *LES* level (i.e.

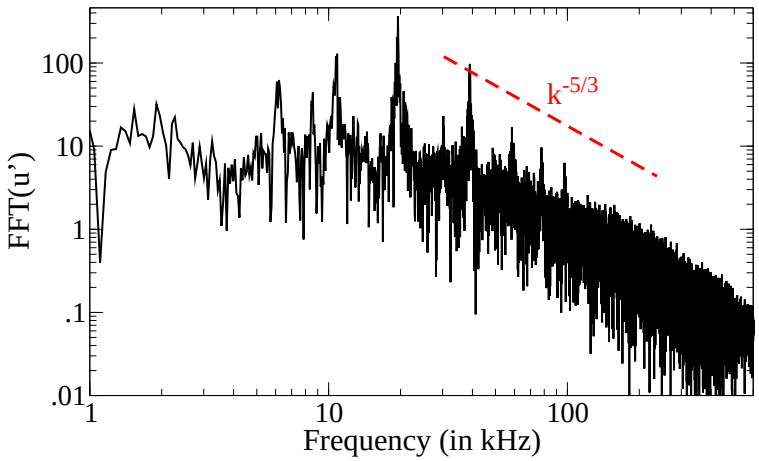

Figure 3.12: Spectrum of the turbulent axial velocity fluctuations for the dump combustion chamber. Data are taken 2 cm downstream of the dump plane, on the product side of the flame. A reference of the -5/3 decay is also shown.

less than one LES cell). If the flame heat release was resolved in only one LES cell, numerical oscillations would be present. In reality, the simulated flame front numerically thickens itself such that the heat release region is resolved by a minimum of two LES cells. In order to limit this numerical thickening of the flame front, it is of critical importance to have a fine grid resolution in the flame region.

CHAPTER IV

POLLUTANT EMISSION

The following chapter presents the pollutant emission prediction obtained for the $DOE-HAT$. Results are compared to experimental data.

4.1 CO Emission Without UHC Oxidation

When only CO formation at the flame front and its oxidation in the post-flame region are considered, the entire amount of CO formed at the flame front is oxidized before reaching the emission probe, and thus, the experimental data trend (see Figure 4.1) is not predicted. This is predicted by both approaches ($GLES$ and $LEMLES$). Typical results are shown in Figure 4.1.

To ensure the correctness of the oxidation rate computation, the values given by the flamelet library are compared to values obtained when the CO oxidation rate is directly computed assuming an Arrhenius law. The CO oxidation reaction is: $CO+OH \leftrightarrow CO_2+H$ and the CO oxidation rate can be expressed as Warnatz [1984]:

$$\frac{d[CO]}{dt} = -k_i[OH]_e\Big(1+\frac{[CO]_e}{[CO_2]_e}\Big)([CO]-[CO]_e) \tag{4.1}$$

where the reaction rate k_i is given by an Arrhenius law k_i=$4400.0T^{1.5}exp(-373/T))$ (units are kmol, m, K and sec). The comparison for different equivalence ratios is given in Table 4.1. Values reported in Table 4.1 are relatively close, thus confirming the correctness of library calculations. Furthermore, Eq. 4.1 predicts an even higher CO oxidation rate for Φ<0.5, thus verifying the conclusion that the CO formed at the flame front is not responsible for the "knee" in the CO emission curve.

4.1.1 Modification of the Turbulent Flame Speed Model

Partial CO oxidation might occur if the residence time in the post-flame region is decreased. The residence time decreases when the flame length increases. In $GLES$, it is possible to

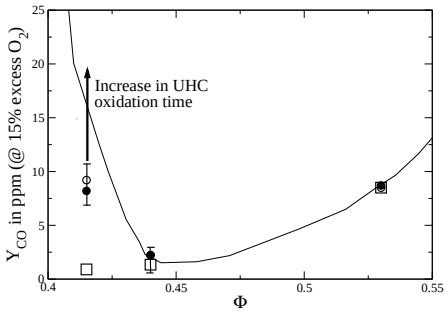

Figure 4.1: Experimental and numerical CO emission for different equivalence ratios (Solid lines: experiments, •: $LEMLES$ with UHC oxidation, ∘: $GLES$ with UHC oxidation, □: $GLES$ without UHC oxidation). The vertical | indicate the level of fluctuations in CO due to combustion dynamics. Fluctuations increase as the equivalence ratio is decreased and LBO is approached.

Table 4.1: Comparison of the CO oxidation computed by the library and by Eq. 4.1.

Φ	$1/\tau_{CO,ox}$ (Eq. 4.1)	$1/\tau_{CO,ox}$ (Library)
0.41	2089	1523
0.43	2853	2215
0.45	3826	3375
0.47	5045	4571
0.49	6539	6426
0.51	8402	8912
0.53	10589	11021

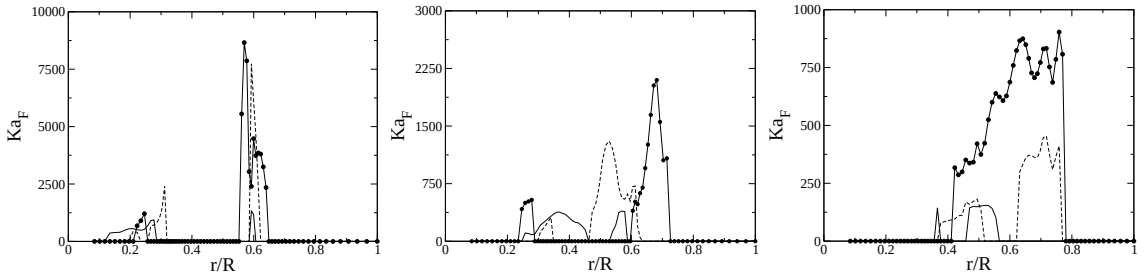

(a) $D = 1.5$ mm (b) $D = 12$ mm (c) $D = 22$ mm

Figure 4.2: Radial profiles of the flame front Karlovitz number Ka_F for different equivalence ratio. Ka_F=KaH where H=1 in the flame region and H=0 otherwise. Legend: –: Φ=0.53, - -: Φ=0.44, -●-: Φ=0.41.

change the effective flame length by modifying the flame speed model. A decrease in β and/or ζ (the upper limit u'/S_L) (see Eq. 2.52) corresponds to a decrease in turbulent flame speed.

The modification of the turbulent flame speed model is motivated by the study of the combustion regime. If, for Φ=0.53, the flame propagates in the corrugated flamelet or the TRZ regime, large portion of the flame propagate in the BRZ regime for Φ=0.41 (see next paragraph). In order to reproduce the "bending" of the turbulent flame speed model in the TRZ and BRZ regime, β and/or ζ can be decreased, hence decreasing the value of S_T for a given value of u'.

To demonstrate the fact that the flame propagates in the BRZ regime for Φ=0.41, the variation of the Karlovitz number at the flame front (Ka_F) for different equivalence ratios is shown in Figure 4.2(a-c) at various axial locations. Ka is large in regions of high turbulence (i.e., shear layers) or when Φ is decreased. For Φ=0.41, Ka_F>>100 in a large portion of the flame.

Different values of β and ζ were tested and the emission results at the emission probe location are summarized in Table 4.2 for an equivalence ratio of 0.41. It can be seen that the CO level can change by nearly a factor of 30 by small changes in the model parameters. This high sensitivity to model parameters suggests a major limitation of the $GLES$ model in the region of current interest.

Table 4.2: Constants used in the turbulent flame speed model 2.52 and related CO emission and flame length.

Case	β	ζ	$\widetilde{Y_{CO}}$ (ppm)	Flame length (cm)
A	20.0	16.56	0.97	1.5
B	10.0	10.00	3.7	3.0
C	7.0	10.00	34.1	10.0

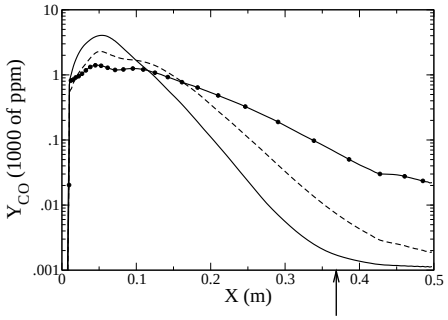

Figure 4.3: Influence of the flame speed model upon the CO mass fraction. X is the distance from the dump plane. Solid line: β=20.0, ζ=16.56, dashed line: β=10.0, ζ=10.0 and dashed-dotted line: β=7.0, ζ=10.0.

As the turbulent flame speed decreases, the flame length increases and the maximum in CO emission also shifts. This is shown in Figure 4.3. Although Case C (Table 4.2) shows good agreement with measurements at the probe location, the actual flame structure is not physical. The flame is too long (see Table 4.2) and the flame thickness is of the order of 1.5 cm, which is unphysical. In Case C, the LES resolved turbulent time scale is much smaller than the flame propagation speed, therefore increasing the flame thickness. Thus, the Case C speed model is not physically viable. Hence, the turbulent flame speed model can not explain the differences between the numerical and experimental CO emission.

4.1.2 Heat Losses

The experimental combustion chamber walls are water cooled, whereas, the numerical setup consider that the walls are adiabatic. Because heat losses may reduce the CO oxidation rate a heat loss model is implemented. The cooling water temperature (T_w) is assumed to be 300K while the wall thickness (δ_w) is assumed to be 1 inch (2.54 cm). This is presented in Figure 4.4.

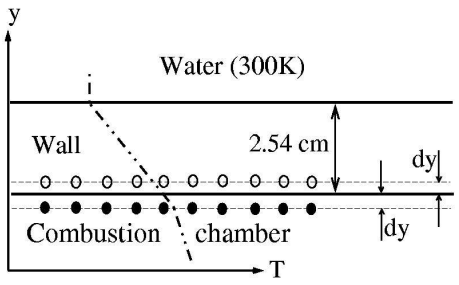

Figure 4.4: Sketch of the geometry of the combustion chamber walls to take into account the heat losses related to the water cooling system. •: computed LES grid points, ∘: boundary grid points.

The temperature of the boundary grid point (T_{GC}) is a function of the computed LES temperature (T_{LES}) and the distance from the wall to the computed LES grid point (dY). T_{GC} is given by:

$$T_{GC} = \Big(\frac{T_{LES} - T_w}{\delta_w + dY}\Big)(\delta_w - dY) + T_w \tag{4.2}$$

Results do not exhibit any change in the CO profile at the emission probe location. The CO oxidation rate is lower in the thermal boundary layer due to the decrease in temperature in region close to the combustion chamber walls. At the same time the residence time increases in the momentum boundary layer. However, the CO oxidation rate decreases in the boundary layer region is an exponential function of temperature while the increase in residence time is a linear function of time and one is not balanced by the other. However, the heat losses modeled in this study are not able to reproduce the experimental CO emission trends.

Another study of the same combustion chamber Cannon et al. [2003] suggests that the CO emission trend is due to the non-uniformity of the incoming mixtures. The idea behind the consideration of a non-uniform inflow mixture fraction profile is the creation of relatively cold post flame region - a direct consequence of regions of low equivalence ratio - that will be characterized by a low CO oxidation rate.

Inflow equivalence ratio profile is plotted in Figure 4.5 (a) and is obtained from experiments. The variation in equivalence ratio is relatively small and agrees with the assumption that the DOE-HAT combustor is operating under nearly perfectly premixed combustion.

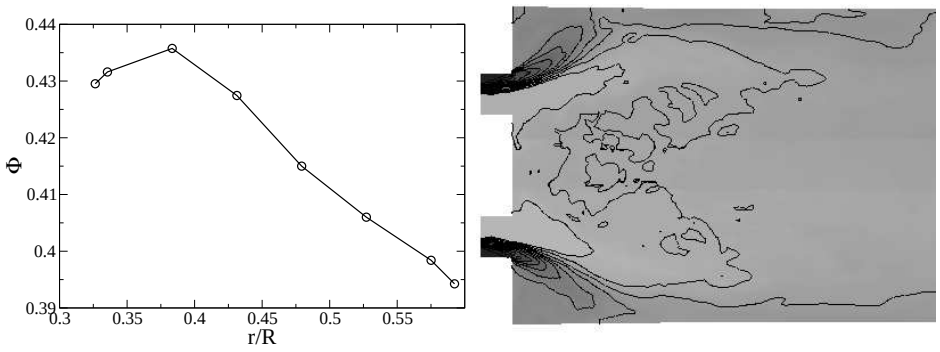

(a) Inflow Φ as a function of the normalized radius ($\overline{\Phi}$=0.415) - Courtesy: UTRC

(b) Time averaged mixture fraction field. Dark colors: leaner than $\overline{\Phi}$, light colors: richer than $\overline{\Phi}$

Figure 4.5: Unmixindness of the inflow mixture. Inflow profile and time averaged $\widetilde{Z}$ field

Figure 4.5 (b) shows the time averaged mixture fraction. Turbulent convection mixes the gases (reactants as well as products) and mixture fraction gradients decrease. At the location of the emission probe, the CO mass fraction reaches its equilibrium value. Therefore, the presence of very lean reactants pockets can not explain the CO emission trend.

4.2 CO Emission With UHC oxidation

As noted earlier, as Φ is decreased and as the LBO limit is approached, local flame quenching can occur and is followed by complete flame extinction when Φ is further lowered. Past studies Held et al. [2001] have shown that UHC is a second source of CO because the UHC released in the post-flame region when the flame front is quenched is oxidized in the post-flame region. For low equivalence ratio (Φ<0.5), the $ITNFS$ model Meneveau and Poinsot [1991] predicts that 2 to 4 percent of the flame surface quenches. Local extinction is predicted at the dump-plane, where turbulence is large.

4.2.1 Mixing Time Scale

In processes like CO or UHC oxidation, a turbulent mixing time scale (t_{mix}) can be defined and a reaction time scale can be taken as as the minimum between the chemical and the mixing time scale. This so-called Eddy-Break Up (EBU) model should not be used in a LES

simulation because of its lack of accuracy: $t_{mix} \propto \Delta / u'$ only gives an order of magnitude of the mixing time scale and is grid size dependent. A very sensitive process like CO oxidation can not tolerate such lack of accuracy. Furthermore, due to the length of the combustion chamber, post-flame region LES cells far from the flame are large enough so that their resolution may not fall into the inertial range, thus no mixing time scale can be defined using inertial range scaling laws. Therefore, it will be assumed that all pollutants formation and destruction rates are chemistry controlled. Computation show that, when t_{mix} can be defined, it is of the order of magnitude of the chemical time scale, thus confirming that no EBU model is required.

4.2.2 Results

Table 4.3 summarizes the two models used in this study for UHC oxidation and the CO emission prediction. The formula used for the oxidation of UHC into CO is:

$$\dot{w} = [UHC] A exp\Big(- \frac{E_A}{T} \Big) \tag{4.3}$$

$\widetilde{Y}_{CO}$ does reach its equilibrium mass fraction if the low UHC oxidation rate is used. If the high UHC oxidation rate is used, the CO mass fraction drops to $Y_{CO,eq}$ right before the location of the emission probe.

Table 4.3: Comparison of CO emission at the location of the emission probe for different UHC oxidation model for Φ=0.41. CO mass fractions are given in ppm @ 15 percent excess O_2. 0.97 ppm corresponds to the value of CO ppm at equilibrium. For Φ=0.41 the ratio between both oxidation rate (for a given [UHC]) is 2.6. The unit of E_A is K^{-1} and the unit of $\widetilde{Y}_{CO}$ is ppm.

Model	A	E_A	$\widetilde{Y}_{CO}$
High oxidation rateHeld et al. [2001]	$6.25 * 10^{16}$	23000	0.97
Low oxidation rateWestbrook and Dryer [1981]	$2.4 * 10^{16}$	26100	8.1

Figure 4.6 demonstrates that UHC is not a negligible source of CO. A large amount of CO formed via UHC oxidation is oxidized early in the post-flame region (X<0.1 m in Figure 4.6, where X is the distance from the dump plane to the downstream point). But the CO released later in the combustion process (through oxidation of unburnt fuel at X>0.15

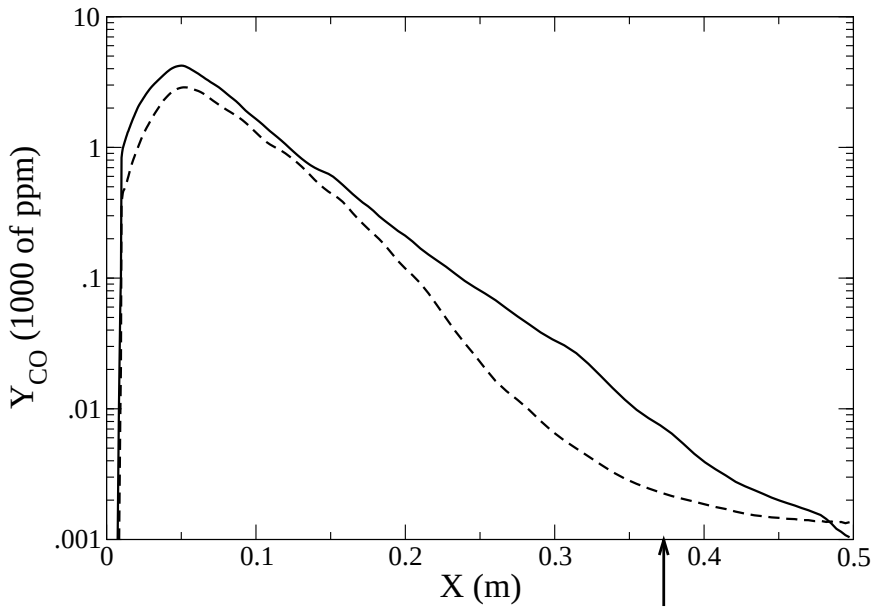

Figure 4.6: Time-averaged CO mass fraction as a function of the distance from the dump plane (X).Solid line: CO emissions with UHC oxidation, dashed line: CO emissions without UHC oxidation. The location of the emission probe is indicated by an arrow.

m in Figure 4.6) does not reach its equilibrium value before the location of the emission probe. This results in a higher CO at the probe location. In this study, all UHC released is oxidized before reaching the emission probe. Furthermore, only the low UHC oxidation rate exhibits significant CO emission at the location of the emission probe.

Analysis of these results suggests that UHC in the post-flame region appears to play a primary role in the exponential increase of CO emission when the equivalence ratio decreases below 0.44. Both UHC oxidation rate models show that the location where $\widetilde{Y}_{CO}$ reaches $Y_{CO,eq}$ is drastically shifted downstream when compared to simulations where UHC is not taken into account. These predictions are very sensitive to the UHC oxidation rate model and global residence time. Therefore, one should only expect to be able to predict the order of magnitude of the CO emission. The fact that the location where $\widetilde{Y}_{CO}$ reaches $Y_{CO,eq}$ is right before the location of the emission probe (high UHC oxidation rate model) or after this location (low UHC oxidation rate model) is not of crucial importance. The general inaccuracies of the models related to CO and UHC formation and consumption only affect the exact location where $\widetilde{Y}_{CO}$=$Y_{CO,eq}$.

Therefore, as a conclusion, one can only emphasize the fact that the prediction of the experimental data can only be achieved if UHC is taken into account and that the model's inaccuracy for low equivalence ratio does not allow us to predict the exact amount of CO emission. However, for large equivalence ration (Φ>0.44), the amount of CO emission is equal to the amount of CO at equilibrium and, for these higher values of Φ, the emission trend can be determined by simply using data obtained from the CHEMKIN program. This last point is only valid for the $DOE - HAT$ combustor.

4.3 NO_x Emission

NO_x emission prediction for the entire range of Φ of interest is shown in Figure 4.7. Results are similar for both $GLES$ and $LEMLES$ approach: the flame surface and product temperature predicted by both models are similar, thus the level of CO is identical for both model (this is in agreement with the observations made for the CO emission, where the two models yields the same amount of emission of CO). Unlike CO, NO_x prediction is in good agreement with experiments for low equivalence ratio but is under-predicted when Φ increases. Post-flame NO_x production is responsible for the largest portion of NO_x emission for $\Phi>$ 0.5 (adiabatic flame temperatur lower than 1500K). This is shown in Figure 4.8. For Φ=0.41, the mass fraction of NO_x is constant in the post-flame region while $\widetilde{Y}_{NO}$ is increasing in the post flame region for Φ=0.53. Numerical results compare well with experimental results for the lower equivalence ratio (Φ=0.41), when post-flame NO formation is negligible. Therefore, the divergence between numerical and experimental results for larger Φ may be explained by the fact that the NO_x formation in the post-flame region is under-predicted in this study. Furthermore, temperature fluctuations, poor macroscopic fuel mixindness and super-equilibrium radicals influence upon NO formation Fric [1993] have been neglected and both of these effects largely affect the formation of NO in the post-flame zone.

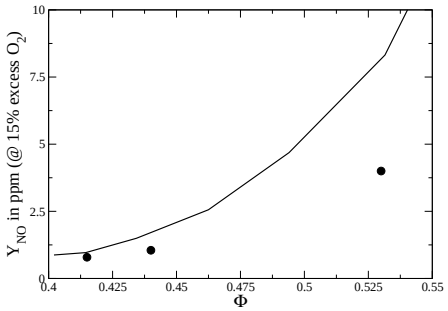

Figure 4.7: Experimental and numerical NO emission for different equivalence ratio (Solid line: experiments, •: $LEMLES$ as well as $GLES$).

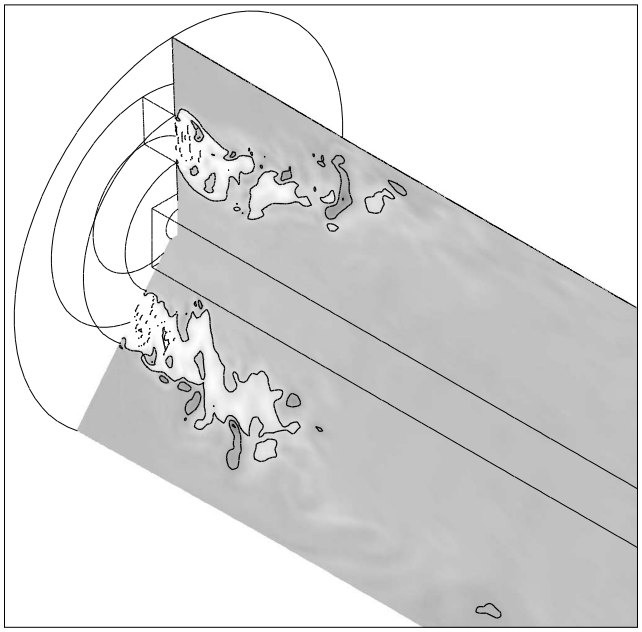

(a) Φ=0.41 - White = 0 ppm, Black = 6 ppm

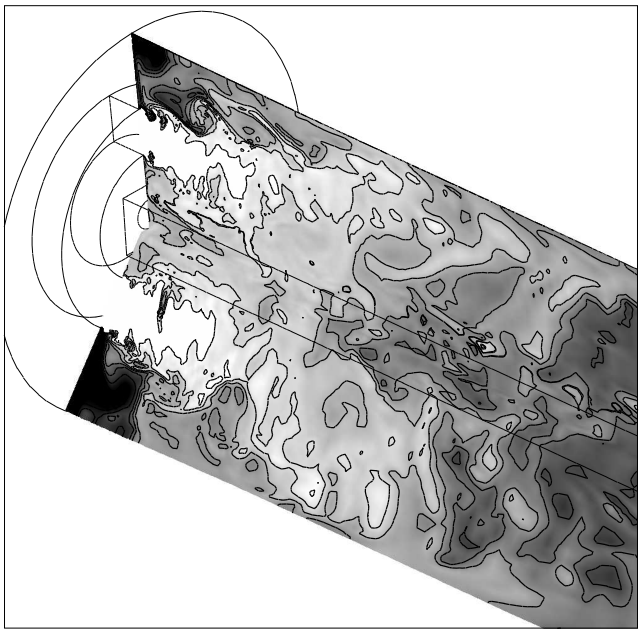

(b) Φ=0.53 - White = 4 ppm, Black = 11 ppm

Figure 4.8: Instantaneous NO mass fraction field for the $DOE-HAT$ combustion chamber. Large amount of NO is produced in the post-flame region for Φ=0.53 while, for Φ=0.41, the entire amount of NO is produced at the flame front.

CHAPTER V

COMPARISON OF *GLES* AND *LEMLES*

In this chapter, the *GLES* approach is compared to the *LEMLES* approach. Both models are compared for premixed turbulent combustion regimes and an explanation for the limitations of the *GLES* and of the *LEMLES* model is proposed.

In the first section, flame propagation in an isotropic turbulent field is studied. In the second section, the propagation speeds of flames simulated using the *GLES* and the *LEMLES* model are compared. In the third section, the limitations of the *GLES* model are presented. In the last section, the limitations of the *LEMLES* model are presented.

5.1 Flame Propagation in an Isotropic Turbulent Field

To evaluate the behavior of the two approaches, we first simulate flame propagation in an isotropic field using the *GLES* and the *LEMLES* models. The general setup is similar to the approach used in past studies Smith and Menon [1996b] except that, here, we choose conditions such that the Karlovitz number is of the order of 100, which is in the $TRZ-BRZ$ borderline regime (See Figure 1.1). Inflow isotropic turbulence of a level sufficient to mimic conditions in the $TRZ-BRZ$ regime is introduced in the inflow. A uniform grid of 64 x 64 x 64 is employed to resolve a domain of 1.5 cm x 1.5 cm x 1.5 cm. For *LEMLES*, 12 *LEM* cells are used in each *LES* cell and the 1-step, 1-step finite-rate kinetics for methane-air combustion is employed. The equivalence ratio is 0.44.

Instantaneous fuel contours are shown in Figure 5.1 (a) and Figure 5.1 (b) for *GLES* and *LEMLES*, respectively. The *GLES* flow field is more homogeneous than the *LEMLES* field. This is due to the limitation of the flame speed model since, in an extreme level of turbulence, u'/S_L>16.56 (which corresponds to the maximum u'/S_L allowed Kim and Menon [2000]) , hence, the turbulent flame speed is a constant for high values of u'/S_L. As a result, the flame thickness is approximately constant. Note that, if this constraint is

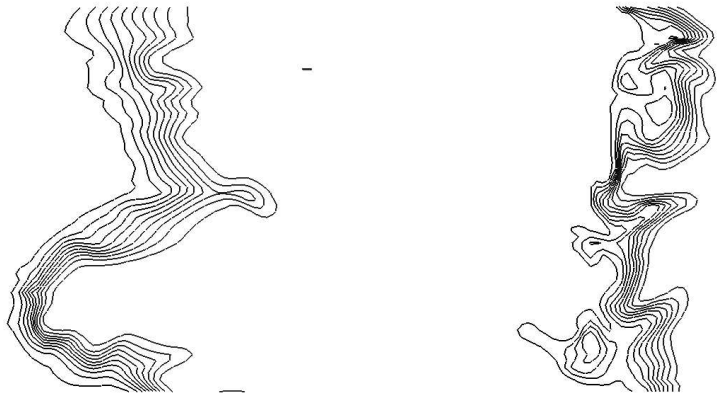

(a) GLES (b) LEMLES

Figure 5.1: Instantaneous snapshots of the premixed flame front in a turbulent medium. Ka is of the order of magnitude of 100. For $GLES$, $S_T{=}S_L\Big[1+20(u'/S_L)^2\Big]^{1/2}$ where $(u'/S_L)_{max}$=16.56. This maximum is reached in the vast majority of the flame region, therefore $S_T{=}S_T(S_L,u')$ is a constant.

relaxed, flame propagation will rapidly increase (in the current $Ka=100$ case, u'/S_L>25.0) but this will not be physical. This is an inherent limitation of the flame speed model used in the $GLES$ approach. In the $LEMLES$ approach, the flame is resolved at the LEM level and therefore, is independent of the LES resolution. Furthermore, since there is no flame speed model, no specific constraint is needed. Flame propagation is the result of subgrid burning, heat release, volumetric expansion and large-scale advection. As shown in Figure 5.1 (b), the flame structure exhibits much more spatial variability unlike in the $GLES$ case. The overall consumption rate of the reactant is similar but no direct comparison is carried out since there is no data to validate either of the two models in the BRZ regime.

5.2 Flame Propagation in Full-Scale Combustion Chambers

5.2.1 Flame Propagation Speed

Average flame shape obtained by the $GLES$ and $LEMLES$ method using the $DOE-HAT$ combustion chamber and the dump combustion chamber are compared. Results for the $DOE-HAT$ combustor are shown on Table 5.1 and results for the dump combustor are

shown on Table 5.2. Flame lengths are computed using time-averaged fuel mass fratcion field. Flame legths are measured from the dump plane to the most dowstream point when the fuel is half burnt, i.e. Y_{CH_4}=$Y_{CH_4,unburnt}/2$.

Table 5.1: Comparison of the flame lengths for the $DOE - HAT$ combustion chamber for different equivalence ratio. Length are given in centimeters and are measured from the dump plane.

Φ	$GLES$	$LEMLES$
0.53	1.5	3.5
0.45	3.0	6.5
0.51	3.5	7.5

Table 5.2: Comparison of the flame lengths for the dump combustion chamber for different equivalence ratio. Length are given in centimeters and are measured from the dump plane.

Φ	$GLES$	$LEMLES$
1.0	2.5	2.2
0.45	4.0	6.0

Results show that the flame lengths obtained via the use of the different models vary greatly. The results presented in Table 5.2 suggest that, for an equivalence ratio close to unity, the flame length obtained when the $LEMLES$ model is used is the same as the flame length obtained when the $GLES$ model is used. For an equivalence ratio close to the LBO limit, the flame obtained when the $LEMLES$ model is used is longer than the flame obtained when the $GLES$ model is used. These results are further analyzed in the next section.

5.2.2 Analysis of the Dump Combustor Flame Behavior

The incoming flow being highly swirling, a tulip-like shape flame is expected. The different flame shapes obtained for the dump combustion chamber are compared in Figure 5.2.

For Φ=1.0, the time-averaged flame surfaces are similar in shape and length. However, this is not the case for Φ=0.45. Two reasons can explain this observation; either the position of the $LEMLES$ flame is less stable than the $GLES$ flame and the time averaging

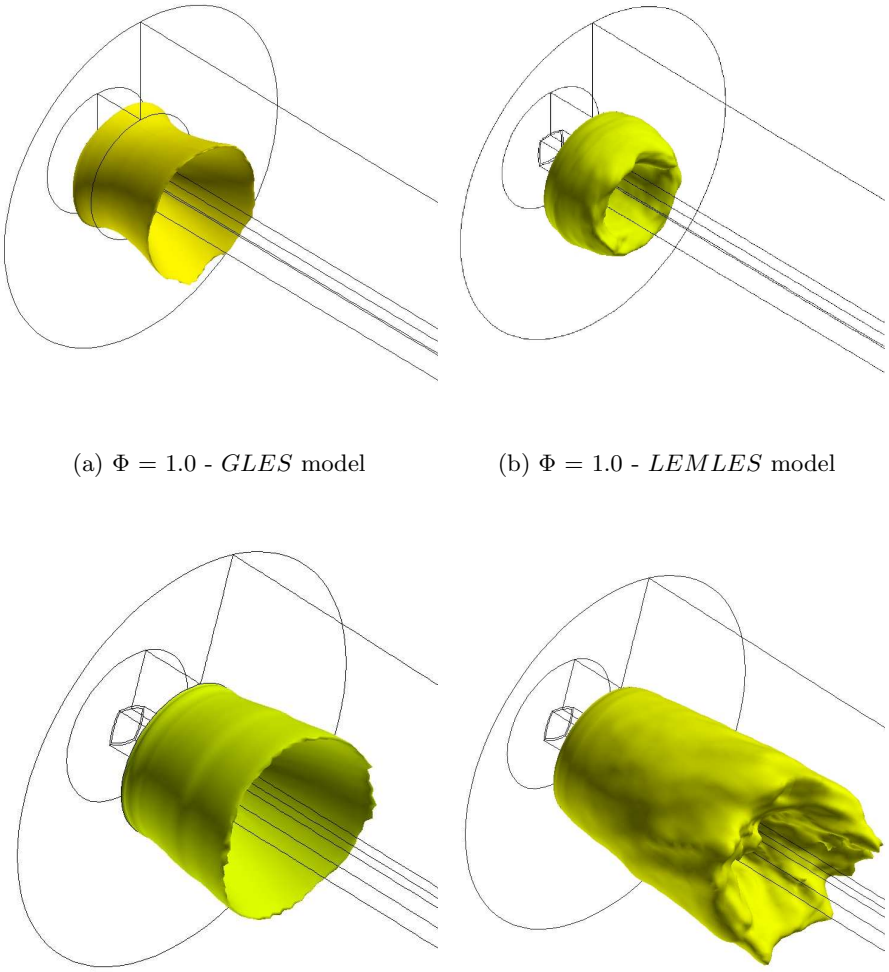

(a) $\Phi = 1.0$ - $GLES$ model

(b) $\Phi = 1.0$ - $LEMLES$ model

(c) $\Phi = 0.45$ - $GLES$ model

(d) $\Phi = 0.45$ - $LEMLES$ model

Figure 5.2: Time-averaged fuel mass fraction. Iso-surface defined as Y_{CH_4}=$Y_{CH_4,unburnt}/2$.

process yields a different flame shape, or the instantaneous $LEMLES$ and $GLES$ flame have drastically different shapes. This question can be answered by analyzing Figure 5.3 which shows instantaneous fuel mass fraction fields for Φ=0.45. The instantaneous shape of both flame is very different and explains the differences observed between Figure 5.2 (c) and 5.2 (d). Both flames being stabilized in the centerline region by the recirculation bubble (vortex breakdown), the location of this structure may explain the difference in flame shape and length.

Instantaneous and non-dimenzionalized centerline axial velocity and fuel mass fraction are plotted for both the $GLES$ model (Figure 5.4) and the $LEMLES$ model (Figure 5.5). The results are very different. For the $GLES$ simulation, the flame at the centerline region is located close to the dump plane and is anchored by a strong recirculation region (see the zoom-in of Figure 5.4). For the $LEMLES$ model, two vortex breakdowns are present. The first one is located inside the reactant region and the leading 'edge' of the second recirculation region anchors the flame. The recirculation bubble is divided in two due to the presence of the flame front. Strong swirl creates a vortex breakdown on the reactant side. The flame propagation speed is too low for the flame to be anchored at the leading edge of this recirculation region. The flame is stabilized downstream of this first recirculation region and, because of thermal expansion, the centerline velocity becomes positive. However, at the flame location, the swirl is still large enough to create a second recirculation zone. This latter vortex breakdown structure and the flame interact such that the flame is stabilized by the presence of the second recirculation zone.

This process is clearly visible when the transition from the $GLES$ to the $LEMLES$ model is studied. Figure 5.6 shows the transition from the $GLES$ flame structure (used as $LEMLES$ simulation initial conditions) to the $LEMLES$ flame structure. The flame propagation speed is lower when the $LEMLES$ model is used and reactants are entrained upstream by the vortex breakdown. Equilibrium is reached once the two recirculation regions are present (t $>$ 35 ms).

However, when time-averaged data are analyzed, only one central recirculation zone is present and anchors the flame. The presence of two instantaneous recirculation regions

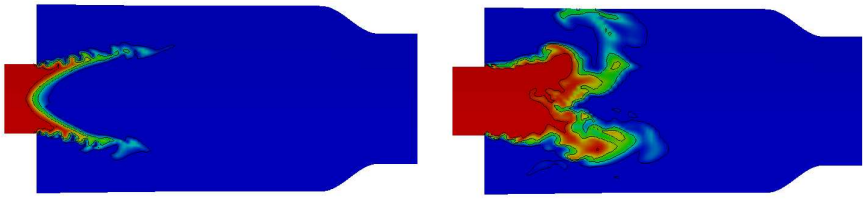

(a) *GLES* model (b) *LEMLES* model

Figure 5.3: Instantaneous fuel mass fraction for the *GLES* and *LEMLES* model for Case 2 (Φ=0.45). Red: Y_{CH_4} is equal to the unburnt fuel mass fraction - Blue: Y_{CH_4}=0.

may be a transient phenomena between the initial *GLES* field and the *LEMLES* field. Unfortunately, the computation was not performed over a time span long enough to test this hypothesis.

5.2.3 Limitation of the *GLES* model

According to the results presented above, the flame speed obtained via the *GLES* model is larger than the flame speed obtained when the *LEMLES* model is used. The explanation of this phenomena can be found in the *G*-equation turbulent flame speed (S_T) formula. As a reminder:

$$S_T = S_L\Big[1+\beta\Big(\frac{u'}{S_L}^{\gamma}\Big)\Big]^{\frac{1}{\gamma}} \tag{5.1}$$

where β and γ are usually set as 20 and 2, respectively. There is a limit on u'/S_L that is set to 16.56.

The following paragraphs focus on this limit. Figure 5.7 shows the maximum u' allowable before the limit on u'/S_L is reached as a function of the equivalence ratio. The lower the laminar flame speed, the lower the maximum value of u' before reaching the maximum value of u'/S_L. A typical distribution of u' inside the combustion chamber is computed as:

$$u' = \sqrt{\frac{2}{3}k^{sgs}} \tag{5.2}$$

and is shown in Figure 5.8. Using this information, the fraction of the combustion chamber where the limit of u'/S_L is reached is plotted on Figure 5.9. This figures shows that the limit of u'/S_L is never reached for Φ>0.7. The limit is only reached in 5% of the domain

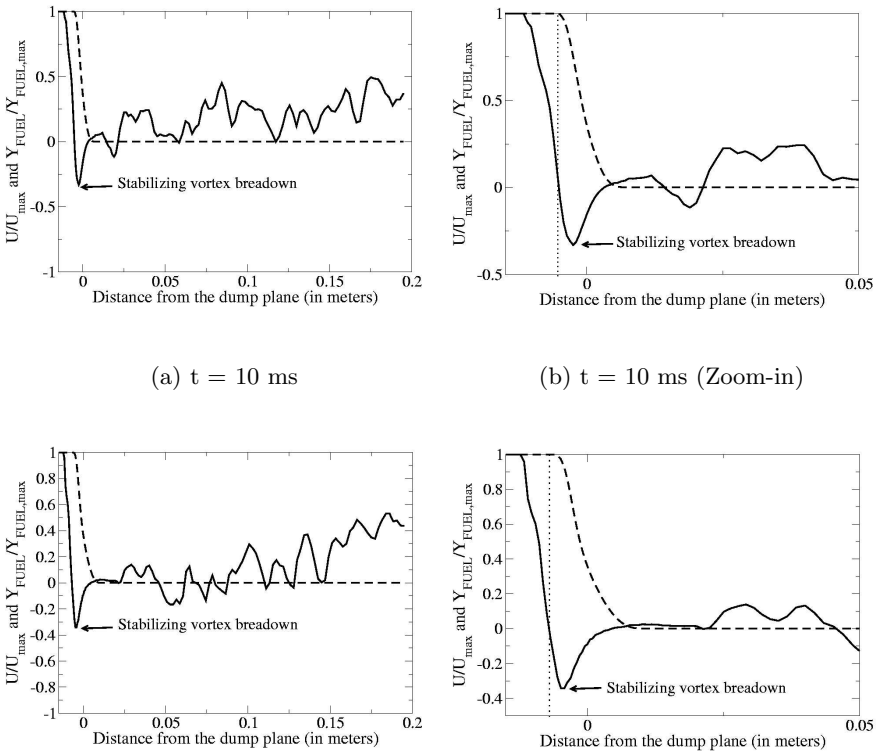

(a) t = 10 ms

(b) t = 10 ms (Zoom-in)

(c) t = 15 ms

(d) t = 15 ms (Zoom-in)

Figure 5.4: Instantaneous non-dimenzionalized centerline axial velocity (solid line) and fuel mass fraction (dashed line) - *GLES* Model - Case 2.

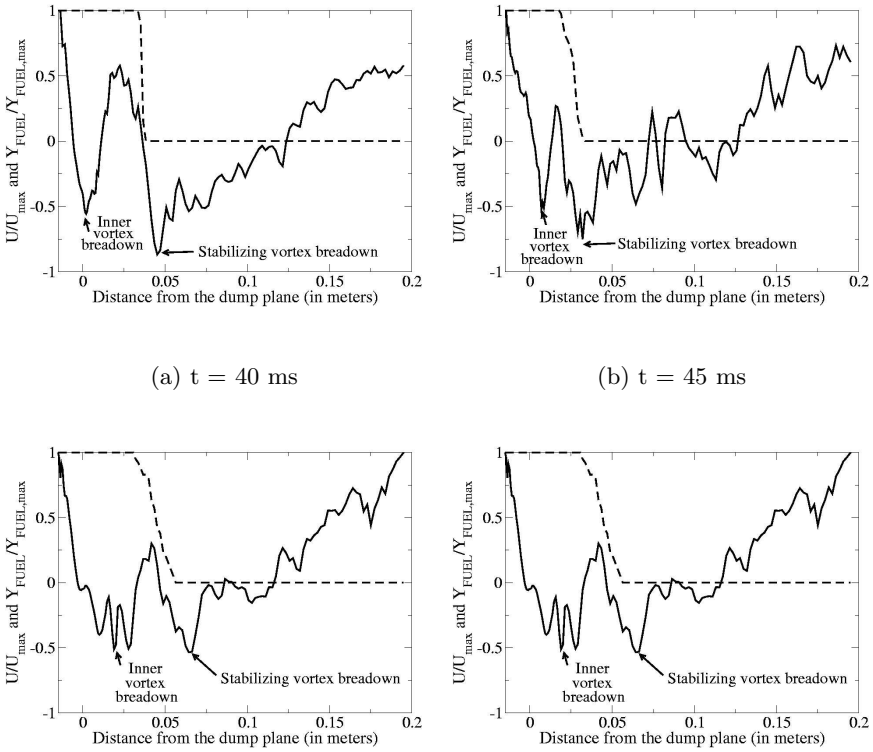

(a) t = 40 ms

(b) t = 45 ms

(c) t = 50 ms

(d) t = 55 ms

Figure 5.5: Instantaneous non-dimenzionalized centerline axial velocity (solid line) and fuel mass fraction (dashed line) - *LEMLES* Model - Case 2.

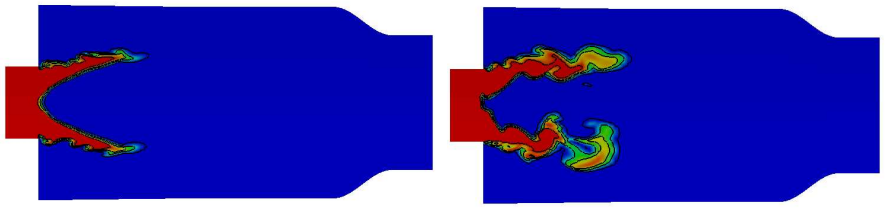

(a) t = 15 ms

(b) t = 20 ms

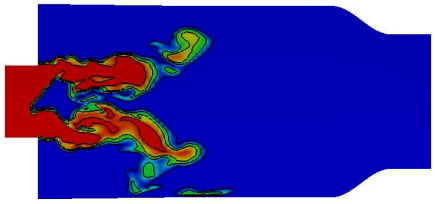

(c) t = 25 ms

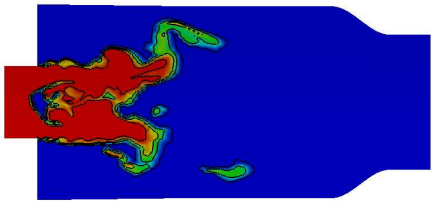

(d) t = 30 ms

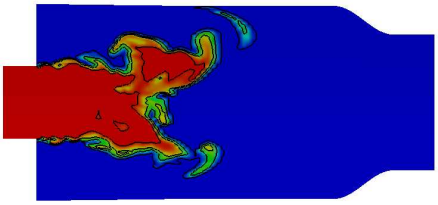

(e) t = 35 ms

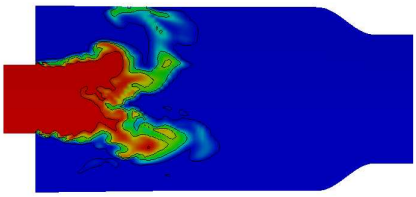

(f) t = 45 ms

Figure 5.6: Instantaneous fuel mass fraction - *LEMLES* model - Case 2. The initial conditions for this simulation are provided by simulations carried out with the *GLES* model.

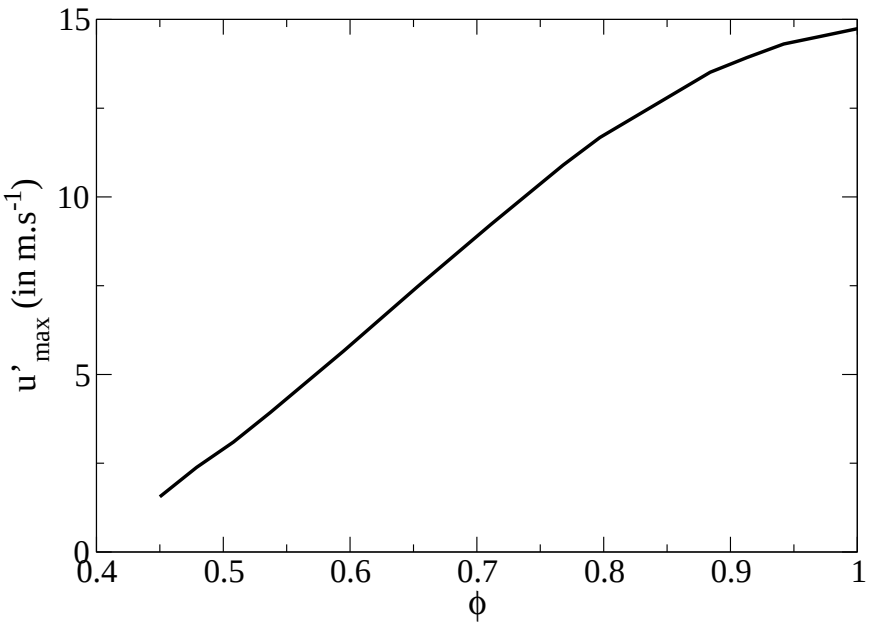

Figure 5.7: Maximum u' allowable in order to have u'/S_L<16.56. This limit is a function of S_L and S_L is given for an inflow pressure and temperature of 6 atm and 644 K, respectively.

for 0.6<Φ<0.7. For Φ<0.6, the portion of the domain where the limit of u'/S_L is reached increases dramatically to reach 84% for Φ=0.45. For high equivalence ratio (Φ>0.7), the flame propagates in the corrugated flamelet regime and Eq. 5.1 is valid. For 0.6<Φ<0.7, the flame propagates in the TRZ regime and, as proved in different other studies Kim and Menon [2000], Eq. 5.1 is still valid. However, as the combustion regime of the premixed flame moves from the TRZ to the BRZ regime, Eq. 5.1 fails and S_T is a constant defined as:

$$S_T = S_L\Big[1 + \beta(16.56)^{\gamma}\Big)\Big]^{\frac{1}{\gamma}} \tag{5.3}$$

The problem lies in the fact that Eq. 5.1 ignores the turbulent flame speed "bending" phenomenon Peters [2000]. For large value of u'/S_L, the turbulent flame speed decreases.

The difference between $GLES$ and $LEMLES$ results is due to a difference in flame propagation speed. As explained above, the turbulent flame speed is over-estimated in the $GLES$ model. Further explanations are given in the next section.

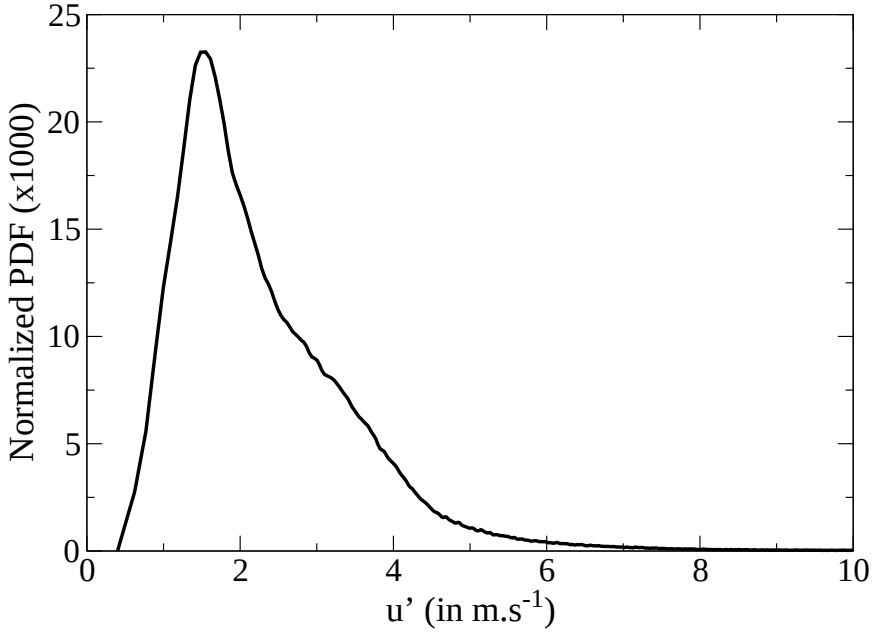

Figure 5.8: Probability density function of u' in the dump combustion chamber. Data obtained from case 2. The equivalence ratio only slightly perturbs the behavior of u' hence, u' data collected for Φ=0.45 are valid for all Φ.

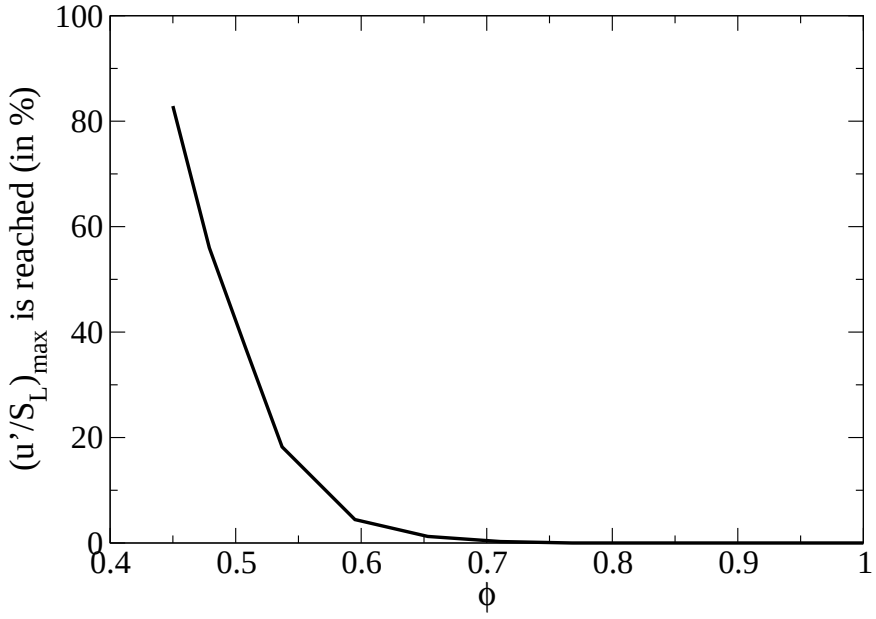

Figure 5.9: Fraction of the *LES* cells in the domain where the limit of u'/S_L=16.56 is reached. Case 2.

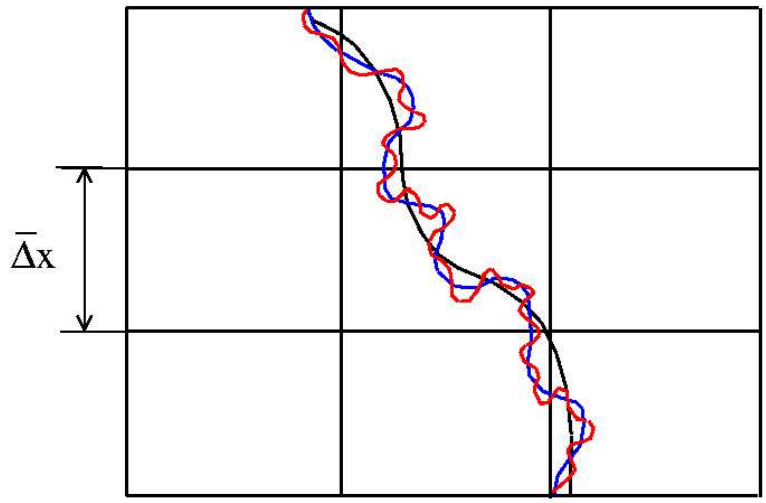

Figure 5.10: Schematic of the LES grid (the grid spacing is $\overline{\Delta}$) and the flamelet for Φ close to unity. The LES resolved flame is shown in black. Unresolved LES turbulent structures increase the flame surface (blue line). Subgrid turbulent structures also increase the flame surface (red line).

5.2.4 Limitations of the $GLES$ Model

The $GLES$ model employed in this study is based on the flamelet approach, where the flame front is considered as an $infinitesimally$ thin surface dividing reactants and products. The flame surface is considered as a succession of laminar flame element, therefore, the local flame propagation speed is S_L. In the LES context, the flame surface is wrinkled by subgrid eddies as well as by unresolved LES eddies (four LES cells are required to resolve an eddy; all eddies smaller than $4\overline{\Delta}$ are not resolved and their influence has to be modeled). This leads to the use of the turbulent flame speed (S_T) model, which takes into account the unresolved increase of the flame surface by increasing the flame propagation speed. Typically, this can be summarized as shown in Figure 5.10.

However, as the equivalence ratio becomes lower, the flame can not be considered as an $infinitesimally$ thin surface anymore. The following relation gives the order of magnitude of the flame thickness δ_F:

$$\delta_F \approx \frac{1}{S_L} \tag{5.4}$$

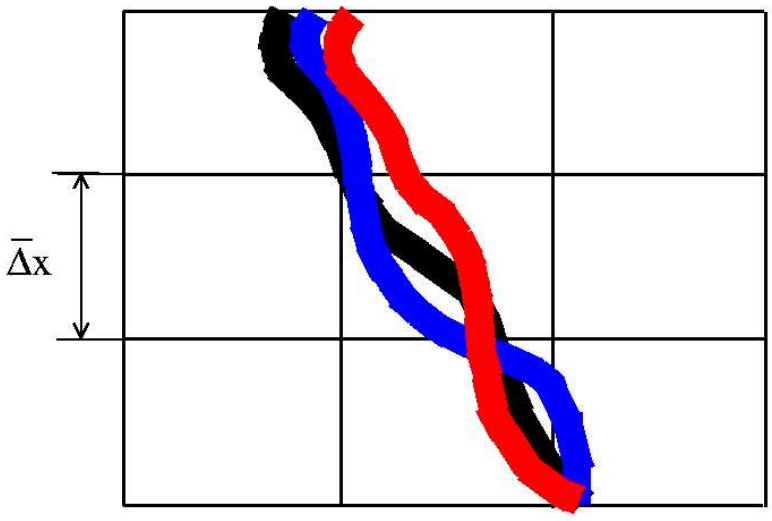

Figure 5.11: Schematic of the LES grid (the grid spacing is $\overline{\Delta}$) and the flamelet for low values of Φ. The LES resolved flame is shown in black. Unresolved LES turbulent structures increase the flame surface (blue line). Subgrid turbulent structures also increase the flame surface (red line).

Comparing the flame thickness for Φ=1.0 and Φ=0.45, leads to:

$$\frac{\delta_F(\Phi = 0.45)}{\delta_F(\Phi = 1.0)} = \frac{S_L(\Phi = 1.0)}{S_L(\Phi = 0.45)} = \frac{89.0}{9.4} = 9.46 \tag{5.5}$$

The flame thickness close to LBO is ten times larger than the flame thickness for an equivalence ratio of unity. For very low equivalence ratios, the schematic of Figure 5.10 is not valid and a valid schematic of the flame behavior in the LES context is presented in Figure 5.11. When the flame thickness is too large, the subgrid eddies do not increase the flame area, they broaden the flame thickness, via a broadening of the flame preheat zone. Therefore, the calibration of the turbulent flame speed model is not valid and leads to an over-prediction of the actual flame propagation speed.

Kim and Menon [2000] proposed a turbulent flame speed model that is valid in the TRZ regime. The idea is to correct the laminar flame speed S_L and consider a laminar flame speed S_L^* that represents the flame propagation speed in the TRZ regime. Kim notes that turbulent structures that can penetrate the flame front *broaden* and *accelerate* the flame (S_L^*>S_L). However, if the local flame front propagation speed is larger than a laminar flame, the overall turbulent propagation speed is lower. This phenomenon is known as the

turbulent flame speed bending phenomenon Peters [1999]. In his model, Kim defines S_L^* and u'^*. u'^* represents the actual level of turbulence that is able to wrinkle the broadened flame ($u'^*<u'$). The turbulent flame speed model valid in this regime is:

$$S_T = S_L^* \Big[1 + \beta \Big(\frac{{u'^*}^\gamma}{S_L^*} \Big) \Big]^{\frac{1}{\gamma}} \tag{5.6}$$

where the constant β and γ are the same as the one taken for Eq. 5.1. In the TRZ regime, $S_L^*>S_L$ but $u'^*<u'$. Because the turbulent flame speed 'bends' in the TRZ regime, the following relation can be deduced:

$$S_L^*(S_L,u') \Big[1 + \beta \Big(\frac{u'^*(S_L,u')^\gamma}{S_L^*(S_L,u')} \Big) \Big]^{\frac{1}{\gamma}} < S_L \Big[1 + \beta \Big(\frac{u'}{S_L} \Big)^\gamma \Big]^{\frac{1}{\gamma}} \tag{5.7}$$

If the Kolmogorov scale is smaller than the flame thickness, the flame propagates in the BRZ regime and Eq. 5.6 is not valid anymore. The limit can be determined by using the following formula Kim and Menon [2000]:

$$\frac{u'}{S_L} = 2.33 Re_\Delta^{1/4} \tag{5.8}$$

where Re_Δ is the subgrid Reynolds number defined as:

$$Re_\Delta = \frac{u'\overline{\Delta}}{\nu} \tag{5.9}$$

If u'/S_L is larger than $2.33Re_\Delta^{1/4}$, Eq. 5.6 is not valid and Kim and Menon [2000] suggests that the flame breaks up and quenches partially or completely. The acceptable (i.e. Eq. 5.6 is valid) laminar flame speed is determined using the distribution of u' inside the domain (see Figure 5.8). Results are presented in Figure 5.12. This figure shows that, for Φ=0.45, the maximum u' that is allowable for $S_L(\Phi=0.45)$=9.4 cm.s^{-1} is u'=0.9. In the computational domain, the vast majority (>97%) of the value of u' is larger than this limit, therefore Eq. 5.6 is not valid for case 2 (Φ=0.45).

This demonstrates that, for a low value of the equivalence ratio, no flamelet model is valid and the $LEMLES$ model has to be employed. This latter model is valid in all premixed turbulent combustion regimes but in the extreme case of a laminar flame. This is discussed in the next section.

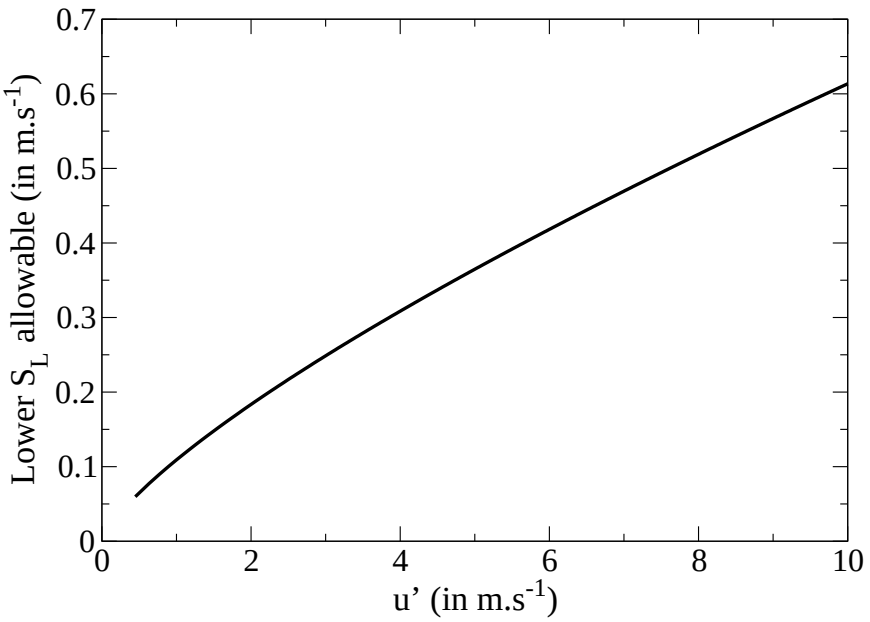

Figure 5.12: Minimum value of S_L allowable to use the TRZ turbulent flame speed for Φ=0.45 (see. Eq. 5.6).

5.2.5 Limitations of the $LEMLES$ Model.

While the $GLES$ model is not valid for large Karlovitz numbers, the $LEMLES$ model fails in regime of low turbulence (Ka<<1). In the $LEMLES$ formulation, species diffusion is performed at the LEM level (i.e. on the LEM domain) while species convection is performed at the LES level. Because the LEM domains are independent of each others, molecular diffusion is not performed between LEM domains located in different LES cells. In premixed combustion, diffusion of heat and radicals ahead of the flame front is responsible for flame diffusion. In a laminar sense, because there is no inter-LES molecular diffusion of species and temperature, the flame cannot propagate from one LES cell to the other. This is clearly shown in Figure 5.13. The propagation of a laminar 1-dimensional premixed flame is simulated using the $LEMLES$ approach. Figure 5.13 (a) clearly shows that the flame does not propagate and that its structure is strongly perturbed because molecular diffusion is not performed between LEM domains, i.e. the discontinuities in the graph correspond to the boundaries of the LES cells.

As discussed in section 2.2.3.1, the regridding process at the LEM level acts as gradient

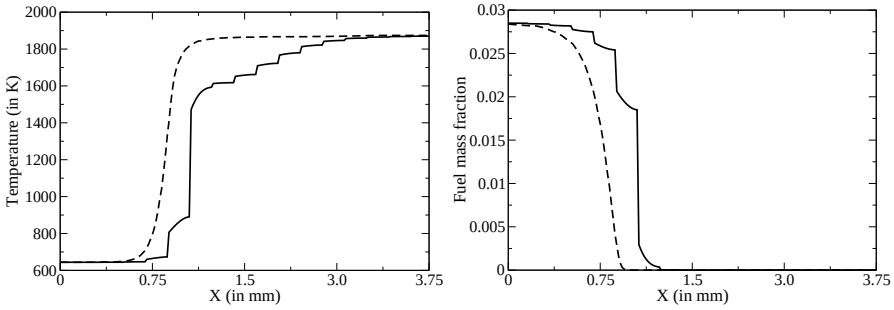

(a) Temperature profile (b) Fuel mass fraction profile

Figure 5.13: $1-D$ flame premixed flame diffusion - $LEMLES$ model (solid lines: initial temperature and fuel mass fraction field - dashed lines: temperature and fuel mass fraction field after 1 ms). The incoming velocity is lower than the theoretical S_L. However, the flame does not propagate and its structure is strongly modified.

smoothing, i.e. it mimics molecular diffusion processes. The evaluation of this gradient smoothing is of great importance. Initial LEM fields (Y_i^0), LEM fields after molecular diffusion (Y_i^I) and LEM fields after splicing and regridding (Y_i^F) are recorded. The molecular diffusion (DY_{mol}) is compared to the total diffusion (DY_{tot}) and are defined as:

$$DY_{mol} = \frac{Y_{i+1}^I - Y_i^I}{Y_{i+1}^0 - Y_i^0} \tag{5.10}$$

$$DY_{tot} = \frac{Y_{i+1}^F - Y_i^F}{Y_{i+1}^0 - Y_i^0} \tag{5.11}$$

The ratio DY_{mol}/DY_{tot} for a typical LEM domain located in the flame zone is shown in Figure 5.14 (result given in percentage). The first and last LEM computational points are not shown because they are affected by the splicing processes. The inner points are not. The figure shows that, on average, only 25% of the total diffusion is a result of molecular diffusion. 75% of the total diffusion is due to gradient smoothing. Hence, the molecular diffusion, even if extremely carefully computed, is not of great importance.

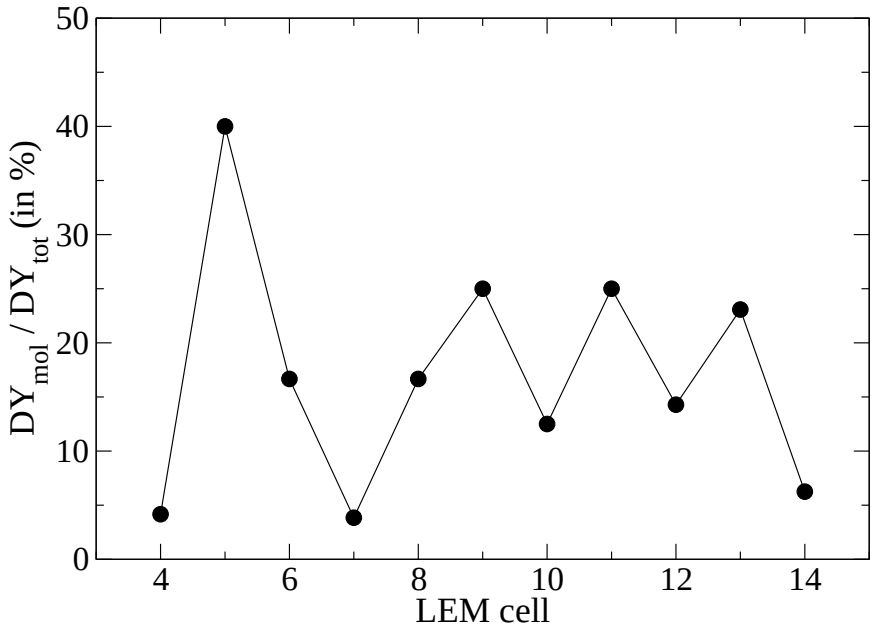

Figure 5.14: DY_{mol}/DY_{tot} for the inner points of a LEM domain. This data is typical for all LEM domains located in the flame zone.

CHAPTER VI

SYSTEMS WITH UNIFORM INFLOW CONDITIONS

In the last chapters, we focus on flame extinction due to turbulence and on flame propagation under different inflow conditions. This chapter focuses on uniform inflow conditions while the next chapter focuses on non-uniform (both in time and space) inflow conditions. This chapter presents results for case 1 and 2 (see sec. 3.8.2). In the BRZ regime, turbulent structures are smaller than the flame reaction zone and are able to break-up the reaction zone structure and quench the flame front. This phenomena is a theoretical concept, i.e. it has not been directly observed in experiences. A large number of numerical and experimental studies focuses on flame extinction via flame stretching. In these studies, stretching is caused by an eddy much larger than the flame thickness and flame extinction depends upon the flame Lewis number. In experimental studies, where flame extinction, or more generally flame lift-off, has been observed, no single cause was identified. Flame lift-off is caused by heat losses, turbulence, non-homogeneous inflow equivalence ratio, etc.

6.1 Preamble

In this first section, the post-processing of $LEMLES$ data is discussed. There are two distinct ways to post-process $LEMLES$ species and reaction rates data. The first one consists of post-processing all LEM data. Because of the number of LEM points per LES cell, this technique is expensive and requires a large amount of memory. The other technique consists of averaging all LEM variables at the LES level and output the LES averaged values. This latter technique is usually used Sankaran et al. [2003], Eggenspieler and Menon [2003b]. However, this technique presents some challenges. Averaging LEM data can lead to error in their interpretation. Depending upon the distribution of the LEM fields and the LES cells, results of the averaging procedures can be different. An example is given by Figures 6.1 (a) and 6.1 (b). Let us assume a distribution of the scalar ψ at the LEM

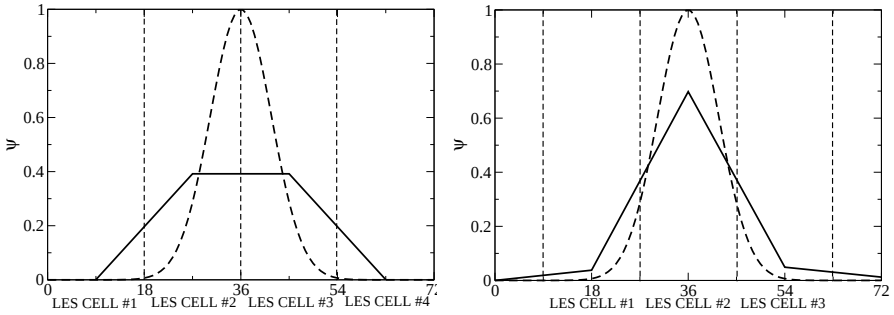

(a) LES cells distribution 1 (b) LES cells distribution 2

Figure 6.1: LES averaging of a LEM resolved scalar ψ for two different distribution of the LES cells.

level. By doing the average, Figure 6.1 (a) indicates that the maximum value of ψ is 0.4 and Figure 6.1 (b) indicates that the maximum value of ψ is 0.7 while the real maximum is 1.0. Interpreting directly Figure 6.1 (a) or Figure 6.1 (b) can therefore lead to large errors and this has to be kept in mind when analyzing $LEMLES$ results.

6.2 Flame Propagation in a High Isotropic Turbulence Field

The propagation of a flame in an isotropic turbulent field is studied. The flame propagates in the BRZ regime and the smallest turbulent structures are theoretically supposed to quench the flame. This study was performed in a two dimensional computational domain with an 4-step mechanism. The setup of the simulation is summarized in Table 6.1.

Table 6.1: Turbulent flame properties of the flame propagating in an isotropic turbulent field. Φ : equivalence ratio. u': subgrid velocity fluctuations. S_L: laminar flame speed. L: integral length scale. δ_F: flame thickness. η: Kolmogorov scale. Re_L: Reynolds number based on the integral length scale. Re_λ: Reynolds number based on the Taylor Micro-scale. L_{Box}: box size.

Φ	u'/S_L	L/δ_F	η/δ_F	Re_L	Re_λ	T_{ref}	L_{Box}	L_{Box}/L
0.45	85.0	1.4	0.0015	350	75	644.0	1.5 cm	50

Fuel reaction rates are shown in Figure 6.2. Both LEM reaction rates (Figure 6.2 (a)) and LES averaged reaction rates (Figure 6.2 (b)) are plotted. The turbulence being high, L/δ_F is of the order of unity and the flame surface is only slightly wrinkled. This is a direct

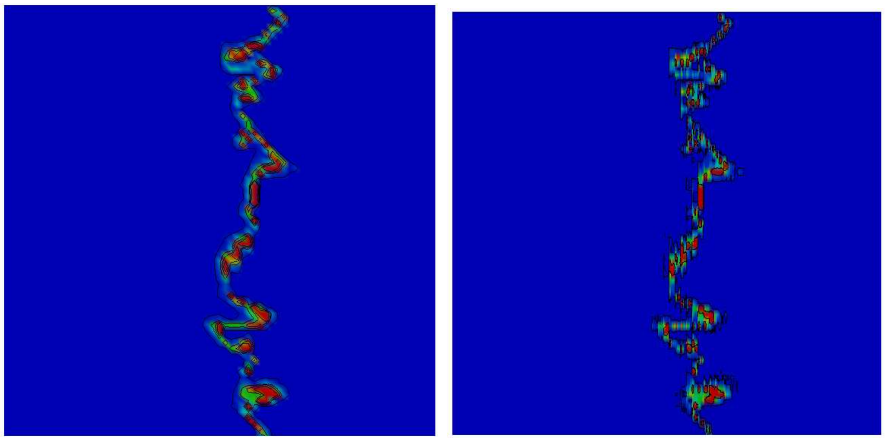

(a) *LES*-averaged value of the *LEM* fuel reaction rates

(b) *LEM* fuel reaction rates

Figure 6.2: Instantaneous fuel reaction rates (Blue: 0 s^{-1} - Red: -150.0 s^{-1}).

consequence of the turbulence field generation (a lower turbulence level would yield a larger L/δ_F and the flame would be more wrinkled). The reaction rates vary from -150 to -20 and no complete flame extinction is observed. However, it is clear that the flame structure is greatly affected by turbulence, both at the *LES* and *LEM* level.

The fuel reaction rates are studied in more details. The *LEM* fuel reaction rate ($\dot{w}_{CH_4}$) is plotted as a function of the *LEM* methane mass fraction Y_{CH_4} at the beginning of the simulation (t/τ_0=1 - Figure 6.3 (a)) and at the end of the simulation (t/τ_0=15 - Figure 6.3 (b)), where τ_0 is the eddy turn-over time defined as:

$$\tau_0 = \frac{L}{u'} \tag{6.1}$$

Figure 6.3 (b) shows that $\dot{w}_{CH_4}$ diffuses around its "laminar" value shown in Figure 6.3 (a). The broadening of $\dot{w}_{CH_4}$ as a function of Y_{CH_4} is a direct result of the action of the subgrid stirring as well as the action of molecular and numerical diffusion. However, there is no indication that the flame is partially or totally quenched. This contradicts results from the observation of Figure 6.2 (a) or (b). By looking at one of those figures, one may conclude that some portions of the flame are quenched. However, a more careful study of the fuel reaction rates (Figure 6.3) shows that it is not the case. Note that this observation is valid

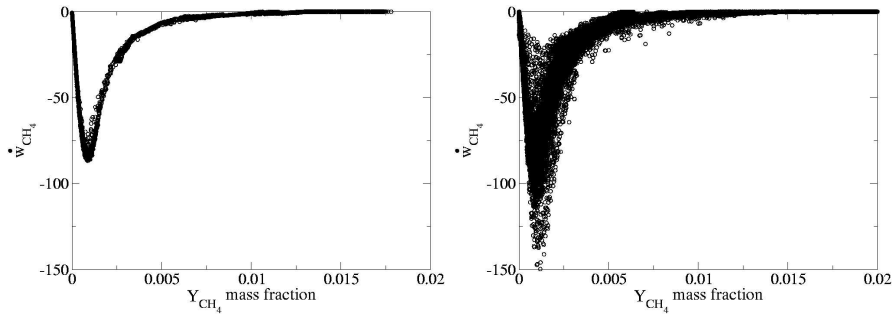

(a) t/τ_0=1 (b) t/τ_0=15

Figure 6.3: Fuel reaction rates ($\dot{w}_{CH_4}$) plotted as a function of the fuel mass fraction (Y_{CH_4}).

for any of the 4-step mechanism used in this test.

This being rather surprising, the LEM temperature, Y_{CH_4} and $\dot{w}_{CH_4}$ fields are plotted along a line crossing the flame front at two locations: one where $\dot{w}_{CH_4}$ is high and one where $\dot{w}_{CH_4}$ is low. Results are shown in Figure 6.4. This representation is not a physical representation because the LEM domains are 1-dimensional and Figure 6.4 has to be viewed only as a schematic representation of the species, temperature and reaction rate fields. Figure 6.4 (a) shows a region where $\dot{w}_{CH_4}$ is low. The reaction rate region is narrow and combustion occurs only when $Y_{CH_4}/Y_{CH_{4,max}} \approx 0.25$ and $T/T_{max} \approx 0.85$. On the other hand, the fuel reaction rate showed on Figure 6.4 (b) is high and combustion occurs for $Y_{CH_4}/Y_{CH_{4,max}} \approx 0.01$ and $T/T_{max} \approx 0.91$. This is in agreement with the theory that high reaction rates are reached for T close to T_{max} and Y_{CH_4} close to 0. Both plots showed in Figures. 6.4 represent flame structures, but one field (Figure 6.4 (b)) contains values of T and Y_{CH_4} that allows high $\dot{w}_{CH_4}$ while the other one (Figure 6.4 (a)) does not. The differences in the LEM fields are linked to the LEM splicing and diffusion. Hence, the difference in the fuel reaction rates is purely a numerical artifact and does not indicate a region of locally quenched reaction zone. This is in agreement with results presented in Figure 6.3. In conclusion, the $LEMLES$ study of a premixed flame propagating in an isotropic turbulent field did not exhibit neither partial nor complete flame extinction.

Sankaran [2003] demonstrated that the reaction rates varies as a function of the flame

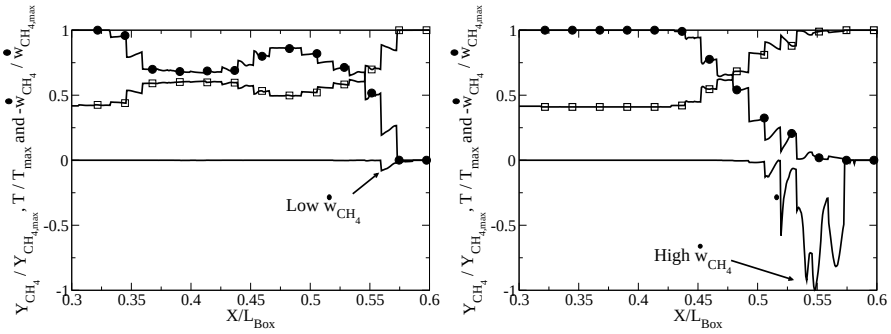

(a) LEM fields where $\dot{w}_{CH_4}$ is low (b) LEM fields where $\dot{w}_{CH_4}$ is large

Figure 6.4: Representation of LEM fields along lines perpendicular to the flame surface. Normalized temperature, fuel mass fraction and fuel reaction rates are plotted. Solid line: $\dot{w}_{CH_4}$, bulleted-line: Y_{CH_4} and squared-line: temperature.

curvature. A lean premixed CH_4-air flame having a Lewis number (Le) lower than unity was studied. It was determined that flame curvature at the LES level affects the fuel reaction rate because of unbalanced ($Le \neq 1$) molecular diffusion of species and temperature. In his study, flame curvature is observed at the LES level. However, as indicated in section 5.2.5, there is no molecular diffusion of heat and species at the LES level. Hence, at the LES level, effects of flame curvature on the reaction rate can not be observed and the conclusions of Sankaran [2003] are arguable.

Also, the LEM fields are 'flat' and are not consistent with the general $LEMLES$ model goals, which is to resolve the subgrid structure of the flame. In the simulation of flame propagation in an isotropic box, the time step is very low, when compared to classical time step of a full-scale LES simulation of a combustion chamber. As a results of this small time step, few materials are spliced at every time step and the lack of inter-LES cells diffusion tends to flatten the LEM field. On the contrary, in a full-scale combustion chamber simulation, the time step is large (by one order of magnitude) and the a large amount of materials is spliced between LEM domain. As a results, molecular diffusion can not flatten the LEM field and the LEM species fields are non-uniform.

6.3 Flame Extinction With Heat Losses

The study of the propagation of a flame in the BRZ regime in an isotropic turbulent field does not exhibit any local or complete flame extinction. Therefore, premixed flame propagation is studied in a real case scenario: combustion inside a full scale industrial dump combustion chamber. In this case, also, the simulation does not exhibit any flame extinction. Hence, perturbations to the flame propagation are implemented in the form of local heat losses. This technique is described in the next section.

6.3.1 Heat Losses Modeling

Heat losses occur at the walls of the combustion chamber. The walls materials cannot withstand the high product temperature and walls are usually cooled or cool air is injected via holes in the combustion chamber to create a protective colder layer of gases. Considering wall related heat losses is not practical in LES because the LES resolution does not allow to resolve the wall thermal boundary layer. However, one can simulate heat losses by directly including them locally. Following the study of Poinsot et al. [1991], heat losses (dT_{HL}/dt) are included in the energy balance in the form of a linear term:

$$\frac{dT_{HL}}{dt} = \frac{h}{\rho C_P}(T - T_1) \tag{6.2}$$

where T_1 is the reactant temperature and T is the LES temperature. The coefficient h is defined as follow:

$$h = \lambda S c^2 \big(\frac{S_L}{\nu}\big)^2 \frac{c}{\beta} \tag{6.3}$$

where $\lambda = \mu C_P/P_r$, β is the reduced activation energy Williams [1985] and c is a dimensionless heat-loss coefficient. Heat losses are taken into account only in the post-flame region and are a direct function of the product temperature.

The next figures illustrates the behavior of the temperature field for c=0 (Figure 6.5 (a)), c=10^{-4} (Figure 6.5 (b)) and c=10^{-3} (Figure 6.5 (c)). For medium heat losses (c=10^{-4}), an equilibrium exists between the heat released by the flame front and the heat losses whereas for the case with large heat losses (c=10^{-3}) such an equilibrium does not exist and the flame quenches. This latter case is of no interest and the value of c is taken as 10^{-4}. Heat losses

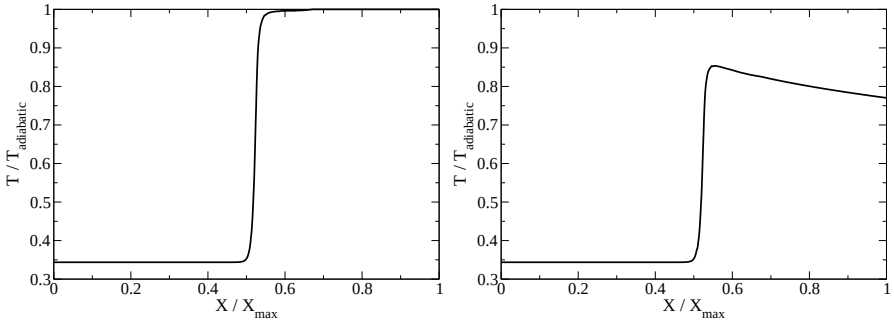

(a) c=0

(b) c=10^{-4}

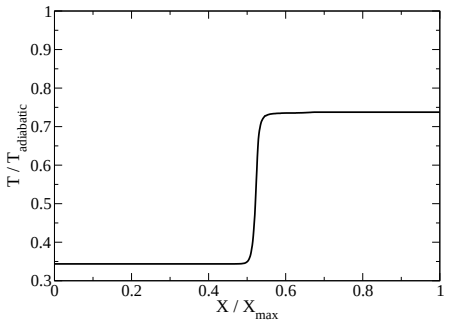

(c) c=10^{-3}

Figure 6.5: One-dimensional flame normalized temperature profiles for different values of the heat loss coefficient c. representation valid for all equivalence ratios.

are implemented in the region close to the edge formed by the expansion of the inflow pipe inside the combustion chamber. Heat losses are limited to the region in a 1.5 mm radius from this edge. As a result, the final value of c is given by:

$$c = f(r)c^* \tag{6.4}$$

where c^*=10^{-4} and $f(r)$=$max((1-r/1.5), 0)$ with r taken as the distance from the considered point to the edge of the inflow pipe.

Heat losses are only implemented at the LEM level and are neglected at the LES level. The LES energy equation is written in a conservative form and does not support the addition of energy loss. As a consequence, heat losses are taken into account at the *chemical* (LEM) level (where the computation of the reaction rate is performed) but not at the $flow$ (LES) level (where the momentum equation are solved). It is assumed that

heat losses have a limited impact on the flow field, hence, neglecting heat losses at the LES level is assumed to not perturb the results of the simulation.

6.4 Flame Propagation in a Dump Combustion Chamber

6.4.1 LEM Resolution and Turbulent Combustion Regimes

The choice of the number of LEM cells per LES cell is a compromise between the need to resolve all turbulent and chemical length scales and the computational cost. The LEM resolution is chosen as 18 LEM cells per LEM line in this study. Figure 6.6 (a) shows the typical distribution of the LES subgrid velocity fluctuations (u') in the combustion chamber. For each level of turbulence (i.e. for each u'), a PDF of the eddy size can be computed Menon et al. [1993]. Using this eddy size PDF distribution, the expected eddy size ($\overline{L}$) is computed for all values of u' and is expressed as the number of LEM cells needed to resolve it. A minimum of six LEM cells is needed to resolve an eddy. All eddies larger than six LEM cells are fully resolved. Figure 6.6 (a) shows that 97% of subgrid eddies are resolved (Domain (A)), and only 3% of subgrid eddies are under-resolved (Domain (B)).

It is also of great interest to evaluate the resolution of the LEM line with respects to the resolution of the different premixed turbulent combustion regimes. Figure 6.6 (b) shows the CDF distribution of the eddy size and the Karlovitz number ($Ka=(\delta_F/\eta)^2$) as a function of u' for Φ=0.45. Figure 6.6 (b) shows that both the flamelet and the TRZ regime are fully resolved (domain (I)). Around 6 % of the domain has a level of turbulence corresponding to the BRZ regime (domain (II) and (III)). In domain (II), all scales relevant to the flame/eddy interactions are resolved at the LEM level whereas these interactions are under-resolved in domain (III). It is important to note that Figure 6.6 (b) shows that the flame does not propagate in the flamelet regime ($Ka<1$). This is due to the fact that only the LES subgrid turbulent scales are considered in Figures 6.6 (a) and 6.6 (b). For low level of u', the frequency of occurrence of subgrid eddies is negligible and only LES resolved eddies affect the flame front. LES resolved eddies are larger than the flame front. Therefore, for low level of turbulence, the flame propagates in the flamelet regime.

The flame front thickness is 0.15 mm and 1.2 mm for Φ=1.0 and Φ=0.45, respectively.

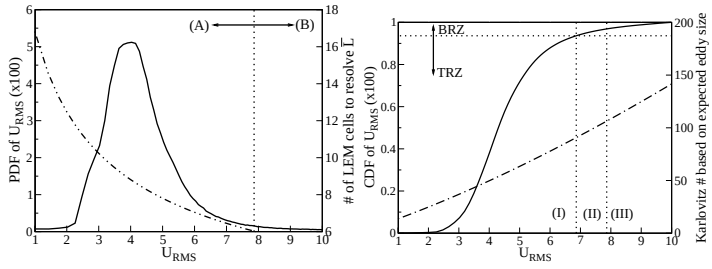

(a) (b)

Figure 6.6: Analysis of the resolution, at the LEM level, of all relevant subgrid eddies and combustion regimes. (a) PDF distribution of the subgrid velocity fluctuations u' $(-)$ and expected eddy size $\overline{L}$ $(- \cdot\cdot -)$ as a function of u'. Domain (A) and Domain (B) are defined in sec. 6.4.1. (b) CDF distribution of the subgrid velocity fluctuations u' $(-)$ and Karlovitz number $(- \cdot\cdot -)$ associated with the expected eddy size $\overline{L}$. Domain (I), (II) and (III) are defined in sec. 6.4.1.

In the flame region, the typical LES resolution is 0.45 mm. Thus, on average, with 18 LEM cells per LES cell, the flame is resolved using 5 LEM for Φ=1.0 and 40 LEM cells for Φ=0.45.

6.4.2 Flow Features

The main features of the flow fields for Cases 1 and 2 are compared. The time-averaged axial velocity profiles are shown on Figure6.7 (a), for Φ = 1.0 and on Figure6.7 (b), for Φ = 0.45. Figure 6.8 shows the time-averaged swirl number for both equivalence ratio as a function of the distance from the inflow. The sudden jump in the value of the swirl number is related to the change in radius used in the computation of the swirl number. The radius changes from the radius of the inflow pipe to the radius of the combustion chamber. Both the axial velocity profiles and the variation of the swirl number along the centerline are very similar for Φ=0.45 and Φ=1.0. For both cases, two recirculation regions are present. The first one is located downstream of the dump plane (i.e. corner recirculation region) and is created by the sudden expansion of the inflow pipe inside the combustion chamber. The second one is located in the centerline region and is created by the swirling flow. Both recirculation regions stabilize the flame by recirculating high temperature products upstream and towards the flame front. The vortex breakdown bubble is responsible for the

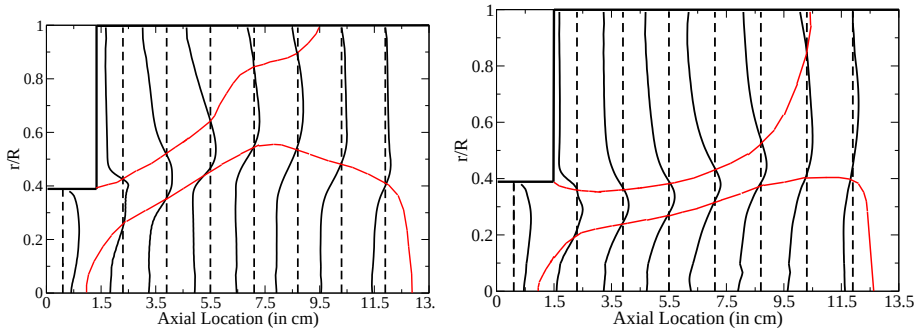

(a) $\Phi = 1.0$ (b) $\Phi = 0.45$

Figure 6.7: Time-averaged axial velocity profiles for Case 1 and 2. The locations of the recirculation regions are indicated by plotting the iso-lines corresponding to a null axial velocity. The solid lines represent the time-averaged velocity profiles and the dashed lines represent the null velocity profiles at each location.

tulip-like shape of the flame for Φ=1.0.

For Φ=0.45, the results presented in this section seem to contradict the results presented in sec. 5.2.2. In sec. 5.2.2, we noted that the centerline vortex breakdown is divided in two regions. The first central recirculation region is located on the fuel side while the second central recirculation region is located on the product side. This is not visible in Figure 6.7 (b). Results presented in sec. 5.2.2 are *instantaneous* while the results presented in this section are $time-averaged$. In time, the instantaneous structures visible in sec. 5.2.2 moves upstream and downstream of the dump plane, hence the time averaging process smooths the data and only one large recirculating region is visible. This may be explain by the fact that one of the two recirculation regions is stronger and/or that the two recirculation regions merge. Only a computation over an even longer time span can answer this question.

6.4.3 Flame Extinction

In this section, results of simulation of the full scale dump combustor with heat losses are presented and discussed. Data reported here are collected using the 4-step mechanism. Figure 6.9 shows iso-surface of $\dot{w}_{CH_4} = 5\ s^{-1}$ for $\Phi = 1.0$ at four different times. In this case, flame extinction is not observed (chemical heat release counteracts the action of the heat losses). However, Figure 6.10 shows the fuel reaction rate iso-surface for $\Phi = 0.45$

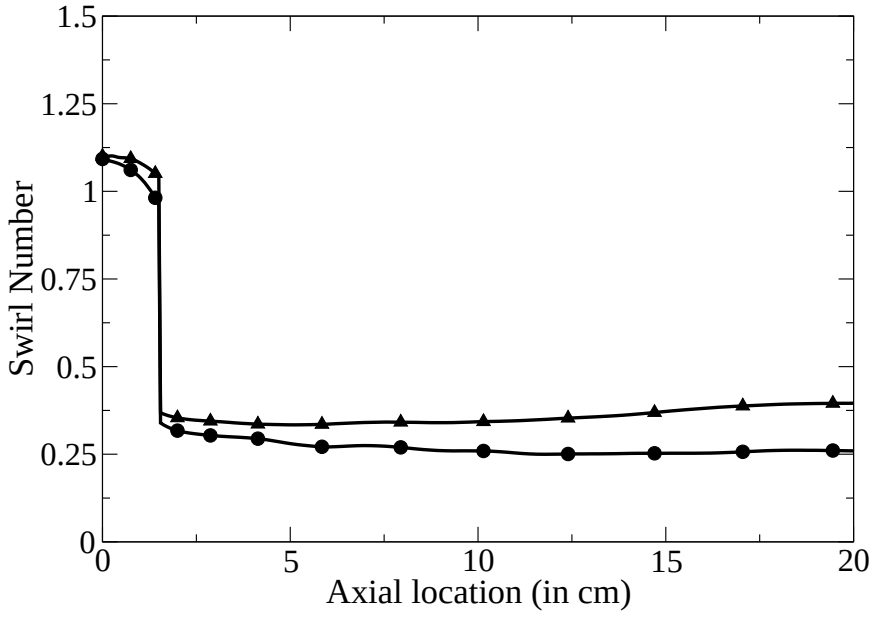

Figure 6.8: Time-averaged swirl number as a function of the axial location. The dump plane is located at X = 1.5 cm. Bullet: Φ=0.45 - Triangle: Φ=1.0.

and flame lift-off is clearly visible. Flame extinction varies in time and space. When heat losses are introduced, flame extinction is visible when $\dot{w}_{CH_4}$ is plotted as a function of Y_{CH_4}. Figure 6.11 (a) corresponds to $\Phi = 1.0$ and Figure 6.11 (b) corresponds to $\Phi = 0.45$. For $\Phi = 1.0$, results are comparable to the trends observed in sec. 6.2: the fuel reactions rates are spread over a large range but no flame extinction is observed and the spreading of the points is mainly a result of the simulation of heat losses. However, for $\Phi = 0.45$, values of $\dot{w}_{CH_4}$ are more spread and can reach 0 for all values of Y_{CH_4}, hence proving that some portion of the flame are quenched. Similar results can be obtained using the 1-step mechanism. Thus, flame lift-off through heat losses can be studied with a 1-step mechanism.

Figure 6.10 and Figure 6.11 (b) clearly indicate that the introduction of the heat losses does not fully prevent combustion. Rather, heat losses perturb the flame propagation and, depending upon the subgrid phenomena, quench or do not quench the flame front.

6.4.4 Behavior of the Radicals and Minor Species

In this section, we focus on the relation between $\dot{w}_{CH_4}$ and the radical H and the minor species H_2. Figure 6.12 shows $\dot{w}_{CH_4}$ as a function of H_2. Data of Figure 6.12 (a) were

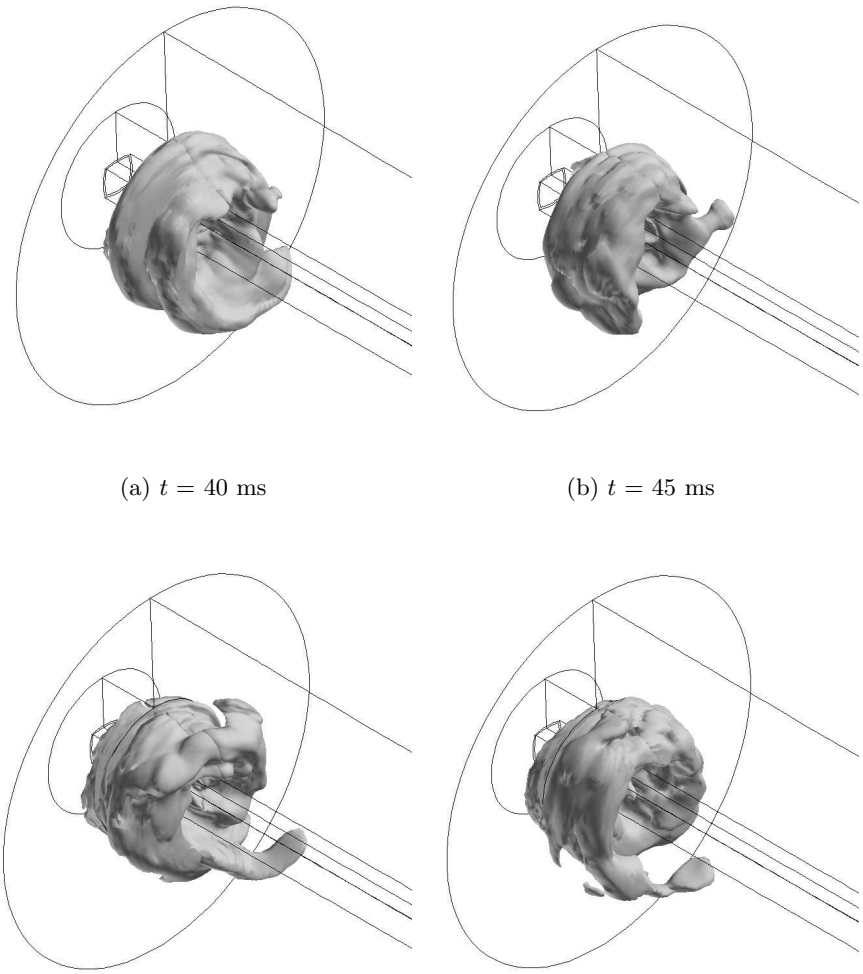

(a) $t = 40$ ms

(b) $t = 45$ ms

(c) $t = 50$ ms

(d) $t = 55$ ms

Figure 6.9: Instantaneous fuel reaction rate iso-surfaces for Φ=1.0.

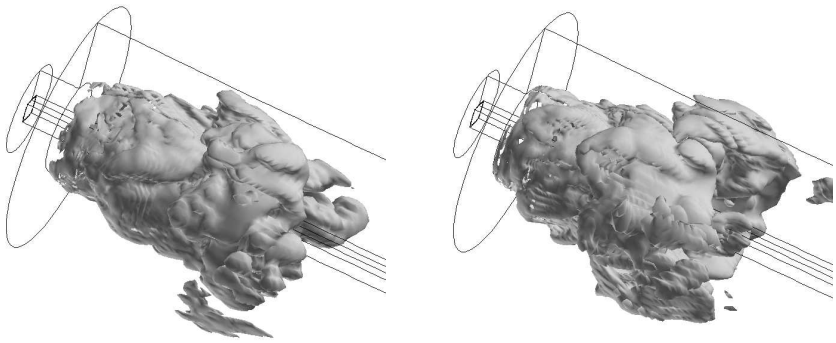

(a) t = 40 ms

(b) t = 45 ms

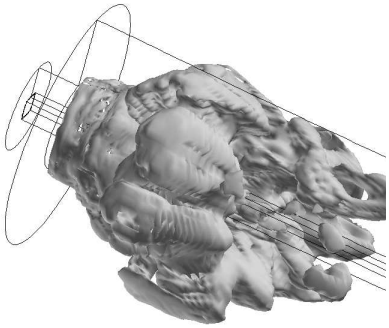

(c) t = 50 ms

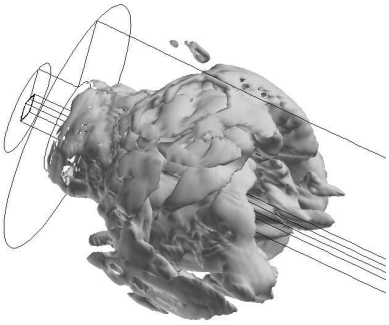

(d) t = 55 ms

Figure 6.10: Instantaneous fuel reaction rate iso-surfaces for Φ=0.45.

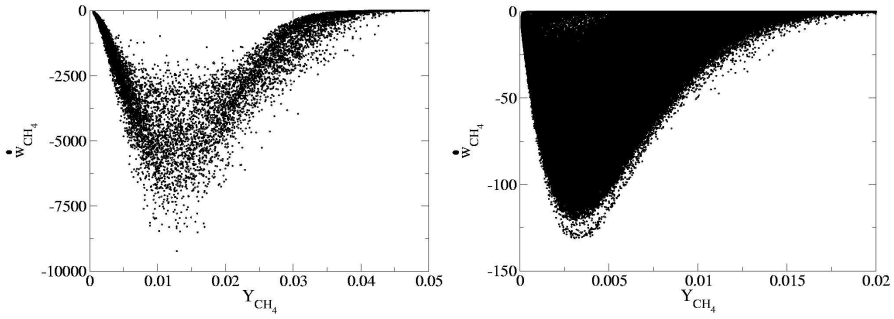

(a) Φ = 1

(b) Φ = 0.45

Figure 6.11: *LEM* fuel reaction rates plotted as a function of the *LEM* fuel mass fraction. Data taken in the region comprised between between the dump plane and 2.0 cm downstream of the dump plane. In regions farther downstream of the dump plane, no flame extinction is observed and the two plots have the same shape.

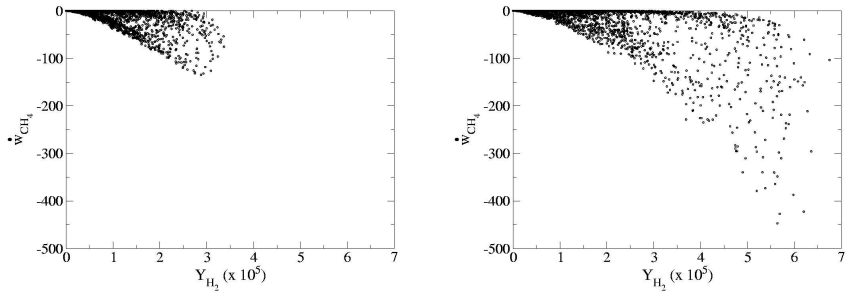

(a) Region where flame extinction is observed

(b) Region where flame extinction is not observed

Figure 6.12: *LEM* H_2 mass fraction as a function of the *LEM* fuel reaction rate. 4-step chemical mechanism.

collected in the region where flame quenching occurs while data of Figure 6.12 (b) were collected in regions where no flame extinction is observed. The trends in Figure 6.12 are similar but the data are more spread in Figure 6.12 (b). The same trend is observed when $\dot{w}_{CH_4}$ is plotted as a function of H (Figure 6.13). Again, data of Figure 6.13 (a) were collected in the region where flame quenching occurs while data of Figure 6.13 (b) were collected in regions where no flame extinction is observed (i.e. downstream of the dump plane). The spreading of the data for Figures 6.12 (b) and 6.13 (b) is, again, related to numerical and molecular diffusion. These observations prove that no difference in the H or H_2 fields are noticeable when heat loses are considered. Portion of the flame where a strong temperature gradient but no radicals (regions defined as "quenched but active" flame front by Buschmann *et al.*) are not observed. This may be related to the use of simplified chemical mechanism. If such regions are of interest, a chemical mechanism that includes major radicals like OH should be employed.

6.4.5 CO Emission

An instantaneous flame iso-surface and CO mass fraction field are shown in Figure 6.14 for $\Phi = 0.45$. The average CO mass fraction at the exit of the combustion chamber is 10 ppm, which is higher than the equilibrium value. The combustion chamber is short and

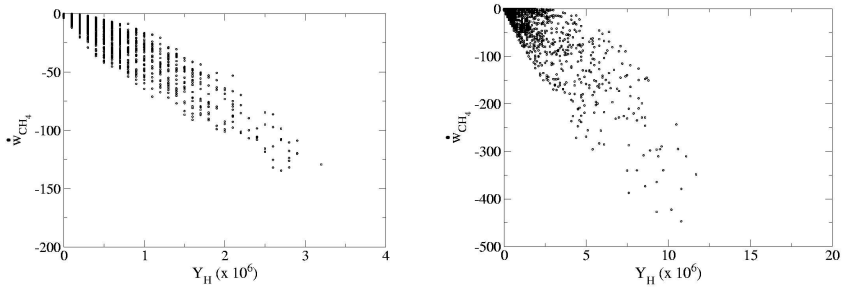

(a) Region where flame extinction is observed

(b) Region where flame extinction is not observed

Figure 6.13: *LEM H* mass fraction as a function of the *LEM* fuel reaction rate. 4-step chemical mechanism.

not all *CO* formed at the flame front is oxidized before reaching the combustion chamber outflow. No *UHC* is produced, hence *UHC* is not a second source of *CO*, contrary to the what was observed for the $DOE - HAT$ case (see. Chapter 4). This does not contradict previous results (see Chapter 4). In this case, as in the $DOE - HAT$ case, the flame front may quench and unburnt fuel may be released in the post-flame region. Results presented here only indicate that the *LEMLES* model did not predict flame extinction leading to the release of unburnt fuel in the post-flame region.

6.4.6 Dynamics of Flame Lift-off

The sum of all local fuel reaction rates (in the region from the dump plane to 7.5 mm downstream of the dump plane) is computed as a function of time and is plotted in Figure 6.15. The maximum absolute value of the sum is used to normalize the data. The first mode of the oscillations is extracted. The flame can be considered as lifted-off when the normalized sum of the reaction rate is smaller than -0.5. The flame is attached to the inflow pipe lips when the normalized sum of the reaction rate is large than -0.5 (Note that this is one out of many possible definitions of flame lift-off). The first mode of the oscillations has a frequency of approximately 1,000 Hz. The flame extinction frequency matches the longitudinal half quarter mode of the combustion chamber.

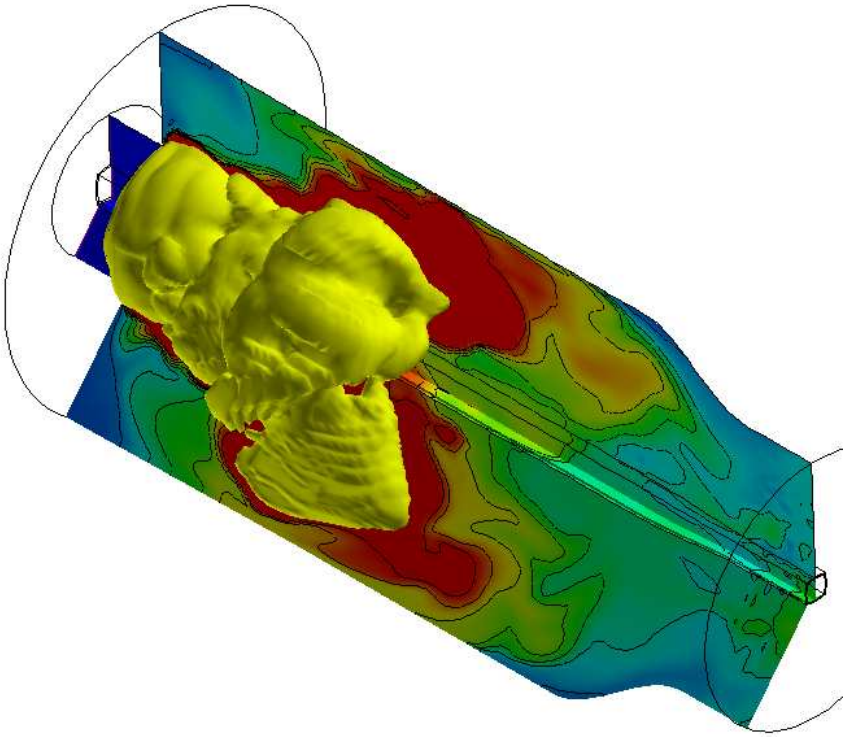

Figure 6.14: Instantaneous flame isosurface and CO mass fraction field. A logarithm scale is used for the CO mass fraction field.

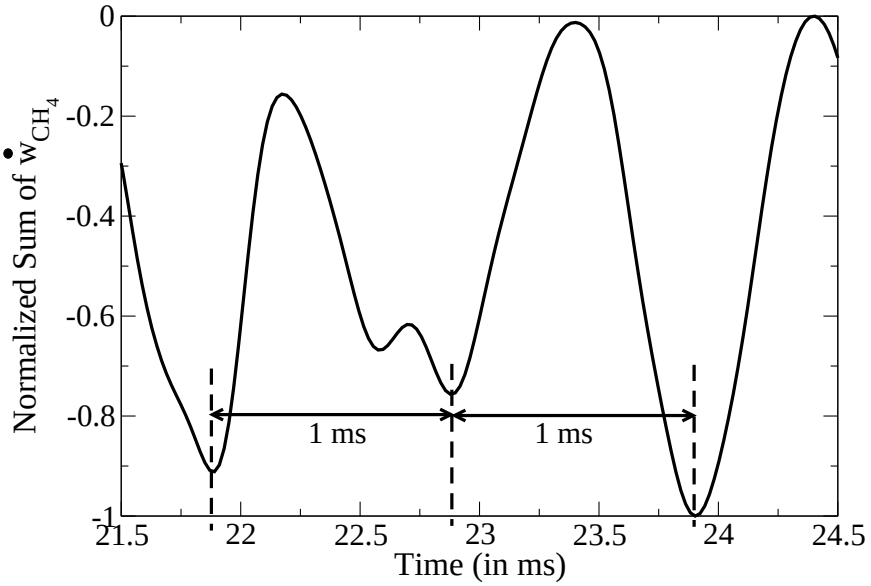

Figure 6.15: Normalized sum of the reaction rate in the region close to the dump plane as a function of time. The data is smoothed in order to extract the first frequency mode.

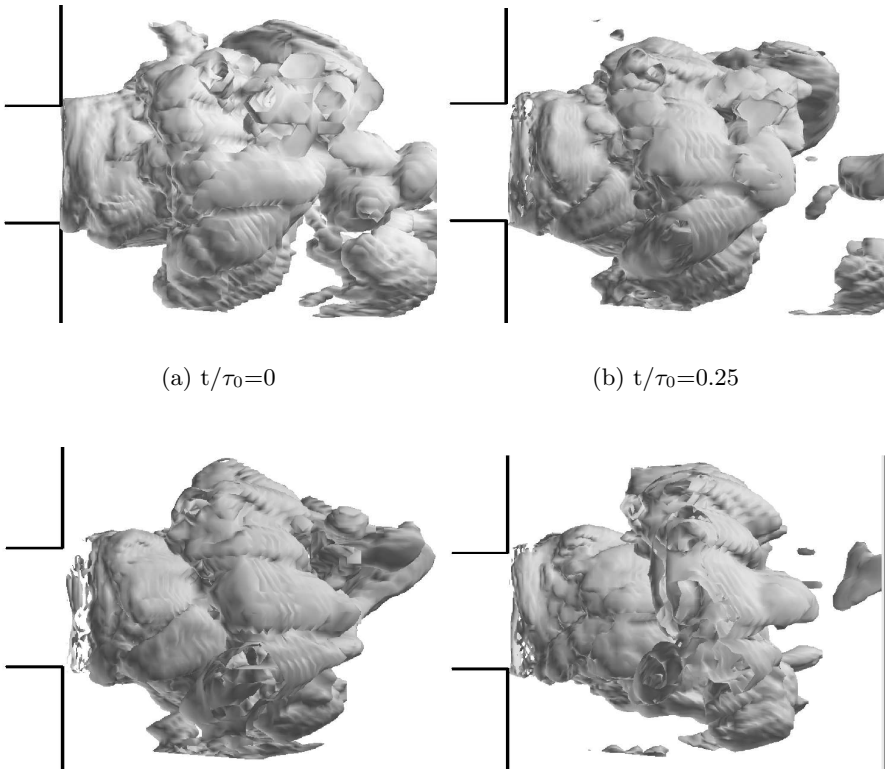

(a) t/τ_0=0 (b) t/τ_0=0.25

(c) t/τ_0=0.50 (d) t/τ_0=0.75

Figure 6.16: Time averaged fuel mass fraction. τ_0=1 ms.

To gain more insight into the flame lift-off dynamics, reaction rate isosurface is shown in Figure 6.16 at four different times in the 1 ms time span. A reason that may explain the dynamics of flame lift-off is related to the displacement of hot products induced by the pressure waves present in the combustion chamber. When a pressure wave propagates downstream, heat losses built-up, the flame quenches and lifts-off. When the pressure wave propagates upstream, hot products are entrained to the dump plane region and counteract the action of the heat losses. In this later case, the flame front is not quenched and the flame is attached to the dump plane. This is similar to the compact flame regime observed by Sommerer et al. [2004].

6.4.7 Comparison of the 1- and 4-Step Mechanisms

In this section, we compare the performances of the 1-step mechanism versus the 4-step mechanism. Table 6.2 compares the computational time for both mechanisms. The computational time required with the $GLES$ method is used as a reference. When collecting these data, the number of processors is kept constant for all computations. In the $LEMLES$ model, the larger computational cost is the cost of the computation of the chemistry (57% and 68% of the total computational cost, for the 1- and 4-step mechanism, respectively). The new method developed to compute the reaction rates (see sec. 3.6) is four times and three times faster for the 1- and 4-step mechanism, respectively. In order to decrease the wall-clock computational time when the $LEMLES$ model is used, the number of processors used is increased.

Table 6.2: Comparison of the computational cost of different approaches for the 1- and 4-step mechanisms. The $GLES$ computation time is used as a reference.

Model	Time
$GLES$	1
$LEMLES$ - 1-step - No reaction	3
$LEMLES$ - 1-step - Reaction	7
$LEMLES$ - 1-step - Reaction (DVODE)	28
$LEMLES$ - 4-step - No reaction	6
$LEMLES$ - 4-step - Reaction	25
$LEMLES$ - 4-step - Reaction (DVODE)	80

The 4-step mechanisms should be more accurate and detailed than the 1-step mechanism and includes radical and minor species (H and H_2) as well as pollutants (CO). In this study, no difference between the two models was observed in terms of flame extinction but the 4-step mechanism is able to predict the combustion chamber CO emissions.

In conclusion, the 4-step mechanism is more accurate but this accuracy has a cost (this mechanism is 3.5 times more computationally expensive than the 1-step mechanism). The computational cost of a $LEMLES$ simulation with detailed chemistry (i.e. more than 1 step) is the biggest disadvantage of the model.

CHAPTER VII

SYSTEMS WITH NON-UNIFORM INFLOW CONDITIONS

In chapter V, UHC formation as a result of flame extinction is determined as being a key element for accurate prediction of the CO emission. In the previous chapter, flame extinction is simulated. However, even if the flame quenches, no emission of UHC is visible. Three main reasons can explain this observation: chemical, geometrical and numerical issues.

One could argue that the reduced mechanisms used in this work prevent the formation of UHC. When the flame quenches, the typical flame front structure collapses and the radical mass fractions strongly deviate from their value (or profile) when the flame is propagating. Therefore, re-ignition can be delayed and this delay corresponds to the time needed by the unburnt fuel to migrate in the post-flame region. While the 1-step chemical mechanism does not incorporates radicals, the 4-step does, but no UHC emission was observed. The use of simplified chemical mechanisms may explain why no UHC is released in the post-flame region. A more detailed 16-species chemical mechanism is too expensive and cannot, at the moment, be used in the simulation of a full scale combustion chamber.

If strong enough, the vortex created at the expansion of the inflow pipe inside the combustion chamber may be able to convect unburnt fuel from the reactants side to the products side when the flame front quenches. In this study, the vortices shedding from the lips of the inflow pipe are not strong enough to convect reactants. A different, less "simple" geometry, may provide vortices strong enough to push unburnt fuel on the product side.

The last explanation can be related to the simulation itself. In experiments, combustion instabilities perturb the feeding system and the reacting mixture is not perfectly mixed Lieuwen and Zinn [1998], as assumed in the simulations performed in the previous chapter. As a result, the formation of UHC can be linked to these non-uniformities. Therefore, this

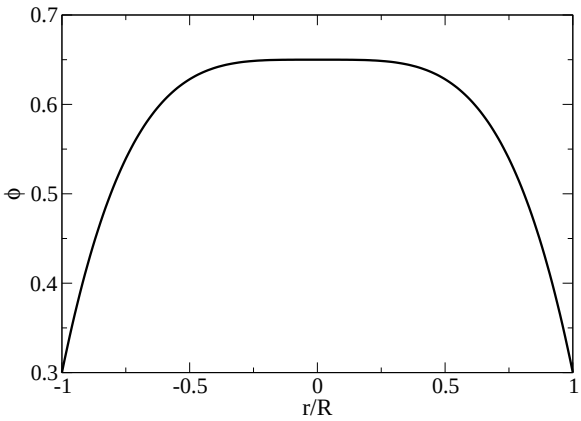

Figure 7.1: Inflow equivalence ratio as a function of the radial location r. Here R is the inflow pipe radius.

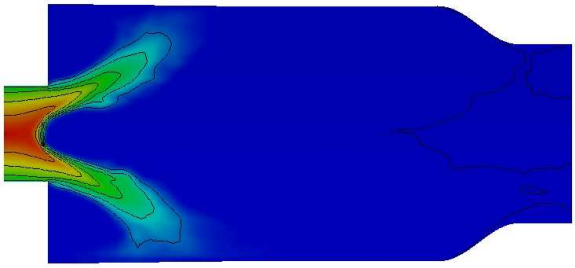

Figure 7.2: Time-averaged fuel mass fraction field. Red: reactant with Φ=0.65. Green: reactant with Φ=0.3. Blue: products.

chapter focuses on simulation of systems where the inflow mixture is non-uniform in time and space (Case 3 and 4).

7.1 Spatially Non-Uniform Equivalence Ratio

The inflow reactant equivalence ratio profile is shown in Figure 7.1. The flammability limit of the premixed mixture is Φ=0.42. For reference, the time-averaged fuel mass fraction field is shown in Figure 7.2

Theoretically, when Φ is lower than 0.42, the flame does not propagate because the post-flame temperature is too low. However, in this case, the post-flame temperature is not constant and does not depend solely on the mixture equivalence ratio. In the centerline region, where the equivalence ratio is maximum (Φ=0.65), the post-flame temperature is

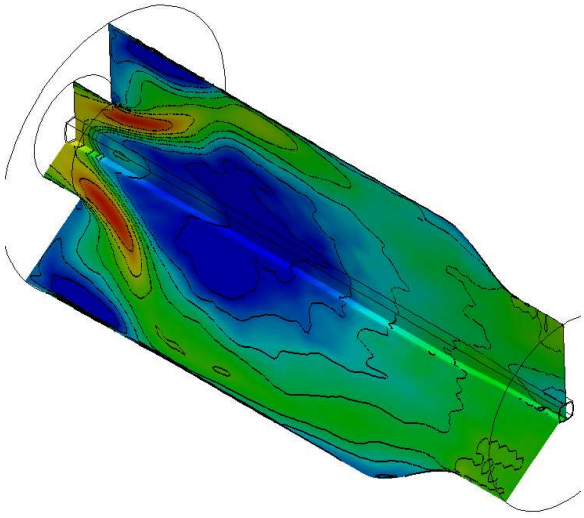

Figure 7.3: Time-averaged axial velocity field - Case 4 - Case 4 (blue : -20 m.s^{-1} - Red : 70 m.s^{-1}).

much larger than in region closer to the inflow pipe walls, where Φ is minimum.

The vortex breakdown and the dump plane recirculation regions (shown in Figure 7.3) convect high temperature products upstream and mix with the lower temperature products. As a result, the temperature of the products where Φ is minimum is always higher than the theoretical adiabatic product temperature and the flame propagates. More detailed, time averaged, axial velocity profiles are shown in Figure 7.4 and the recirculation regions are clearly visible. The time averaged temperature field is shown in Figure 7.5 and confirms that the average temperature is, in region of low Φ, larger than the theoretical adiabatic flame temperature.

An instantaneous fuel reaction rate iso-surface and the fuel mass fraction field are shown in Figure 7.6. In the region of low equivalence ratio, the flame, locally, does not propagate. The flame only propagates downstream of the dump plane, when the post-flame temperature is high enough. In this case, no formation of UHC was observed.

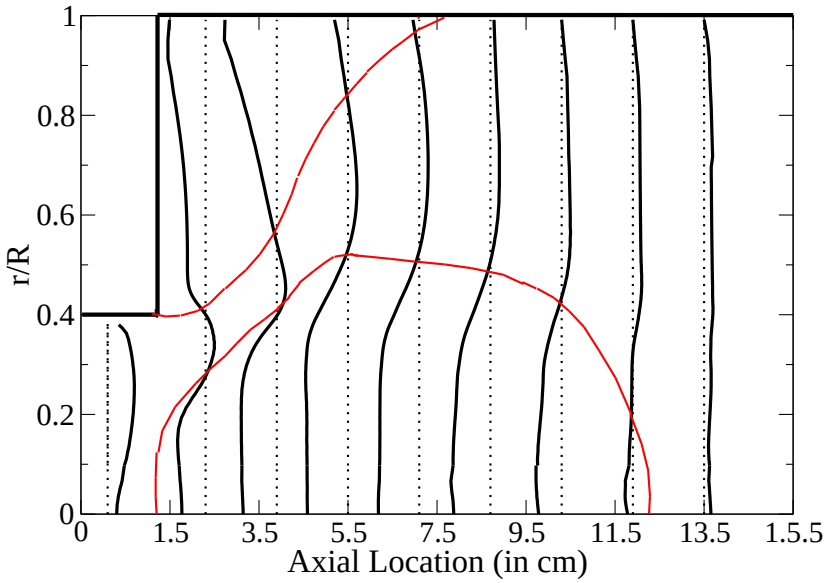

Figure 7.4: Time-averaged axial velocity profiles for Case 3. The locations of the recirculation regions are indicated by plotting the iso-lines corresponding to a null axial velocity. The solid lines represent the time-averaged velocity profiles and the dashed lines represent the null velocity profiles at each location.

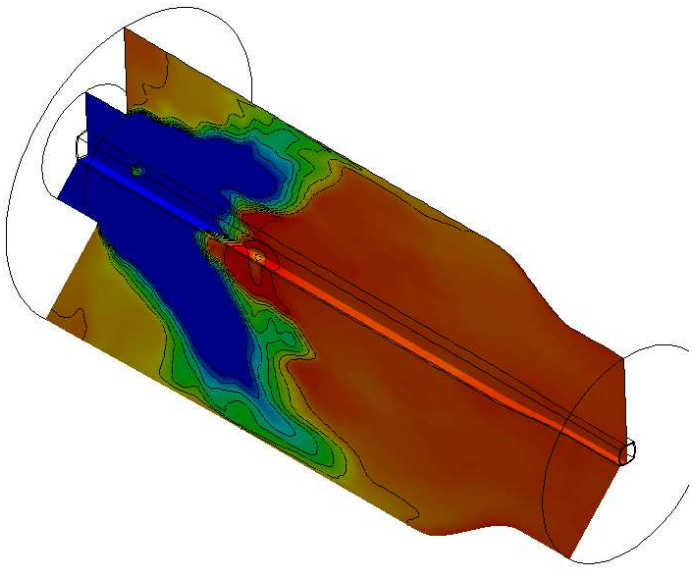

Figure 7.5: Time-averaged temperature profiles - Case 4 (blue : 1450 K - Red : 1700 K).

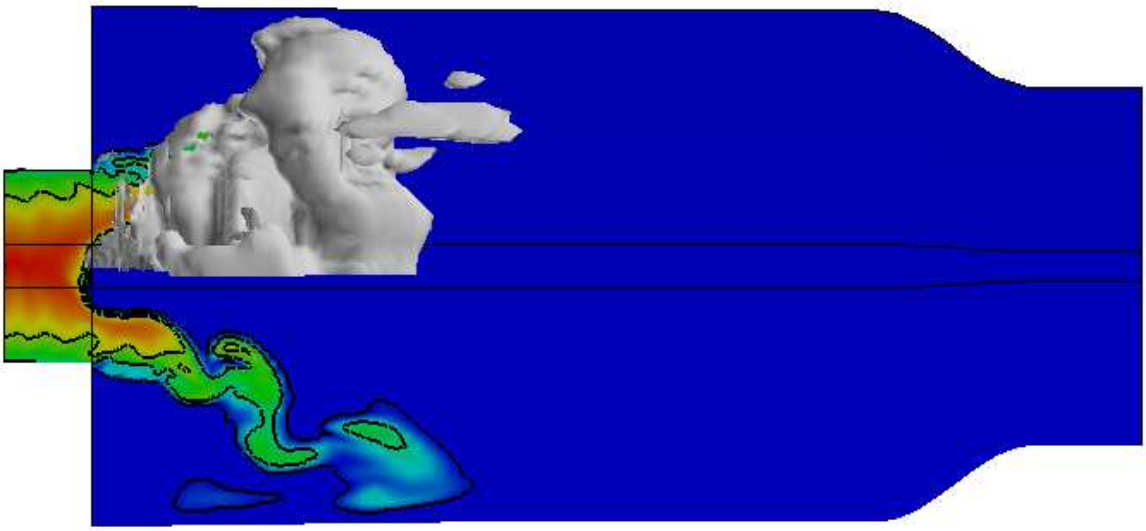

Figure 7.6: Instantaneous fuel reaction rate iso-surface ($\dot{w}_{CH_4}$=-5 s^{-1}, for clarity, only the upper portion is shown) and fuel mass fraction field (Red: unburnt reactant with Φ=0.65 - Blue: Y_{CH_4}= 0). Case 3.

7.2 Temporally Non-Uniform Equivalence Ratio

7.2.1 Flame Structure

In this case, Φ varies in time with a frequency of 333 Hz. The equivalence ratio at the dump plane is plotted in Figure 7.7. Five cycles are simulated (i.e. 15 ms). The temperature field and the fuel mass fraction field during such a cycle are shown in Figure 7.8 and Figure 7.9, respectively. The points S1 to S8 correspond to the points in Figure 7.7 and are given as reference. Note that the time span between two snapshots on Figures 7.8 and 7.9 (0.45 ms) corresponds to a mean fuel downstream displacement of 2.5 cm. According to the results of sec. 5.2.2, the flame should oscillate between two positions: a tulip-like shape for large value of Φ and a jet like flame for low value of Φ. This is not the case in this simulation. The frequency of the change in inflow equivalence ratio is too large for the flame to transition to the jet-like shape. At the instants denoted S2 and S3, fuel is present in the vortex breakdown bubble but the increases of Φ in the incoming reactant prevents the transition to a stable jet-like flame. The cycle repeat itself, point S8 is identical to the point S2 (see Figure 7.8 and 7.9).

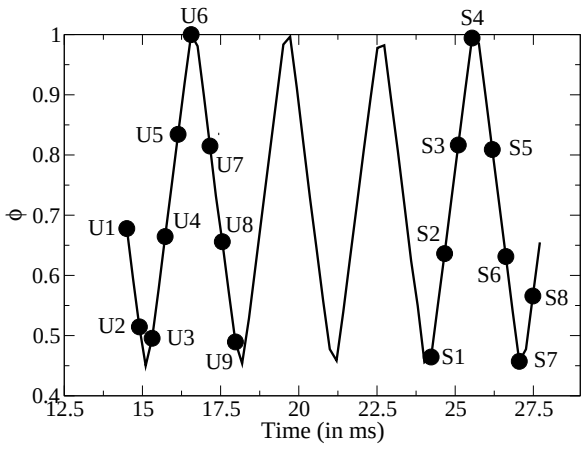

Figure 7.7: Inflow equivalence ratio at the location of the dump plane as a function of time.

During the first cycle of the simulation, a stable jet-like flame is observed (see Figure 7.10 and Figure 7.11 which show the temperature field and the fuel mass fraction field, respectively). Initially, the simulation is carried out using the $GLES$ model with a uniform equivalence ratio of Φ=0.65. When the flow is developed, the $GLES$ model is turned off while the $LEMLES$ model is turned on. Then, the equivalence ratio is first decreased to Φ=0.45 and a jet-like flame structure is observed (Points U3 to U7 in Figures 7.10 and Figure 7.11). In the first cycle (starting at Φ=0.65), the initial post-flame temperature is 1950 K. As Φ decreases, the newly formed products mix with the previously formed products, which have a higher temperature. As a result the temperature of the products located in the flame vicinity is always higher than the theoretical flame temperature and the flame propagation speed is higher than the local theoretical flame speed. However, the propagation speed is not high enough to avoid the transition from a tulip-like flame to a jet-like flame. In the next cycles, the post-flame temperature reaches a value as high as 2450 K (theoretical adiabatic product temperature for Φ=1.0). As the equivalence ratio is decreased, the flame propagation speed decreases less than for the first cycle (the initial post-flame temperature is 2450 K instead of 1950 K). In this cycle, the flame propagation speed is kept large enough such that only a limited jet-like flame is observed (points S2 and S3 in Figures 7.8 and Figure 7.9).

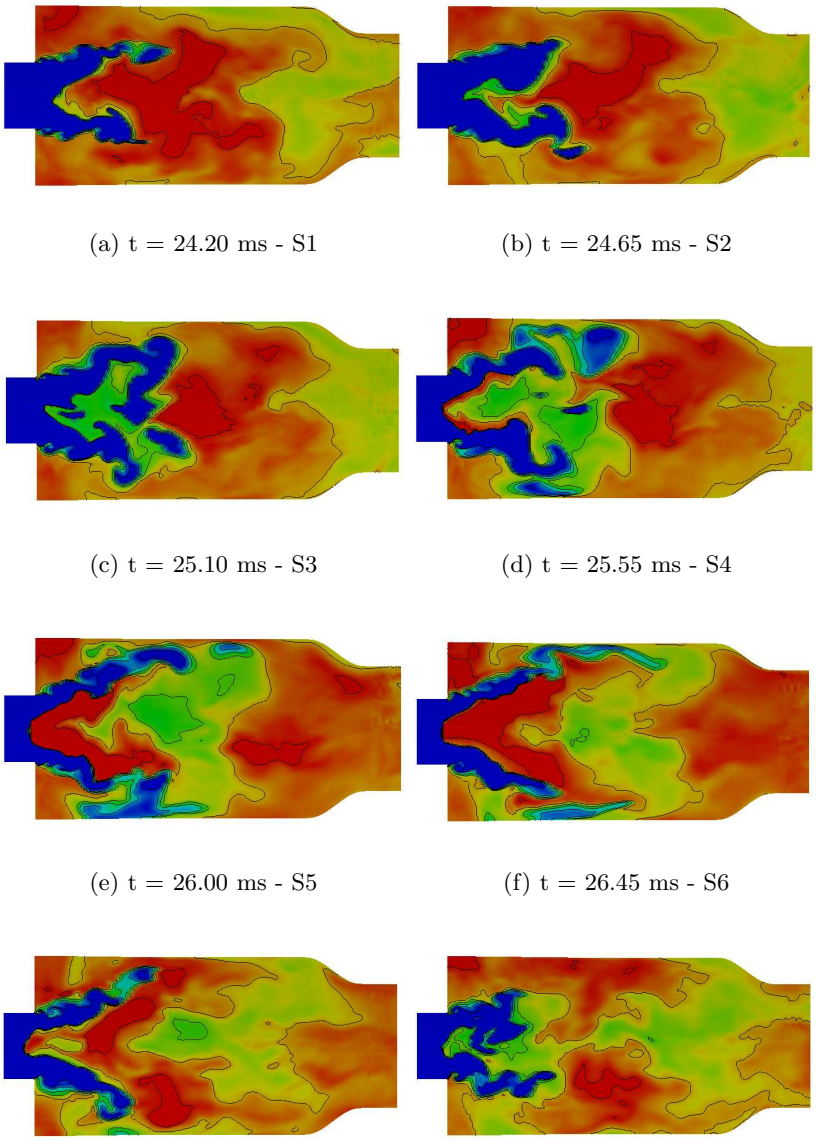

(a) t = 24.20 ms - S1

(b) t = 24.65 ms - S2

(c) t = 25.10 ms - S3

(d) t = 25.55 ms - S4

(e) t = 26.00 ms - S5

(f) t = 26.45 ms - S6

(g) t = 26.90 ms - S7

(h) t = 27.35 ms - S8

Figure 7.8: Instantaneous temperature field - Case 4.

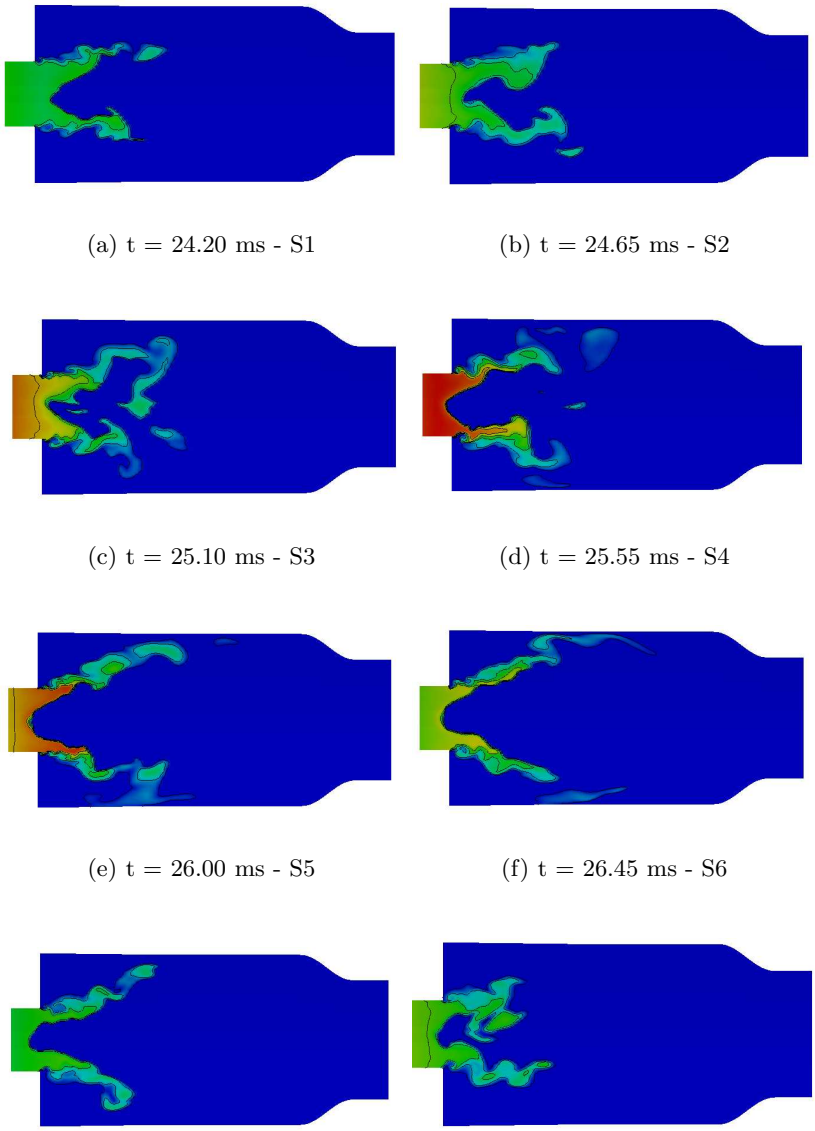

(a) t = 24.20 ms - S1

(b) t = 24.65 ms - S2

(c) t = 25.10 ms - S3

(d) t = 25.55 ms - S4

(e) t = 26.00 ms - S5

(f) t = 26.45 ms - S6

(g) t = 26.90 ms - S7

(h) t = 27.35 ms - S8

Figure 7.9: Instantaneous fuel mass fraction field - Case 4.

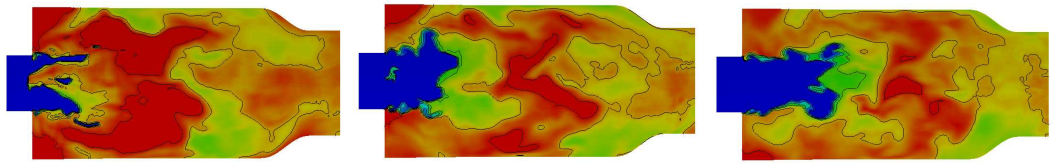

(a) t = 14.50 ms - U1 (b) t = 14.95 ms - U2 (c) t = 15.40 ms - U3

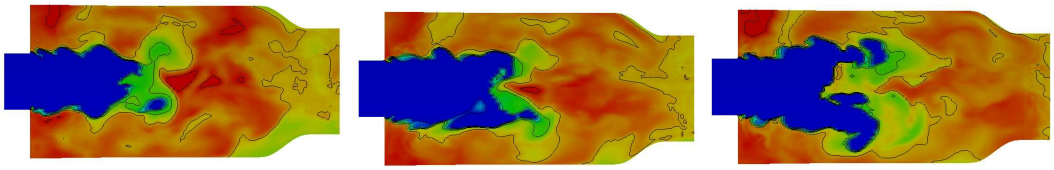

(d) t = 15.85 ms - U4 (e) t = 16.30 ms - U5 (f) t = 16.75 ms - U6

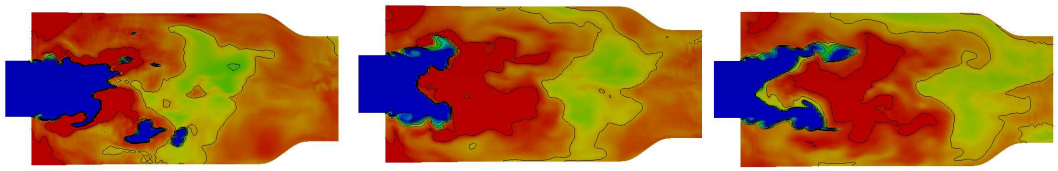

(g) t = 17.20 ms - U7 (h) t = 17.65 ms - U8 (i) t = 18.10 ms - U9

Figure 7.10: Instantaneous temperature field - Case 4.

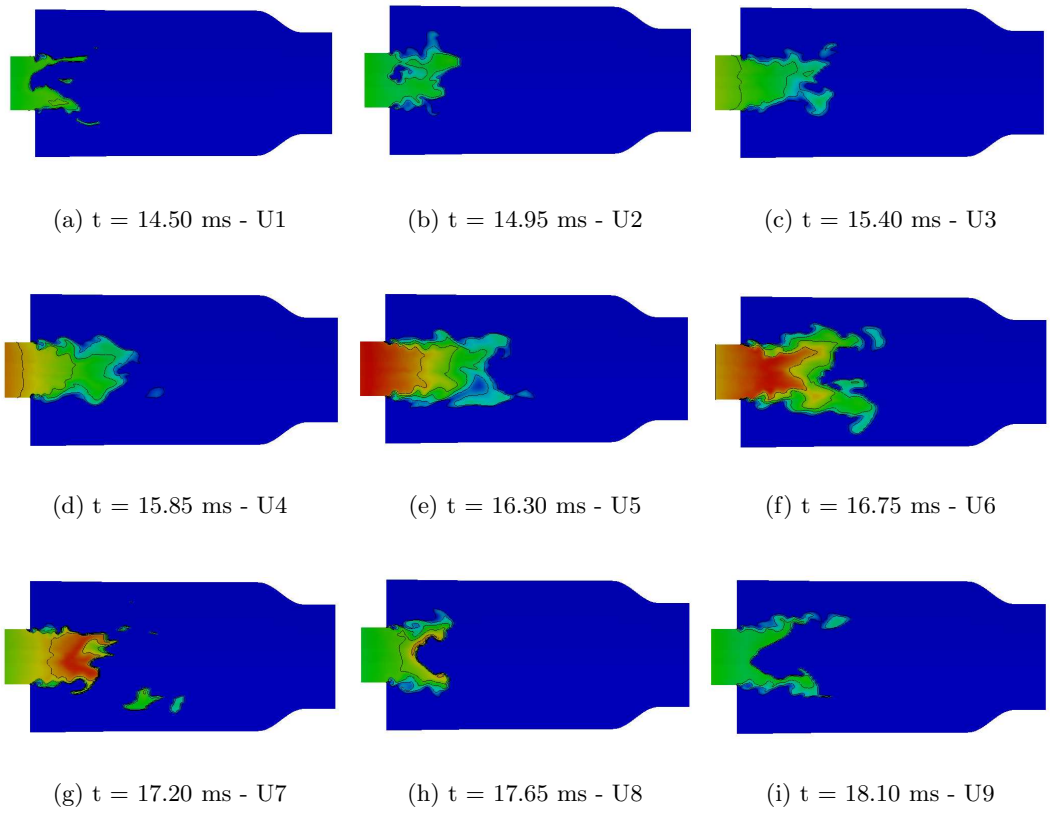

(a) t = 14.50 ms - U1 (b) t = 14.95 ms - U2 (c) t = 15.40 ms - U3

(d) t = 15.85 ms - U4 (e) t = 16.30 ms - U5 (f) t = 16.75 ms - U6

(g) t = 17.20 ms - U7 (h) t = 17.65 ms - U8 (i) t = 18.10 ms - U9

Figure 7.11: Instantaneous fuel mass fraction field - Case 4.

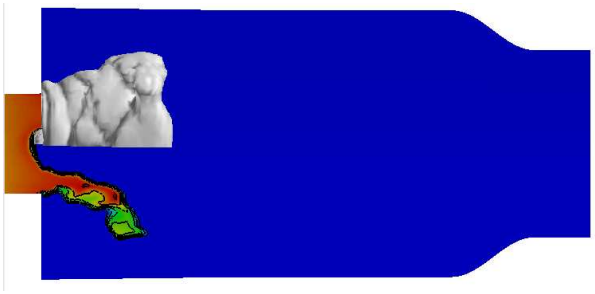

Figure 7.12: Fuel reaction rate iso-surface (for clarity, only the upper portion is shown) and fuel mass fraction field for Φ=1. The incoming equivalence ratio is 1.0. Gray: $\dot{w}_{CH_4}$=-5 s^{-1}, Red: Y_{CH_4}=0.045 ($\Phi \approx 1.0$), Blue: Y_{CH_4}=0.0.

7.2.2 Flame Extinction

It is expected that the behavior of the flame would be similar to case 1 and 2. For low equivalence ratio, flame extinction is observed in the region downstream of the dump plane (i.e. the flame lifts-off) and, for larger equivalence ratio, the heat release counteracts the heat losses and the flame does not quench.

Flame quenching is not observed for all values of the equivalence ratio. In this case, the post-flame temperature does not reach the theoretical adiabatic product temperature (as for case 1) but the post-flame temperature is large enough to prevent flame extinction (see Figure 7.12). The flame quenches and lift-off when the equivalence ratio of the reactant is low (i.e. lower than $\Phi = 0.6$). This is shown in Figure 7.13.

In another simulation, the minimum equivalence ratio was set to 0.42 and flame extinction was observed. The flame lift-off distance was larger than 2 cm and the flame blows-off even when Φ increased again above 0.45. As a result, the minimum value of Φ was chosen to be 0.45.

7.2.3 Dynamics of Case 4

In this section, we focus on the dynamics induced by the variation of the equivalence ratio. The pressure ($\overline{P}$) and the normalized RMS of the pressure ($P_{RMS}/\overline{P}$) are plotted in Figure 7.14. The pressure data was smoothed in order to extract the first mode. For reference, the value of Φ at the dump plane is plotted on the same figure. The first two cycles (t<19 ms)

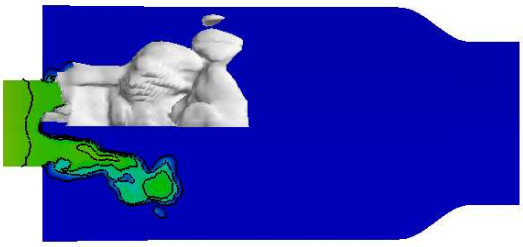

Figure 7.13: Fuel reaction rate iso-surface (for clarity, only the upper portion is shown) and fuel mass fraction field for Φ=1. The incoming equivalence ratio is 0.45. Gray: $\dot{w}_{CH_4}$=-5 s^{-1}, Red: Y_{CH_4}=0.045 ($\Phi \approx 1.0$), Blue: Y_{CH_4}=0.0.

are different from the two last cycles and correspond to the transient phase between the start with the $GLES$ solution and the fully developed $LEMLES$ simulation. The pressure oscillates between 5.8 and 6.2 bars and its frequency is equal to the frequency of change of Φ. The pressure is maximum when Φ is maximum with a time lag of 0.5 ms. The main pressure oscillations are due to oscillations in the product velocity. When Φ increases, the post-flame temperature, hence the post-flame axial velocity, increase. The high temperature fluid elements 'push' the lower speed, lower temperature fluid elements downstream and the pressure builds up. The reverse occurs when Φ decreases. Because the change in Φ controls the variation of $\overline{P}$, the $\overline{P}$ signal is late with regard to the equivalence ratio signal.

The fluctuations of P_{RMS} are low when Φ is high and vice-versa. This is in agreement with the theory that, the lower the equivalence ratio, the larger the pressure fluctuations. Note that P_{RMS} is high (in average, 5.5% of $\overline{P}$). This could be linked to the fact that the post-flame temperature is never equal to the theoretical adiabatic product temperature of the burning fuel (i.e. the flame is always out of equilibrium).

7.3 Combustion Dynamics

The dynamics of the four cases considered in this work is studied. Pressure data are taken in the plane 1 cm downstream of the dump plane. Figure 7.15 shows $P_{RMS}/\overline{P}$ for all four dump combustor cases. As expected, pressure fluctuations are larger in a lean system than in a system operating at stoichiometric conditions (comparison between case 2 and case

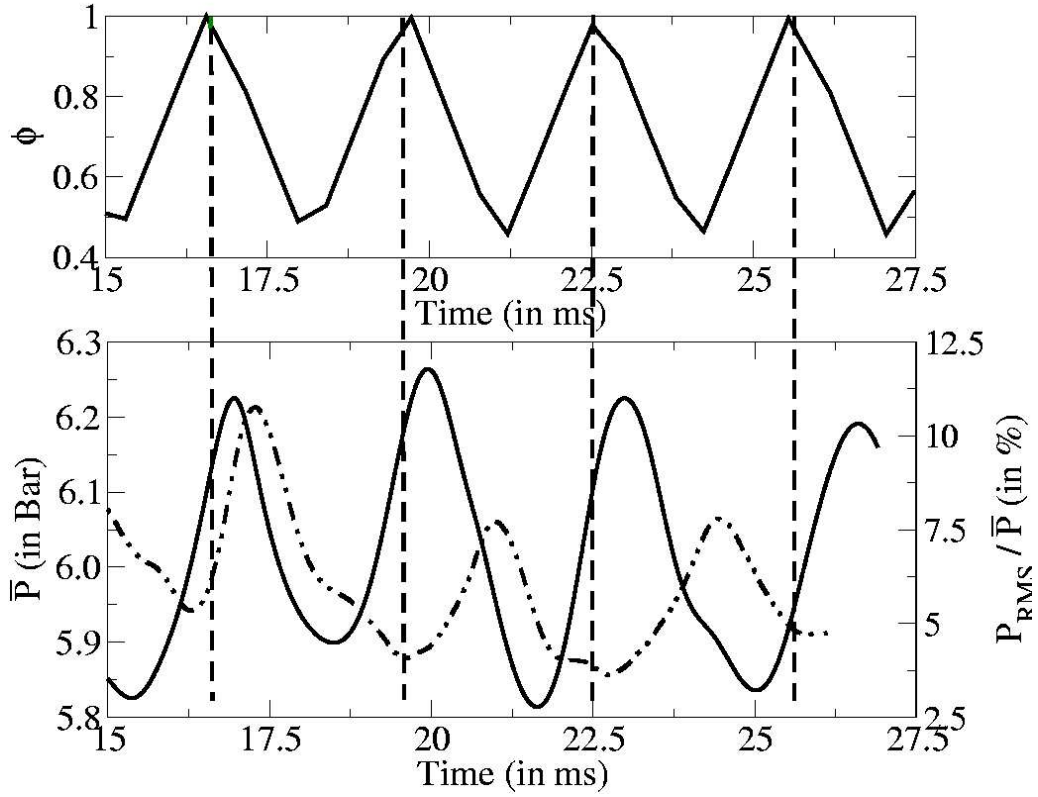

Figure 7.14: $\overline{P}$ and $P_{RMS}/\overline{P}$ as a function of time. For reference, Φ is also plotted as a function of time. Data are smoothed to extract the first mode.

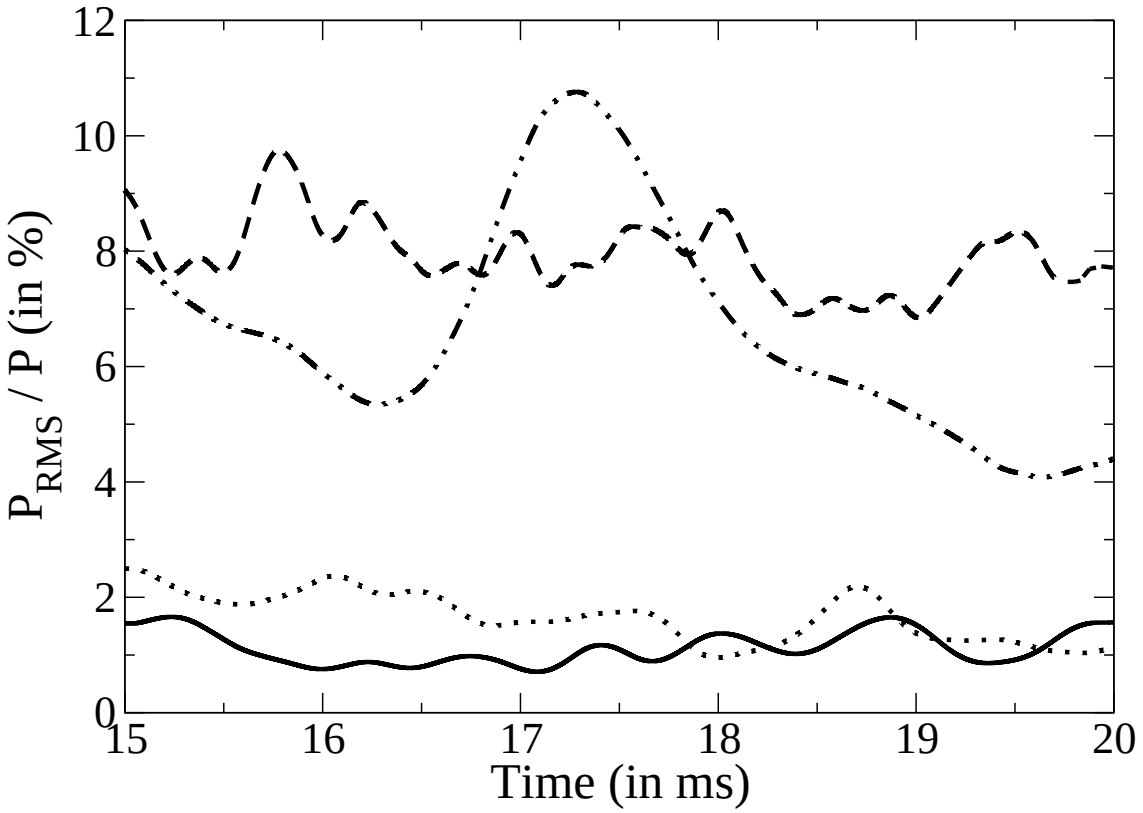

Figure 7.15: $P_{RMS}/\overline{P}$ as a function of time. Solid Line: case 1 dashed line: case 2, dotted line: case 3, dotted-dashed line: case 4.

1). For case 3, pressure oscillations are, in comparison to the other cases, relatively low. The global equivalence ratio for this case is 0.6 and only a limited portion of the flame propagates in the very lean mode. Therefore, pressure oscillations are only slightly larger than in case 1. The situation is different for case 4, where the post-flame temperature is never equal to the theoretical adiabatic post-flame temperature of the inflow reactant mixture (a time lag exists between the change of inflow equivalence ratio and the change of post-flame temperature). As a result, pressure fluctuations are large and vary in time.

7.4 Finite Rates Approach vs. Flamelet Library Approach

The simulations reported in this chapter can also be performed using the *GLES* model. For example, Stone [2002] performed a simulation similar to Case 4. However, the *GLES* model is limited for these kind of simulations because it does not consider the transient

behavior of the flame propagation speed. In the $GLES$ model, S_L is a function of the fuel mixture fraction. This is accurate when the mixture fraction is uniform. In reality, the flame propagation speed is a function of the post-flame temperature and, therefore, the $GLES$ model is not accurate when the reactant equivalence ratio changes in time or space. In the $LEMLES$ model, the flame propagation speed is a function of the post-flame temperature, hence, this model is accurate for simulations where the inflow reactant Φ is non-uniform in space and/or time.

CHAPTER VIII

CONCLUSION

The general goals of this study were to study emission predictions from an experimental combustion chamber, to improve the Linear-Eddy Mixing (LEM) model that is embedded in the Large-Eddy Simulation (LES) solver as well as to study parameters that can lead to the lift-off of a lean premixed flame.

Experimental level of emissions were available for a well documented Department of Energy Humid Air Turbine combustor ($DOEHAT$). Thus this combustion chamber was chosen as a framework for the study of prediction of pollutant emissions using numerical tools. Experimental results show that for Φ>0.44, CO level at the exit of the combustion chamber corresponds to the amount of CO at equilibrium. Thus experimental emission predictions for Φ>0.44 were easily reproduced using LES. However, for Φ<0.44, the amount of CO at the exit of the combustion chamber exponentially increases and the prediction of this trend was the challenge of this study. Initially, we checked to see if the amount of CO formed at the flame front was not fully oxidized before reaching the emission probe. However, the results showed that the CO produced at the primary flame front reduces to its equilibrium for Φ<0.44. As a result, we implemented a simple wall heat loss model to study the effect of product cooling on the level of CO emission. While colder post-flame temperatures lead to a lower rate of oxidation of CO in the post-flame region, the numerical emission levels still reaches equilibrium at the probe location. This discrepancy with the experimental results may be due to the lack of data concerning heat losses in the $DOEHAT$ combustion chamber as well as the simplicity of the wall heat loss model used here. Previous numerical studies have suggested that the release of unburnt fuel in the post-flame region can be an additional source of CO in the post-flame region. Thus, we included the release of unburnt fuel via local flame extinction in our simulation and observed that this additional source of CO, formed later in the combustion process did produce a dramatic increase in CO

emission for $\Phi<0.44$. Thus, reasonable agreement with experimental results was obtained only when the release of unburnt fuel at the flame front was included. NO emissions were also compared. We modeled NO formation via two sources: prompt and thermal NO. NO production was computed by post-processing output data from 1-D flame calculations (CHEMKIN-PREMIXED and GRI-MECH 2.11) Note that this technique (also known as a flamelet library approach) drastically simplifies the chemical processes and may lead to some errors. Still, numerical results are in reasonable agreement with the experimental results. The trend of NO emission was reproduced and it was fond that the formation of NO in the post-flame region is negligible for $\Phi<0.5$ and only a small amount of NO is formed in the post-flame region for $\Phi=0.53$. Thus prompt NO is the primary source of NO for those lean conditions. The differences between the numerical and experimental results were less than 5 ppm and may be due to the simplicity of the numerical NO formation model as well as possible inaccuracies in both GRI-MECH 2.11 prompt NO rates and the experimental measurements.

The second part of this work focused on the use of the LEM model. Efforts were focused on decreasing the cost of the computation of the reaction rates. Compared to previous versions of the LEM implementation, the new approach is four times less computationally expensive. It was shown that classical flamelet modeling approaches (denoted $GLES$ in this work) fail in the Broken Reaction-Zone (BRZ) regime, whereas the LEM model does not have such a limitation and is valid for all turbulent combustion regimes. The limitation of the flamelet models was observed by comparing flame lengths and shapes obtained in a dump combustor for $\Phi=1.0$ (where the combustion process occurs in the flamelet regime) and $\Phi=0.45$ (BRZ regime). Results for $GLES$ and $LEMLES$ are similar for $\Phi=1.0$, but $GLES$ over-predicts the flame propagation speed for $\Phi=0.45$. It should be noted that the absence of inter-LES cell molecular diffusion in the $LEMLES$ model leads to its inability to simulate the propagation of fully laminar flames. This is not a significant, as the $LEMLES$ model was developed for highly turbulent reacting flows. In this later case, the influence of inter-LES cells molecular diffusion on the combustion process should be negligible.

In simulations with adiabatic wall conditions, the flame is anchored to the corner formed

by the sudden expansion of the inflow pipe. In order to simulate flame lift-off, limited heat losses were introduced at the tip of the inflow pipe, and it was observed that the flame no longer anchors at this corner. The flame lift-off phenomena is unsteady, and its dynamics were shown to be related to natural acoustic modes of the combustor. Pure flame extinction via high levels of turbulence as well as the presence of unburnt fuel in the post-flame region were not observed. If such phenomena are to be modeled, a realistic numerical simulation must include a more detailed chemical mechanism (only 1-step and 4-step mechanisms were used in this study) and product cooling (either vie heat losses at the wall or via injection of cooling air in the post-flame region) has to be accurately simulated.

Because real combustion systems do not operate at fixed inflow conditions (temperature, pressure, equivalence ratio, etc.), combustion processes in the dump combustion chamber were studied under transient operating conditions, Specifically, the inflow equivalence ratio was non-uniform in either space or time. The main goal of this part of the study should be considered as a first step toward numerical simulation of transient combustion systems. In the case where the inflow equivalence ratio varies in space, the high temperature recirculating gases stabilizes the flame in region of very low equivalence ratio ($LEMLES$ approach). If a flamelet approach was to be used, the flame would not propagate in region of very low equivalence ratio and would blow-off. In the case where the inflow equivalence ratio varies in time, the flame propagation speed strongly varies as a function of the product temperature and the equivalence ratio ($LEMLES$ approach). If a flamelet ($GLES$) approach was to be used, the flame propagation speed would only be a function of the equivalence ratio. Thus a simulation using the $GLES$ approach would not be accurate. To summarize, classical flamelet models use equilibrium data to compute information like flame propagation speed, product temperature, etc. In the $LEMLES$ model, the combustion processes entirely depends upon the state of the gas mixture, thus transient systems can be more accurately simulated by the $LEMLES$ model.

The only major drawbacks of the $LEMLES$ method are its computational cost and its large memory requirements. However, because the unequaled advantages of the $LEMLES$ model, this should only be considered as a minor burden and future improvements of the

LEM implementation should decrease further the computational cost of this method.

In conclusion, a model was developed and tested and is adequate for the simulation of combustion process in full scale combustion chambers, where the combustion processes occur in various turbulent premixed combustion regimes. It was shown that this model can be used for the simulation of more realistic systems, where operating conditions are not constant.

CHAPTER IX

RECOMMENDATIONS FOR FUTURE WORK

Pollutant Emission Prediction. In the flamelet approach, the NO model has to be improved to accurately predict the level of NO emission. Also, in order to accurately predicts the emission of CO, the production of UHC via flame extinction has to be simulated. The $INFTS$ model used in this study is accurate but is only a model developed for $RANS$ (steady) simulation. Either a model predicting flame quenching in unsteady simulation has to be developed, or the production of UHC via flame extinction has to be simulated via the use of the $LEMLES$ approach, the latter being more computationally expensive.

LEMLES Model. The major flaws of this model are the lack of molecular diffusion between LEM domains as well as the lack of stirring between LEM domains. Thus, neither laminar flame propagation nor accurate flame structure resolution can be simulated. Resolving these two issues is challenging but should be considered as a first priority.

Computation of the chemical reaction rates in the $LEMLES$ Model. More than half of the computational cost of the $LEMLES$ Model approach is related to the computation of the reaction rates. Methods like Artificial Neural Networks must be considered in order to speed-up the computation of the chemical reaction rates.

Flame extinction and heat losses. The heat loss model used in this study is rather simple and uses ad-hoc constant. Experimental data, for example, should be used to ensure a more realistic modeling of the heat losses.

Flame extinction and flame lift-off. More experimental data are needed. Flame extinction and UHC production are very sensitive processes and one can not "guess" the proper conditions leading to a stable, lifted-off flame releasing UHC in the post-flame region. More experimental information than only the average nominal operating conditions should be provided. Inflow conditions data should be provided as a function of time and space. Only such information can lead to an accurate prediction of the systems dynamics. Also, in

study of flame extinction and flame lift-off, the pressures waves present in the inflow pipe play an important role Sommerer et al. [2004]. The computational domain must include the entire inflow geometry and not only an ad-hoc designed inflow pipe as used in this study. This should lead to a better prediction of the acoustics boundary conditions and should provide a better understanding of the dynamics of the system studied.

Bibliography

B. Bédat and R. K. Cheng. Experimental study of premixed flames in intense isotropic turbulence. *Combustion and Flame*, 100:486–494, 1995.

A. Bhargava, D. W. Kendrick, M. B. Colket, W. A. Sowa, K. H. Casleton, and D. J. Maloney. Pressure effects on no_x and co emission in industrial gas turbines. *Trans. of the ASME*, 2000-GT-8, 2000.

P. Bradshaw. Effects of streamline curvature on turbulent flow. Technical Report AGARD-AG-169, AGARD-AG, 1973.

A. Buschmann, F. Dinkelacker, T. Schaefer, M. Schaefer, and J. Wolfrum. Measurement of the instantaneous detailed flame structure in turbulent premixed combustion. *Twenty-Sixth Symposium (International) on Combustion*, pages 437–445, 1996.

W. Bush and F. Fendell. Asymptotic analysis of laminar flame propagation for general lewis numbers. *Combustion Science and Technology*, 421:1, 1970.

S. Byggstoyl and B. F. Magnussen. Model for flame extinction in turbulent flow. In *Turbulent Shear Flows 4*, pages 381–395. Springer-Verlag, 1988.

W. H. Calhoon. *On Subgrid Combustion Modeling for Large-Eddy Simulations*. PhD thesis, Georgia Institute of Technology, Atlanta, GA, August 1996.

W. H. Calhoon and S. Menon. Subgrid modeling for reacting large eddy simulations. *AIAA-96-0516*, 1996.

S. M. Cannon, B. Zuo, and C. E. Smith. Les predictions of combustor emissions from a practical industrial fuel injector. *ASME-2003-GT-38200*, 2003.

J. M. Card, J. H. Chen, M. Day, and S. Mahalingam. Direct numerical simulation of turbulent non-premixed methane-air flames modeled with reduced kinetics. *Studying turbulence using Numerical Simulation Databases - V*, pages 41–54, 1994.

V. Chakravarthy and S. Menon. Large-eddy simulations of turbulent premixed flames in the flamelet regime. *Combustion Science and Technology*, 162:1–48, 2000.

V. Chakravarthy and S. Menon. Linear-eddy simulations of reynolds and schmidt number dependencies in turbulent scalar mixing. *Physics of Fluids*, 13:488–499, 2001a.

V. Chakravarthy and S. Menon. Subgrid modeling of premixed flames in the flamelet regime. *Flow, Turbulance and Combustion*, 2001b.

Chen.Y.C., N. Peters, Schneemann.G.A.i, Wruck.N.i, Renz.U., and ansour.M.S. The detailed structure of highly stretched turbulent premixed methane-air flames. *Combustion and Flame*, 107:223–244, 1996.

P. Clavin. Dynamic behavior of premixed flame fronts in laminar and turbulent flows. *Progress in Energy and Combustion Science*, 11:1–59, 1985.

F. Dinkelacker, A. Soika, D. Most, D. Hofmann, A. Leipertz, W. Polifke, and K. Doebbeling. Structure of locally quenched higly turbulent lean premixed flames. *Twenty-Seventh Symposium (International) on Combustion*, pages 857–865, 1998.

G. Eggenspieler and S. Menon. Finite rate chemistry modeling for pollutant emission prediction near lean blow out. *AIAA-2003-4941*, 2003a.

G. Eggenspieler and S. Menon. Modeling of pollutant formation near lean blow out in gas turbine engines. *Direct and Large Eddy Simulation V*, 2003b.

G. Erlebacher, M. Y. Hussaini, C. G. Speziale, and T. A. Zang. Toward the large-eddy simulation of compressible turbulent flows. *Journal of Fluid Mechanics*, 238:155–185, 1992.

T. F. Fric. Effects of fuel-air unmixedness on nox emissions. *Journal of Propulsion and Power*, 9(5):708–713, 1993.

C. Fureby. Large-eddy simulation of turbulent anisochoric flows. *AIAA Journal*, 33(7): 1263–1272, 1995.

C. Fureby and C. Löfström. Large-eddy simulations of bluff body stabilized flames. *Proceedings of the Combustion Institute*, 27:1257–1264, 1994.

M. Germano, U. Piomelli, P. Moin, and W. H. Cabot. A dynamic subgrid-scale eddy viscosity model. *Physics of Fluids A*, 3(11):1760–1765, 1991.

S. Ghosal. On the large-eddy simulation of turbulent flows in complex geometries. Technical report, Center for Turbulence Research, 1993.

T. J. Held and H. C. Mongia. Emissions modeling of gas turbine combustors using a partially-premixed laminar flamelet model. *AIAA-98-3950*, 1998.

T. J. Held, M. A. Mueller, and H. C. Mongia. A data-driven model for no_x, co and uhc emissions for a dry low emissions gas turbine combustor. *AIAA-2001-3425*, 2001.

S. Hill and L. Douglas Smoot. Modeling of nitrogen oxides formation and destruction in combustion systems. *Progress in Energy and Combustion Science*, 26:417–458, 2000.

Y. Huan, S. Y. Hsieh, and V. Yang. Numerical modeling of combustion dynamics of a lean-premixed swirl-stabilized injector. *AIAA-02-1009*, 2002.

J. Jarosinski, J. Lee, and R. Knystautas. Interaction of a vortex ring and a laminar flame. *Twenty-Second Symposium (International) on Combustion*, 22:505–514, 1988.

L. Kagan and G. Sivashinsky. Flame propagation and extinction in large scale vortical flows. *Combustion and Flame*, 120:222–232, 2000.

J. R. Kee, F. M. Rupley, and J. A. Miller. Chemkin-ii a fortran chemical kinetics package for the analysis of gas phase chemical kinetics. Technical Report SAND89-8009B, Sandia National Laboratories, 1992.

D. W. Kendrick, A. Bahrgave, M. B. Colket, A. W. Sowa, D. J. Maloney, and K. H. Casleton. Nox scaling characteristics for industrial gas turbine fuel injectors. *ASME-2000-GT-98*, 2000.

A. R. Kerstein. Linear-eddy model of turbulent scalar transport and mixing. *Combustion Science and Technology*, 60:391–421, 1988.

A. R. Kerstein. Linear-eddy model of turbulent transport ii. *Combustion and Flame*, 75: 397–413, 1989.

A. R. Kerstein. Linear-eddy model of turbulent transport iii. *Journal of Fluid Mechanics*, 216:411–435, 1990.

A. R. Kerstein. Linear-eddy modeling of turbulent transport. part 6. microstructure of diffusive scalar mixing fields. *Journal of Fluid Mechanics*, 231:361–394, 1991a.

A. R. Kerstein. Linear-eddy modeling of turbulent transport. part v: Geometry of scalar interfaces. *Physics of Fluids A*, 3(5):1110–1114, 1991b.

A. R. Kerstein. Linear-eddy modeling of turbulent transport. part 4. structure of diffusion-flames. *Combustion Science and Technology*, 81:75–86, 1992.

A. R. Kerstein and W. T. Ashurst. Propagation rate of growing interfaces in stirred fluids. *Physical Review*, 68(7):934–937, 1992.

W.-W. Kim and S. Menon. A new dynamic one-equation subgrid-scale model for large-eddy simulations. *AIAA-95-0356*, 1995.

W.-W. Kim and S. Menon. A new incompressible solver for large-eddy simulations. *International Journal of Numerical Fluid Mechanics*, 31:983–1017, 1999.

W.-W. Kim and S. Menon. Numerical simulations of turbulent premixed flames in the thin-reaction-zones regime. *Combustion Science and Technology*, 160:119–150, 2000.

W.-W. Kim, S. Menon, and H. C. Mongia. Large eddy simulations of reacting flow in a dump combustor. *AIAA-98-2432*, 1998.

W.-W. Kim, S. Menon, and H. C. Mongia. Large-eddy simulation of a gas turbine combustor flow. *Combustion Science and Technology*, 143:25–62, 1999.

C. Law and C. J. Sung. Structure, aerodynamics, and geometry of premixed flames. *Progress in Energy and Combustion Science*, 26:459–505, 2000.

P. A. Libby, A. Linan, and F. Williams. Structure of laminar flamelets in premixed turbulent flames. *Combustion and Flame*, 44:287, 1982.

P. A. Libby and F. Williams. Strained premixed laminar flames with no-unity lewis number. *Combustion Science and Technology*, 34:257, 1983.

T. Lieuwen and B. Zinn. The role of equivalence ration oscillations in driving combustion instabilities in low no_x gas turbines combustors. *Twenty-seventh Symposium (International) on Combustion*, pages 1809–1816, 1998.

G. Lilley. Swirl flows in combustion: A review. *AIAA Journal*, 15(8):1063–1078, 1977.

D. K. Lilly. A proposed modification of the germano subgrid-scale closure method. *Physics of Fluids A*, 4(3):633–635, 1992.

R. W. MacCormack. The effect of viscosity in hypervelocity impact cratering. *AIAA-69-0354*, 1969.

R. W. MacCormack. An efficient numerical method for solving the time-dependent compressible navier-stokes equations at high reynolds number. Technical Report NASA Technical Memorandum x-73, National Aeronautics and Space Administration, 1976.

M. Mansour, N. Peters, and Y. Chen. Investigation of scalar mixing in the thin reaction zones regime using a simultaneous ch-lif/rayleigh laser technique. *Proceedings of the Combustion Instutute*, 27:767–773, 1998.

P. McMurtry, C. Todd, A. Kerstein, and S. Krueger. Linear eddy simulations of mixing in a homogeneous turbulent flow. *The Physics of Fluids*, 5(4):1023–1034, 1993a.

P. A. McMurtry, T. C. Gansauge, A. R. Kerstein, and S. K. Krueger. Linear-eddy simulations of mixing in a homogeneous turbulent flow. *Physics of Fluids A*, 5:1023–1034, 1993b.

P. A. McMurtry, S. Menon, and A. R. Kerstein. A subgrid mixing model for les on nonpremixed turbulent combustion. *AIAA-92-0234*, 1992.

C. Meneveau and T. Poinsot. Stretching and quenching of flamelets in premixed turbulent combustion. *Combustion and Flame*, 86:311–332, 1991.

S. Menon and A. R. Kerstein. Stochastic simulation of the structure and propagation rate of turbulent premixed flames. *Proceedings of the Combustion Institute*, 24:443–450, 1992.

S. Menon and W.-W. Kim. High reynolds number flow simulations using the localized dynamic subgrid-scale model. *AIAA-96-0425*, 1996.

S. Menon, P. McMurtry, and A. R. Kerstein. A linear eddy mixing model for large eddy simulation of turbulent combustion. In B. Galperin and S. Orszag, editors, *LES of Complex Engineering and Geophysical Flows*. Cambridge University Press, 1993.

S. Menon, P.-K. Yeung, and W.-W. Kim. Effect of subgrid models on the computed interscale energy transfer in isotropic turbulence. *Computers and Fluids*, 25(2):165–180, 1996.

C. Müller, J. Driscoll, D. Sutkus, W. Roberts, M. Drake, and M. Smooke. Effect of unsteady stretch rate on oh chemistry during a flame-vortx interaction: To asses flamelets models. *Combustion and Flame*, 100:323–331, 1995.

H. N. Najm and P. S. Wyckoff. Premixed flame response to unsteady strain rate and curvature. *Combustion and Flame*, 110:92–112, 1997.

C. C. Nelson. *Simulations of Spatially Evolving Compressible Turbulence Using a Local Dynamic Subgrid Model*. PhD thesis, Georgia Institute of Technology, Atlanta, GA, December 1997.

S. Pannala and S. Menon. Large eddy simulations of two-phase turbulent flows. *AIAA 98-0163, 36th AIAA Aerospace Sciences Meeting*, 1998.

N. Patel, C. Stone, and S. Menon. Large-eddy simulation of turbulent flow over an axisymmetric hill. *AIAA 2003-0967, 41th AIAA Aerospace Sciences Meeting*, 2003.

S. Patel, N. andMenon. Subgrid modeling for les of spray combustion in large-scale combustors. *AIAA Journal*, 2005.

P. Pelce and P. Clavin. Influence of hydrodynamics and diffusion upon the stability limits of laminar premixed flames. *Journal of Fluid Mechanics*, 124:219–237, 1982.

N. Peters. Laminar diffusion flamelet models in non-premixed turnbulent combustion. *Prog. Energy Combust. Sci*, 10:319–339, 1984.

N. Peters. The turbulent burning velocity for large-scale and small scale turbulence. *Journal of Fluid mechanics*, 384:107–132, 1999.

N. Peters. *Turbulent Combustion*. Cambridge Monographs on Mechanics, 2000.

H. Pitsch and L. Duchamp De Lageneste. Large-eddy simulation of premixed turbulent combustion using a level-set approach. *Twenty-Ninth Symposium (International) on Combustion*, 29:2001–2008, 2002.

A. Pocheau. Front propagation in a turbulent medium. *Europhysics Letters*, 20(5):401–406, 1992.

T. Poinsot and S. Lele. Boundary conditions for direct simulations of compressible viscous flow. *Journal of Computational Physics*, 101:104–129, 1992.

T. Poinsot, D. Veynante, and S. Candel. Diagrams of premixed turbulent combustion based on direct simulation. *Twenty-Third Symposium (International) on Combustion*, 23:613–619, 1990.

T. Poinsot, D. Veynante, and S. Candel. Quenching processes and premixed turbulent combustion diagrams. *Journal of Fluid Mechanics*, 228:561–606, 1991.

S. Pope. Computationally efficient implementation of combustion chemistry using in situ adaptive tabulation. *Combustion Theory Modelling*, 1:41–63, 1997.

S. Pope. *Turbulent Flows*. Cambridge University Press, 2000.

J. W. S. Rayleigh. *Theory of Sound*, volume 2. Dover Publications, Inc., 1945.

P. Roberts. *The End of Oil*. Houghton Mifflin, 2004.

W. L. Roberts, J. F. Driscoll, M. C. Drake, and L. P. Goss. Images of the quenching of a flame by a vortex-to quantify regimes of turbulent combustion. *Combustion and Flame*, 94:58–69, 1993.

G. Russo and P. Smereka. A remark on computing distance functions. *Journal of Computational Physics*, 163(1):51–67, 1994.

V. Sankaran. *Sub-grid Combustion Modeling for Compressible Two Phase Reacting Flow*. PhD thesis, Georgia Institute of Technology, Atlanta, GA, July 2003.

V. Sankaran and S. Menon. The structure of premixed flame in the thin-reaction-zones regime. *Proceedings of the Combustion Institute*, 28:203–210, 2000.

V. Sankaran, I. Porumbel, and S. Menon. Large-eddy simulation of a single-cup gas turbine combustor. *AIAA-2003-5083*, 2003.

J. Smagorinsky. General circulation experiments with the primitive equations. *Monthly Weather Review*, 91(3):99–164, 1993.

T. Smith and S. Menon. One-dimensional simulations of freely propagating turbulent premixed flames. *Combustion Science and Technology*, 128:99–130, 1996a.

T. M. Smith. *Unsteady Simulations of Turbulent Premixed Reacting Flows*. PhD thesis, Georgia Institute of Technology, Atlanta, GA, March 1998.

T. M. Smith and S. Menon. The structure of premixed flames in a spatially evolving turbulent flow. *Combustion Science and Technology*, 119(1-6):77–106, 1996b.

T. M. Smith and S. Menon. Subgrid combustion modeling for premixed turbulent reacting flows. *AIAA-98-0242*, 1998.

Y. Sommerer, D. Galley, T. Poinsot, S. Ducruix, F. Lacas, and D. Veynante. Large eddy simulation and experimental study of flashback and blow -off in a lean partially premixed swirler burner. *Journal of Turbulence*, 5, 2004.

C. Stone. *Large-Eddy Simulation of Combustion Dynamics in Swirling Flows*. PhD thesis, Georgia Institute of Technology, Atlanta, GA, August 2004.

C. Stone and S. Menon. Numerical simulation of combustion dynamics in a swirling dump combustor. In *Proceedings of Grand Challenges In Computer Simulations, High Performance Computing 2001*, pages 15–20. SCS Press, 2001.

S. Stone, C. Menon. Adaptive swirl control of combustion instability in gas turbine combustors. *Proceedings of the Combustion Institute*, 29:155–160, 2002.

K. Tajiri and S. Menon. Les of combustion dynamics in a pulse combustor. *AIAA-01-0194*, 2001.

E. Turkel. Preconditioned methods for solving the incompressible and low speed compressible equations. *Journal of Computational Physics*, 72:277–298, 1987.

D. Veynante, J. Piana, J. M. Duclos, and C. Martel. Experimental analysis of flame surface density models for premixed turbulent combustion. In *Twenty-Sixth Symposium (International) on Combustion*, pages 413–420, Pittsburgh, PA, 1996. The Combustion Institute.

B. Vreman, B. Geurts, and H. Kuerten. On the formulation of the dynamic mixed subgrid-scale model. *Physics of Fluids*, 6(12):4057–4059, 1994.

J. Warnatz. Rate coefficients in the c/h/o system. *Combustion Chemistry*, pages 197–360, 1984.

C. K. Westbrook and F. L. Dryer. Simplified reaction mechanisms for the oxidation of hydrocarbon fuels in flames. *Combustion Science and Technology*, 27:31–43, 1981.

F. A. Williams. *Combustion Theory*. The Benjamin/Cummings Publishing Company, Inc., second edition, 1985.

M. H. Zimberg, S. . H. Frankel, J. Gore, and S. Y. R. A study of coupled turbulent mixing, soot chemistry and radiation effects using the linear eddy model. *Combustion and Flame*, 113:454–469, 1998.

VITA

Gilles Eggenspieler was born to Jean-Louis Eggenspieler and Anny Haertel in Mulhouse (Haut-Rhin, France) on the 30th day of September of the year 1977. Upon graduation from high school (1995), he entered the preparatory classes at Lycèe Klèber (Strasbourg, France). Two years later, he entered the Ecole Nationale Supèrieure des Mines de Nancy, (Nancy, France) and graduated with the 'Ingènieur Civil des Mines' diploma in 2000 after spending one year as an exchange student at the Technische Universität München (Munich, Germany). He began graduate studies in the Department of Aerospace Engineering at the Georgia Institute of Technology (Atlanta, USA) in the Fall of the year 2000. From that time, he has been happily working under the advisement of Prof. Suresh Menon. He graduated with the PhD degree in Aerospace Engineering in Summer of 2005 and started his professional career at the same time. His first position was consultant-engineer at Fluent, Inc.